Computational Analysis of Transcript Interactions and Variants in Cancer

A THESIS
SUBMITTED TO THE FACULTY OF THE GRADUATE SCHOOL
OF THE UNIVERSITY OF MINNESOTA
BY

Wei Zhang

IN PARTIAL FULFILLMENT OF THE REQUIREMENTS
FOR THE DEGREE OF
Doctor of Philosophy

Rui Kuang

November, 2015

Acknowledgements

There are many people that have earned my gratitude for their contribution to my time in graduate school.

First and foremost, I would like to express my sincerest gratitude and appreciation to my advisor Dr. Rui Kuang for his invaluable support and guidance throughout my graduate study. His motivation, enthusiasm, immense knowledge and dedication to research trigger my interests on research. This thesis would not have been possible without his support and encouragement.

Second, I would like to extend my appreciation to my co-advisor Dr. Baolin Wu and my collaborator Dr. Jeongsik Yong. I appreciate all their contributions of time, ideas to make my Ph.D. experience productive.

Third, I am grateful to our computational biology group formal and current members, Dr. Taehyun Hwang, Dr. Ze Tian, Huanan Zhang, Dr. Maoqiang Xie, Raphael Petegrosso, David Roe, Zhuliu Li, Catherine Lee, and Nishitha Paidimukkala, and collaborator from University of Kansas Cancer Center, Dr. Jeremy Chien.

My sincere thanks also go to Dr. Bin Li, who I have worked with during my summer internship. His supervision and support truly helped the progress and smoothness of my internship program.

For this thesis I would like to thank my committee members Dr. Vipin Kumar and Dr. Chad Myers for their time, interest, insightful questions and helpful comments.

Finally, I would like to thank all my friends, family and professors who have helped me grow and become the person I am today. Especially my wife, Shiyang Su and my parents, I would not be here without all of their love, support, and encouragement.

Dedication

To my parents.

Abstract

New sequencing and array technologies for transcriptome-wide profiling of RNAs have greatly promoted the interest in gene and isoform-based functional characterizations of a cellular system. Many statistical and machine learning methods have been developed to quantify the isoform/gene expression and identify the transcript variants for cancer outcome prediction. Since building reliable learning models for cancer transcriptome analysis relies on accurate modeling of prior knowledge and interactions between the cellular components, it is still a computational challenge.

This thesis proposes several robust and reliable learning models to integrate both large-scale array and sequencing data with biological prior knowledge for cancer transcriptome analysis. First, we explore two signed network propagation algorithms and general optimization frameworks for detecting differential gene expressions and DNA copy number variations (CNV). Second, we present a network-based Cox regression model called *Net-Cox* and applied *Net-Cox* for a large-scale survival analysis across multiple ovarian cancer datasets to identify highly consistent signature genes and improve the accuracy of survival prediction. Third, we introduce a Network-based method for RNA-Seq-based Transcript Quantification (*Net-RSTQ*) to integrate protein domain-domain interaction network with short read alignments for transcript abundance estimation. Finally, we perform computational analysis of mRNA 3'-UTR shortening on mouse embryonic fibroblast (MEF) cell lines to understand changes of molecular features on dysregulated activation of mammalian target of rapamycin (mTOR).

We evaluate our models and findings with simulations and real genomic datasets. The results suggest that our models explore the global topological information in the networks, improve the transcript quantification for better sample classification, identified consistent biomarkers to improve cancer prognosis and survival prediction. The analysis of 3'-UTR with RNA-Seq data find an unexpected link between mTOR and ubiquitin-mediated proteolysis pathway through 3'-UTR shortening.

Contents

List of Tables

List of Figures

Chapter 1

Introduction

1.1 Background

Messenger RNA (mRNA) is a large family of RNA molecules. It carries codes from the DNA and translated into proteins. Since mRNA expression is strongly correlated with protein activities, it is often used as a signature in cancer analysis. Transcriptomic technologies such as mRNA-Sequencing (RNA-Seq) and Microarrays have given us the ability to analyze cellular mRNA levels globally, which enable effective molecular phenotyping of cancers, providing novel insights into the disease. Some pioneer works have shown that the mRNA expression patterns caused by BRCA1 or BRCA2 mutation are associated with either a poor prognosis or a good prognosis of breast cancer and ovarian cancer [1–3] by analysing microarray gene expression data.

In the human transcriptome, there are ∼21,000 protein coding genes and many of these genes can encode multiple protein isoforms. Besides transcript isoforms, there are other transcript variants such as gene fusion and alterative polyadenylation can still be introduced into mRNA and affect the expression of gene and isoforms. Moreover, as a complex disease, cancer is believed to be caused by a combination of the effects of multiple transcript variants. Therefore, analyzing cancer trascriptomes is still a challenge. In this thesis, we focus on three specific problems in understanding cancer trascriptome and list them below.

Alternative splicing A single gene contains numerous exons and introns, the exons can be spliced together in different ways. Recent studies have estimated that alternative splicing events exist in 92-94% of multi-exon genes in human, resulting in more than one transcript per gene [4]. An example of an alternative splicing event is illustrated in Figure 1.1(A). The gene contains 5 exons, one of the mRNA transcribed from that gene contains exons 1-4 and another contains exons 1-3, and exon 5, which produce two protein isoforms from the same gene. Alternative splicing provides cells with the opportunity to create protein isoforms of differing functions from a single gene. Cancer cells often take advantage of this flexibility that promote growth and survival [5]. Many isoforms produced in this way are developmentally regulated and preferentially re-expressed in tumor [5,6]. Therefore, accurate transcript quantification is crucial and enables us to detect the differences of the alternative transcripts in the gene under different conditions. Its downstream application in detecting molecular signature for cancer can greatly impact biomedical study.

Alternative polyadenylation The 3' end of most protein-coding genes and non-coding RNAs is polyadenylated. Recent studies using transcriptome-wide techniques have revealed that most human or mouse genes contain more than one poly(A) site, indicating alternative polyadenylation (ApA) [7]. Tandem 3' untranslated region (UTR) ApA, illustrated in Figure 1.1(B), involves the occurrence of alternative poly(A) sites within the same terminal exon is one of the most frequent ApA forms. 3'-UTR ApA generates multiple isoforms with different 3'-UTR length without affecting the protein encoded by the gene. It potentially regulates the stability, cellular localization and translation efficiency of target RNAs as 3'-UTR provides a binding platform for microRNAs and RNA-binding proteins. A recently recognized mechanism of oncogene activation is the loss of microRNA complementary sites [8, 9]. Therefore, identifying cancer relevant 3'-UTR shortening events can possibly improve disease prognosis and diagnosis.

Interactions It is well known that gene, transcript or protein isoforms do not function in isolation in the cell, but are integrated together as a network of interactions between

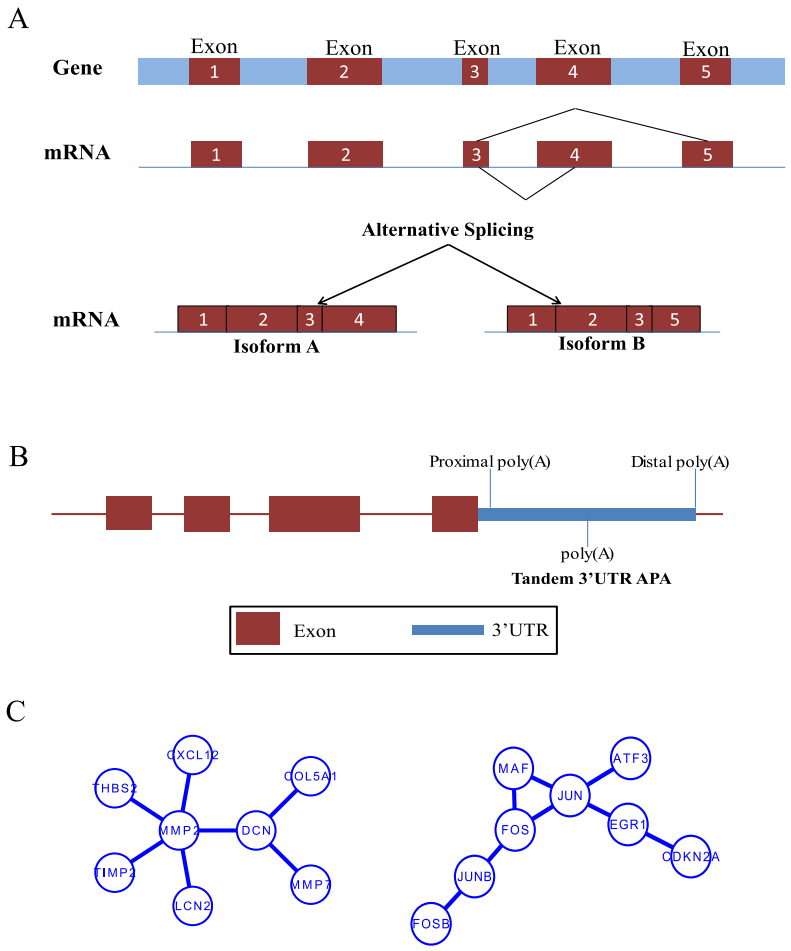

Figure 1.1: **(A) Alternative Splicing, (B)Tandem 3'-UTR Alternative Polyadenylation, and (C) Protein-Protein interaction subnetworks.**

cellular components. Two human protein-protein interaction (PPI) subnetworks obtained from HPRD [10] are shown in Figure 1.1(C). Cancer, as a complex disease, reflects the perturbations or breakdown of specific functional modules in the complex cellular network, rather than a consequence of an abnormality in a single gene [11]. Thus, instead of considering the gene or transcript variant individually in the cancer transcriptome analysis, integrating network and high-throughput information together could probably improve the quality of the analysis [12]. However, due to the complex

and heterogeneous nature of these large-scale datasets, efficient and reliable computational methods that integrate network information for cancer transcriptome analysis are crucially needed.

1.2 Previous Methods

We will review a few fundamental modeling techniques that have been widely used in cancer transcriptome analysis. Our models proposed in this thesis are developed based on these base models. 1) Network propagation, a popular method for feature section by integrating network information into analysis [13–15]; 2) Cox proportional hazard model [16], widely used in survival analysis for biomarker identification and survival prediction; 3) A base Expectation-Maximization(EM) model [17, 18] for transcript quantification with RNA-Seq data.

1.2.1 Network propagation

Let $G = (V, W)$ denote an undirected graph with vertex set V and positive adjacency matrix $W \in \mathbb{R}^{+|V|\times|V|}$. In network propagation, the vertex set V is initialized by a vector y which is the $+1/-1$ label on training vertices and 0 on test vertices in binary classification. In the regularization framework proposed by [13], the objective is to learn a label assignment function $f : V \to \mathbb{R}$ to assign labels to the test vertices. The cost function is defined as follows,

$$\Omega(f) = \sum_{i,j} W_{ij}(\frac{f_i}{\sqrt{D_{ii}}} - \frac{f_j}{\sqrt{D_{jj}}})^2 + \varrho\|f - y\|^2, \tag{1.1}$$

where D is a diagonal matrix with $D_{ii} = \sum_j W_{ij}$ and $\varrho \geq 0$ is a parameter to weight the two terms in the cost function. The first term in Eqn. (1.1) is the *smoothness constraint*, which encourages assigning similar labels to strongly connected vertices. The second term is the *fitting constraint*, which encourages consistency between predictions and training labels. The first term can be rewritten as

$$f'(I - (D)^{-\frac{1}{2}}W(D)^{-\frac{1}{2}})f,$$

where $I - (D)^{-\frac{1}{2}}W(D)^{-\frac{1}{2}}$ is the normalized graph Laplacian, which is positive semi-definite. Thus Eqn. (1.1) is a quadratic problem with a closed-form solution.

In transcriptome analysis, G denotes a gene correlation graph, each vertex represent a gene, and the edge represent the relation between two genes. The initial labels, y, provide the differential expression of each individual gene in the case/control study as the starting point of propagation. After convergence, f gives a new ranking of the genes.

1.2.2 Cox proportional hazard model

Consider the Cox regression model proposed in [16]. Given $\boldsymbol{X}$, the gene expression profile of n patients over p genes, the instantaneous risk of an event at time t for the i^{th} patient with gene expressions $\boldsymbol{X}_i = (X_{i1}, ..., X_{ip})'$ is given by

$$h(t|\boldsymbol{X}_i) = h_0(t)exp(\boldsymbol{X}_i'\boldsymbol{\beta}), \tag{1.2}$$

where $\boldsymbol{\beta} = (\beta_1, ..., \beta_p)'$ is a vector of regression coefficients, and $h_0(t)$ is an unspecified baseline hazard function. In the classical setting with $n > p$, the regression coefficients are estimated by maximizing the Cox's log-partial likelihood:

$$pl(\boldsymbol{\beta}) = \sum_{i=1}^{n} \delta_i \left\{ \boldsymbol{X}_i'\boldsymbol{\beta} - log\left[\sum_{j \in R(t_i)} exp(\boldsymbol{X}_j'\boldsymbol{\beta}) \right] \right\}, \tag{1.3}$$

where t_i is the observed or censored survival time for the i^{th} patient, and δ_i is an indicator of whether the survival time is observed ($\delta_i = 1$) or censored ($\delta_i = 0$). $R(t_i)$ is the risk set at time t_i, i.e. the set of all patients who still survived prior to time t_i. The commonly used Breslow estimator [19] to estimate the baseline hazard $h_0(t)$ is given by

$$\hat{h}_0(t_i) = 1/ \sum_{j \in R(t_i)} exp(\boldsymbol{X}_j'\hat{\boldsymbol{\beta}}). \tag{1.4}$$

The partial likelihood and the Breslow estimator are induced by the total log-likelihood

$$l(\boldsymbol{\beta}, h_0) = \sum_{i=1}^{n} \left\{ -exp(\boldsymbol{X}_i'\boldsymbol{\beta})H_0(t_i) + \delta_i \left[log(h_0(t_i)) + \boldsymbol{X}_i'\boldsymbol{\beta} \right] \right\}, \tag{1.5}$$

with

$$H_0(t_i) = \sum_{t_k \leq t_i} h_0(t_k). \tag{1.6}$$

The optimal regression coefficients $\boldsymbol{\beta}$ is estimated based on the maximization of the total log-likelihood by alternating between maximization with respect to $\boldsymbol{\beta}$ (with Newton-Raphson) and $h_0(t)$ (by equation (1.4)).

1.2.3 Base EM model for transcript quantification

Let $\boldsymbol{T}_i$ denote the set of the transcripts in the ith gene and T_{ik} be the kth transcript in $\boldsymbol{T}_i$. The probability of a read being generated by the transcripts in $\boldsymbol{T}_i$ is modeled by a categorical distribution specified by parameters p_{ik}, where $\sum_{k=1}^{|\boldsymbol{T}_i|} p_{ik} = 1$ and $0 \leq p_{ik} \leq 1$. For the set of the reads $\boldsymbol{r}_i$ aligned to gene i, we consider the likelihood of that each of the $|\boldsymbol{r}_i|$ short reads is sampled from one of the transcripts to which the read aligns. Specifically, for each read r_{ij} aligned to transcript T_{ik}, the probability of obtaining r_{ij} by sampling from T_{ik}, namely $Pr(r_{ij}|T_{ik})$ is $q_{ijk} = \frac{1}{l_{ik}-l_r+1}$ [20–22], where l_r is the length of the read. Assuming each read is independently sampled from one transcript, the uncommitted likelihood function [17] to estimate the parameters $\boldsymbol{P}_i$ from the observed read alignments against gene i is

$$\begin{aligned} \mathcal{L}(\boldsymbol{P}_i; \boldsymbol{r}_i) = Pr(\boldsymbol{r}_i|\boldsymbol{P}_i) = \prod_{j=1}^{|\boldsymbol{r}_i|} Pr(r_{ij}|\boldsymbol{P}_i) &= \prod_{j=1}^{|\boldsymbol{r}_i|} \sum_{k=1}^{|\boldsymbol{T}_i|} Pr(T_{ik}|\boldsymbol{P}_i) Pr(r_{ij}|T_{ik}) \\ &= \prod_{j=1}^{|\boldsymbol{r}_i|} \sum_{k=1}^{|\boldsymbol{T}_i|} p_{ik} q_{ijk}. \end{aligned} \tag{1.7}$$

This likelihood function is concave but it may contain plateau in the likelihood surface. Therefore, Expectation Maximization (EM) is then applied to obtain the optimal $\boldsymbol{P}_i$. In the EM algorithm, the expectation of read assignments to transcripts were estimated in the E-step and the likelihood function with the expected assignments can be maximized in the M-step to estimate $\boldsymbol{P}_i$. The relative abundance of the transcript T_{ik} in gene i, ρ_{ik}, can be derived from

$$\rho_{ik} = \frac{\frac{p_{ik}}{l_{ik}}}{\sum_{k=1}^{|\boldsymbol{T}_i|} \frac{p_{ik}}{l_{ik}}}, \tag{1.8}$$

and the transcript expressions in gene i, π_{ik}, can be calculated by

$$\pi_{ik} = \frac{|r_i| p_{ik}}{l_{ik}}. \tag{1.9}$$

The base model is applied independently to each individual gene and no relation among the transcripts is considered.

1.3 Challenges and Objectives

As shown above, many statistical and machine learning methods have been developed to quantify the transcript/gene expression [23,24], discover gene and transcript variants as molecular signatures (biomarkers) [2,25], and predict survival in patients with potential clinical value [26], but building reliable learning models for estimating the isoform expression and discovering consistent biomarkers for prediction of clinical outcomes using high-throughput dataset is still a key challenge in transcriptome analysis.

- Many of the current approaches for biomarker discovery and survival prediction are based on univariate statistical analysis such as the Cox regression model (equation (1.3)). There are two major limitations of these popular methods. First, the genomic features are ranked by their individual correlation with the phenotype. In complex diseases, such as cancer is believed to be caused by the interactions of multiple genes as well as environmental factors, which can not be captured by traditional univariate analysis. Though network propagation algorithms (equation (1.1)) can overcome this limitation, they only work on positively weighted graphs. Second, usually all the samples are used to compute the correlation with phenotype, and thus biomarkers specific to only a subset of the samples are not detectable [27].

- In current isoform quantification methods for RNA-Seq data analysis, solely based on short read alignment could be overly optimistic to derive the proportion of the isoforms of a gene such as the base EM model (equation (1.7)). First, in the aligned RNA-Seq short reads, most reads mapped to a gene are potentially originated by more than one transcript [28]. The ambiguous mapping could result in hardly identifiable patterns of transcript variants [29]. Second, various sampling biases have been observed regularly in RNA-Seq data from library preparation, include position-specific bias, start and end biases, and sequences-specific bias. How to get accurate transcript quantification remains a challenging problem.

- Approximately 70% genes [30] are characterized by multiple polyA sites that produce distinct transcript isoforms with different 3'-UTR length and content, thereby significantly contributing to transcriptome diversity [31]. However, methods to

quantify relative ApA usage are still limited. Besides that, very few RNA-seq reads contain polyA tails, challenging our ability to identify ApA events in gene. For example, an ultra-deep sequencing study [32] only identified ∼40 thousand putative polyA reads (∼0.003%) from 1.2 billion total RNA-seq reads [33]. Moreover, the precise mechanism(s) of ApA events is unknown [34].

1.4 Contributions

To address the challenges described above, we propose four different models and studies in this thesis.

First, we introduce signed network propagation frameworks for detecting consistent biomarkers [27]. The first framework runs network propagation on a gene graph weighted by both positive and negative gene co-expression for gene selection from gene expression datasets. It integrates gene co-expression and differential expression to explore gene modules which overcome the limitation of the biomarker identification models based on univariate statistical analysis. The second framework runs network propagation on sample-feature bipartite graphs linked by both positive and negative features to identify gene or CNV markers. The framework explores bi-clusters between patients and features to find biomarkers specific to subsets of patient samples.

Second, we propose a network-based Cox proportional hazard model to explore the co-expression or functional relation among gene expression features for survival analysis [35], which to our knowledge is among the first models that directly incorporate network information in survival analysis. A gene relation network constructed by co-expression analysis or prior knowledge of gene functional relations models the relationship between genes. In the model, a graph Laplacian constraint is introduced as a smoothness requirement on the gene features linked in the gene relation network. The model identified consistent signature genes across the three ovarian cancer datasets, and because of the better generalization across the datasets, the model also consistently improved the accuracy of survival prediction over the Cox models regularized by L_2-norm or L_1-norm.

Third, we examine the possibility of using protein domain-domain interactions as

prior knowledge in isoform transcript quantification to overcome the limitation of sampling bias from RNA-Seq data [36]. We first made the observation that protein domain-domain interactions positively correlate with isoform co-expressions in TCGA data and then designed a probabilistic EM approach to integrate domain-domain interactions with short read alignments for estimation of isoform proportions. In simulation, the approach effectively improved isoform transcript quantifications when isoform co-expressions correlate with their interactions. qRT-PCR results on 25 multi-isoform genes in a stem cell line, ovarian cancer cell line, and a breast cancer cell line also showed that the approach estimated more consistent isoform proportions with RNA-Seq data. In the experiments on the RNA-Seq data in TCGA, the transcript abundances estimated by the approach are more informative for patient sample classification of ovarian cancer, breast cancer and lung cancer.

Last, we developed a pipeline to identify the transcriptome-wide ApA events with RNA-Seq data in mouse embryonic fibroblast (MEF) [34]. To detect the events, we evaluated candidate polyA signal (PAS) motifs in the 3'-UTR of the transcript by contrasting the short-read coverage up/downstream of the site across wild-type (WT) and TSC1$^{-/-}$ MEFs with χ^2-test. To our knowledge, this is one of the first comprehensive analysis of transcriptome-wide ApA events with RNA-Seq data. Besides that, in this study we investigate the molecular signatures of mammalian target of rapamycin (mTOR) activated transcriptome and discovered widespread 3'-UTR shortening due to dysregulated mTOR activation. Moreover, we found almost all known 3'-end processing factors alter their expression on changes in cellular mTOR activity in TSC1$^{-/-}$ compared with WT MEF.

1.5 Data Repositories

In this thesis, we utilized public high-throughput genomic data from several sources. All the processed RNA-Seq and microarray data were downloaded from The Cancer Genome Atlas (TCGA) data portal and the Gene Expression Omnibus (GEO) repository. The raw RNA-Seq fastq files were downloaded from Cancer Genomics Hub (CGHub) under National Cancer Institute (NCI) and Sequence Read Archive (SRA) under National Center for Biotechnology Information (NCBI).

- TCGA project (`http://cancergenome.nih.gov/`) profiled and analyzed large numbers of human tumors to discover molecular aberrations at the DNA, RNA, protein and epigenetic levels. The resulting rich data provide a whole picture to understand the molecular basis of cancer. TCGA data portal (`https://tcga-data.nci.nih.gov/tcga/dataAccessMatrix.htm`) provides a platform for researchers to search, download, and analyze data sets generated by TCGA. We downloaded the normalized RNA-Seq and microarray gene expression and transcript expression data of four cancer types from the data portal.

- CGHub (`https://cghub.ucsc.edu/`) is the online repository of the sequencing programs of the NCI, including The Cancer Genomics Atlas (TCGA) project [37]. The raw RNA-Seq fastq files of the cancer patients in four cancer types listed in TCGA were downloaded from the CGHub online repository.

- GEO (`http://www.ncbi.nlm.nih.gov/geo/`) is a public repository that archives and freely distributes microarray, next-generation sequencing, and other forms of high-throughput functional genomic data submitted by the scientific community [38]. We downloaded two ovarian cancer microarray gene expression datasets, five breast cancer microarray gene expression datasets from the GEO repository.

- SRA (`http://www.ncbi.nlm.nih.gov/sra`) stores raw sequence data from next-generation sequencing technologies. Two raw RNA-Seq fastq files of breast cancer cell line and stem cell line were downloaded from the SRA database.

Besides above, our collaborators at University of Kansas Medical Center and University of Minnesota also provided in-house data of ovarian cancer cell line and mouse cell line for the studies.

1.6 Outline

The rest of the thesis is organized as follows:

- In Chapter 2, we describe two signed network propagation algorithms, *Signed-NP* and *Signed-NPBi*, consider both positive and negative relation in graphs to model

gene up/down-regulation or amplification/deletion CNV events for detecting differential gene expressions and DNA CNVs.

- In Chapter 3, we describe a network-based Cox regression model called *Net-Cox*, integrates gene network information into the Cox's proportional hazard model to explore the co-expression or functional relation among high-dimensional gene expression features in the gene network for biomarker identification and survival prediction.

- In Chapter 4, we describe a network-based probabilistic EM approach, *Net-RSTQ*, to integrate domain-domain interations with short read alignments for estimation of isoform proportions.

- In Chapter 5, we identifie 3'-UTR shortening of mRNAs as an additional molecular signature of mTOR activation and show that 3'-UTR shortening enhances the translation of specific mRNAs.

- In Chapter 6, we summarize the findings of the thesis and suggesting directions for future work.

Chapter 2

Signed Network Propagation for Cancer Biomarker Analysis

2.1 Introduction

Powered by high-throughput genomic technologies, it is now a common practice to perform genome-scale experiments for measuring gene expressions, copy number variations (CNVs), single nucleotide polymorphisms, and other molecular information for cancer studies. Correlating these high-dimensional genomic features with cancer phenotypes as molecular signatures (biomarkers) can possibly improve prognosis and diagnosis over current clinical measures for risk assessment of patients [2,39,40]. The most widely used statistical methods to detect biomarkers are Pearson correlation coefficients [2] and hypothesis test methods such as student t-test. There are two major limitations of these popular methods. First, the genomic features are ranked by their individual correlation with the phenotype, and thus relations among features, for example co-expressed genes under certain conditions and adjacent probes involved in the same CNV events, are ignored. Second, usually all the samples are used to compute the correlation with phenotype, and thus biomarkers specific to only a subset of the samples are not detectable.

Network propagation is a graph-based learning algorithm [13] similar to PageRank

used by Google. It has been shown that network propagation is capable of capturing the dependence among genomic features to detect correlated features as biomarkers [14, 15]. An efficient network propagation algorithm on bipartite graphs was introduced to explore sample-feature bi-clusters for feature selection and cancer outcome classification [41]. In the network propagation regularization framework, a quadratic term with a normalized graph Laplacian matrix as hessian is combined with a square-loss on the predictions to explore the global graph structure for capturing correlation between all genomic features. The graph Laplacian matrix is only defined for positively weighted graphs which poses a significant limitation on the applicability of network propagation to the analysis of genomic data. For example, gene expression data could require a precise representation of up-regulated expression or down-regulated expression, and CNV data require a precise representation of amplification or deletion events. In these real computational biology problems, genomic data are represented by signed graphs to incorporate both positive and negative relations and thus the existing network propagation algorithms are not applicable.

To address the problem, we propose two signed network propagation algorithms and regularization frameworks for detecting differential gene expressions and DNA copy number variations. In the frameworks, we introduce signed graph Laplacians into network propagation. The first algorithm, Signed-NP, runs network propagation on a gene graph weighted by both positive and negative gene co-expressions for gene selection from gene expression datasets. Signed-NP integrates gene co-expressions and differential expressions to explore gene modules. The second algorithm, Signed-NPBi, runs network propagation on sample-feature bipartite graphs linked by both positive and negative features to identify gene or CNV markers. Signed-NPBi explores bi-clusters between patients and features to find biomarkers specific to subsets of patient samples.

2.2 Method

Based on the network propagation model described in section 1.2.1. We first introduce signed network propagation (Signed-NP) in section 2.2.1 and its extension for propagation on bipartite graphs (Signed-NPBi) in section 2.2.2. In section 2.2.3 and section

2.2.4 we apply Signed-NP on gene correlation graphs for detecting differential gene expressions, and Signed-NPBi on sample-feature bipartite graphs for gene selection or CNV detection respectively.

2.2.1 Signed Network Propagation

To allow both positive and negative edges for network propagation, we introduce signed graph Laplacian [42] into the regularization framework. Given a signed graph $G = (V, W)$ with vertices V and adjacency matrix $W \in \mathbb{R}^{|V|\times|V|}$. The cost function of the regularization framework is modified as follows,

$$\Omega(f) = \sum_{i,j} |W_{ij}|(\frac{f_i}{\sqrt{D_{ii}}} - sgn(W_{ij})\frac{f_j}{\sqrt{D_{jj}}})^2 + \varrho\|f - y\|^2, \tag{2.1}$$

where $D_{ii} = \sum_j |W_{ij}|$. The first term in Eqn.(2.1) is the normalized signed graph Laplacian $I - S$, where $S = D^{-\frac{1}{2}} * W * D^{-\frac{1}{2}}$. It has been shown in [42] that the signed graph Laplacian is always positive semi-definite. The first cost term encourages assigning similar labels to vertices connected by positive edges and opposite labels to the vertices connected by negative edges. Empirically, the eigenvalues of S can be very small. For better performance in network propagation, we rescale S by dividing the largest eigenvalue such that S's eigenvalues are in the range $[-1, 1]$. Similar to the algorithm proposed by [13], the optimization framework in Eqn.(2.1) can be solved with an iterative label propagation algorithm,

$$f^t = (1 - \alpha)y + \alpha S f^{t-1}, \tag{2.2}$$

where t denotes the propagation step and $\alpha = 1/(1 + \varrho)$. The parameter α balances the weights between initial label and network structure. The larger the α, the more we trust the network structure. This algorithm simply propagates labels among the neighbors in the graph. The algorithm will converge to the closed-form solution

$$f^* = (1 - \alpha)(I - \alpha S)^{-1} * y, \tag{2.3}$$

where f^* assigns labels to the vertices.

2.2.2 Propagation on Signed Bipartite Graph

We next extend the framework in Eqn.(2.1) for signed bipartite graphs. Let $G = (V, U, E, W)$ denote a signed bipartite graph, where V and U represent two disjoint vertex sets, E is a set of weighted edges, and $W \in \mathbb{R}^{V \times U}$ is the wighted adjacency matrix. Each edge $(v, u) \in E$ connects two vertices v and u with weight W_{vu}. The initialization function y for the two vertex sets are denoted by $y(v)$ and $y(u)$. In this context, the cost function over $G = (V, U, E, W)$ is defined as

$$\begin{aligned} \Omega(f) &= 2 \sum_{(v,u)\in E} |W_{vu}|(\frac{f(v)}{\sqrt{D_{vv}}} - sgn(W_{vu})\frac{f(u)}{\sqrt{D'_{uu}}})^2 \\ &\quad +\varrho\|f(v) - y(v)\|^2 + \varrho\|f(u) - y(u)\|^2, \end{aligned} \tag{2.4}$$

where $\varrho \geq 0$ is a parameter for balancing the cost terms, and D and D' are diagonal matrices with $D_{vv} = \sum_{u\in U} |w(v, u)|$ and $D'_{uu} = \sum_{v\in V} |w(v, u)|$. The first cost term encourages similar labeling on positively connected vertex pairs and opposite labeling on negatively connected pairs. The second term and the third term constrain the new label assignment to be consistent with the initial labeling. To solve the optimization problem in Eqn.(2.4), we can also use a similar network propagation algorithm to compute the closed-form solution. The propagation algorithm iteratively performs propagation between the two vertex sets in both directions as follow,

$$f(v)^t = (1 - \alpha)y(v) + \alpha S f(u)^{t-1}$$
$$f(u)^t = (1 - \alpha)y(u) + \alpha S f(v)^{t-1}$$

where $\alpha = 1/(1+\varrho)$, $S = D^{-\frac{1}{2}} * W * D'^{-\frac{1}{2}}$, and t denotes the propagation step. S is also similarly rescaled by dividing the largest eigenvalue. Label information is propagated through neighbors in the bipartite graph. The algorithm will converge to the closed-form solution as in Eqn.(2.3).

2.2.3 Learning with Gene Correlation Graph

We first apply Signed-NP to a gene correlation graph for identifying differentially expressed genes. An illustrative example of network propagation on a gene correlation graph $G = (V, W)$ is shown in Figure 2.1. Each vertex in V represents a gene which

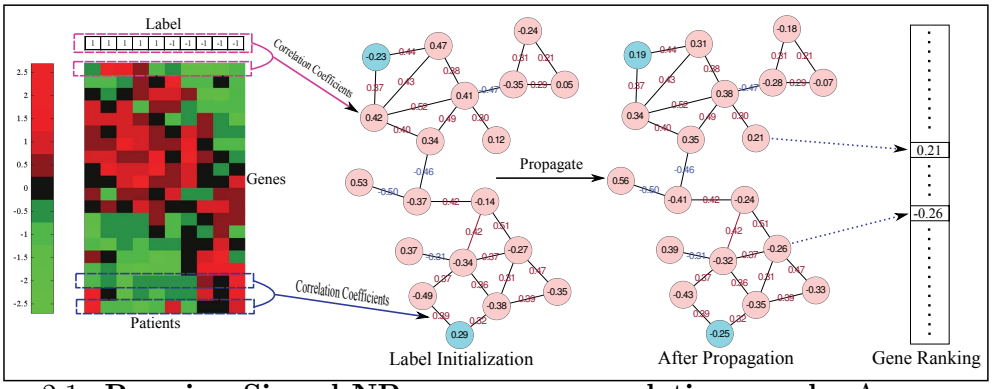

Figure 2.1: **Running Signed-NP on a gene correlation graph.** A gene correlation graph is constructed from gene expression data. The vertices are then initialized by the correlation between each individual gene expression and the labels. Network propagation on the signed graph re-rank all the genes for biomarker discovery.

is initialized by Pearson's correlation coefficients between gene expressions and the case/control labeling. An example of calculating the correlation between gene expression and labels is given in the pink rectangles in the figure. The initial labels provide the differential expression of each individual gene in the case/control study as the starting point of propagation. Each W_{ij} is the Pearson's correlation coefficients between gene expressions of gene i and gene j. An example of computing the correlation between gene expressions is given in the blue rectangles in the figure. Signed-NP propagates the initial labels across the network and the propagation process assigns similar labels to genes that are positively co-expressed and opposite labels to genes with opposite expression. The intuition is that we assume marker genes are active either in the case group or the control group but never both. Thus, the positive edges play the role to join positively co-expressed genes and the negative edges play the role to distinguish the genes with opposite expressions. After network propagation, the genes are re-ranked by the magnitude from positive to negative. Figure 2.1 shows how label propagation can capture the hidden clusters to recover false negatives and eliminate false positives. In the example, we assume two hidden clusters in the network, one of which contains a gene with initial value -0.23 and the another contains a gene with initial value 0.29 (the two cyan nodes). After running label propagation, final scores are assigned by balancing their coherence and discrimination so that genes in the same cluster are assigned similar scores.

2.2.4 Learning with Sample-Feature Bipartite Graph

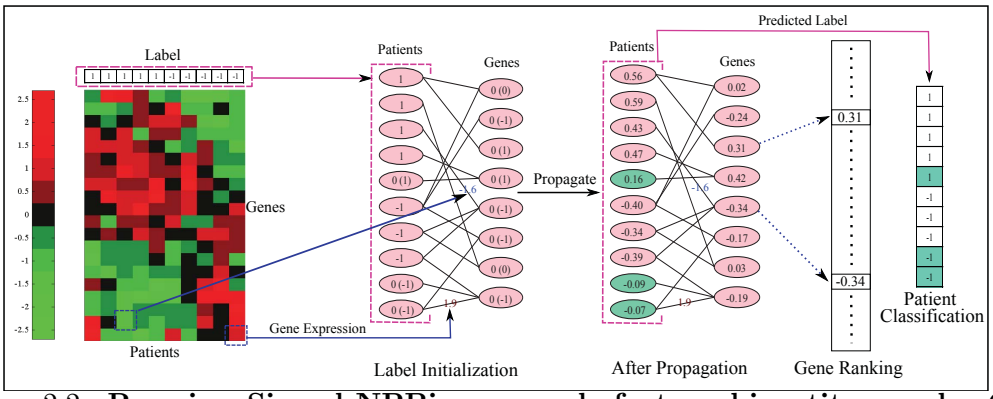

Figure 2.2: **Running Signed-NPBi on sample-feature bipartite graph.** Gene expression data is modeled as a sample-feature bipartite graph. The sample vertices are initialized by the case/control labels and the gene vertices are initialized with 0. Network propagation classifies the unlabeled samples and ranks the genes by their importance.

We next apply Signed-NPBi to gene expression and CNV data for both genomic feature selection and sample classification. Gene expression data is modeled by a sample-feature bipartite graph $G = (V, U, E, W)$ as illustrated in Figure 2.2, where V represents the set of sample vertices and U represents the set of gene vertices. Each edge $(v, u) \in E$ connects sample vertex $v \in V$ and gene vertex $u \in U$ weighted by W_{vu} as is illustrated by the blue rectangles. The sample vertices in V are labeled with +1/-1/0 (case/control/unlabeled) as illustrated by the pink rectangle and the gene vertices are initialized with zeros. In this modeling, Signed-NPBi explores those bi-cluster composed of vertices with opposite labels and connected with negative edges as well as vertices with similar labels and connected with positive edges. As explained in the signed graph model in Eqn.(2.4), the first term in the cost function constrains new labeling to be consistent between the positively connected sample-gene pairs and opposite between the negatively connected sample-gene pairs. The second term is a fitting term which keeps the new label assignment for each sample consistent with the initial label. For the unlabeled vertices $v \in V$ with $y(v) = 0$, the second term is used to regularize these $f(v)$s such that the total cost is constrained. The third term is used in the same spirit to constrain the cost on the gene vertices. The final scores obtained after convergence are used to rank the genes as well as classify additional test (unlabeled) samples. In

Figure 2.2 the optimal labels are given in parentheses. After running network propagation, the genes in bi-clusters will receive more significant values. Note that if connected by negative edges, the sample and the gene will receive opposite labels. Since the important genes are strongly connected to either the case group or the control group we can consider the genes with significant scores within the bi-clusters as biomarkers. The unlabeled samples are also classified to different groups based on the sign of the final score for each sample.

Similarly, we can also apply the signed bipartite graph model to copy number variation data. Each probe feature is represented by a vertex in U connected to the samples with an edge weighted by the log intensity ratio of the probe. After network propagation, those probes with high scores are selected as important CNV regions. In CNV analysis the adjacent probes tend to be strongly correlated, thus the bi-clusters in the bipartite graph represent a continuous CNV regions across a subset of samples.

2.3 Experiments

In the experiments, we tested Signed-NP on 5 breast cancer gene expression datasets to detect differentially expressed genes and Signed-NPBi on two breast cancer gene expression datasets and one bladder cancer arrayCGH dataset to detect both differentially expressed genes and copy number variations.

2.3.1 Biomarker Identification from Gene Correlation Graph

GEO Index **Study**	GSE1456 Pawitan	GSE2034 Wang	GSE3494 Miller	GSE6532 Loi	GSE7390 Desmedt
# of Meta	35	95	37	51	35
# of Meta-free	35	114	150	96	136

Table 2.1: Samples in five breast cancer datasets.

Preparing breast cancer datasets

We collected five independent microarray gene expression datasets generated for studying breast cancer metastasis. The five datasets were generated by the Affymetrix HG-U133A platform. The raw .CEL files were downloaded from the GEO website: Pawitan (GSE1456), Wang (GSE2034), Miller (GSE3494), Loi (GSE6532), and Desmedt

(GSE7390) [43–47], and normalized by RMA [48]. After merging probes by gene symbols and removing probes with no gene symbol, a total of 13,261 unique genes derived from the 22,283 probes were included in our study. The patients are classified as cases and controls in the five datasets based on the time of developing distant metastasis. The patients who were free of metastasis for longer than eight years of survival and follow-up time were classified as metastasis-free and the patients who developed metastases within five years were classified as metastasis cases. The number of selected samples are reported in Table 2.1.

Classification performance

		Test Dataset				
Training Dataset	Method	GSE1456	GSE2034	GSE3494	GSE6532	GSE7390
GSE1456	Signed-NP		0.5985	0.6591	**0.6480**	**0.7247**
	NP		0.5827	0.6544	0.6424	0.6839
	Correlation Coefficients		**0.6019**	**0.6600**	0.6464	0.7070
GSE2034	Signed-NP	0.7830		**0.6183**	**0.7222**	**0.7471**
	NP	**0.7874**		0.6147	0.7186	0.7398
	Correlation Coefficients	0.7832		0.6174	0.7218	0.7361
GSE3494	Signed-NP	0.7940	**0.6410**		**0.6712**	**0.7492**
	NP	**0.7981**	0.6334		0.6699	0.7311
	Correlation Coefficients	0.7841	0.6165		0.6641	0.7209
GSE6532	Signed-NP	**0.7940**	**0.6332**	**0.6576**		**0.7380**
	NP	0.7867	0.6001	0.6409		0.6807
	Correlation Coefficients	0.7840	0.6298	0.6481		0.7006
GSE7390	Signed-NP	0.8103	**0.6357**	**0.6672**	0.6573	
	NP	0.8077	0.6177	0.6629	0.6510	
	Correlation Coefficients	**0.8150**	0.6232	0.6614	**0.6592**	
	Random	0.7475	0.6118	0.5883	0.6264	0.6229

Table 2.2: Evaluating marker genes across breast cancer datasets. Markers selected on the training dataset are used as features in the cross-validation on the test dataset. The best results are bold.

We applied Signed-NP, network propagation (NP), and Pearson's correlation coefficient (CC) to identify markers from each of the five breast cancer datasets. To test NP on a graph with positively weighted edges the network was constructed by setting the weights of the edges to the absolute value of the Pearson's correlation coefficients between the gene pairs and the vertices were initialized by the Pearson's correlation coefficients between gene expressions and the case/control labeling. To evaluate the predictive power of the marker genes we performed a cross-dataset validation. Specifically, we selected the markers genes for Signed-NP and CC from the top 50 up-regulated and 50

down-regulated genes and from the top 100 genes for NP from the training dataset, and evaluated the marker genes on the remaining datasets as test sets. The gene expressions of the marker genes were used as features for cross-validation on the test dataset. We evaluated the classification performance using a Support Vector Machine (SVM) [49] with an RBF kernel. Classification performance was evaluated using a receiver operating characteristic (ROC) score [50]. We reported the mean of the ROC score after repeating 100 times five fold cross validation. We compared the predictive power of the marker genes selected by Signed-NP, NP, and CC. To add a random baseline, we also randomly selected 100 genes and tested with five-fold cross-validation 1000 times. The results are reported in Table 2.2 with $\alpha = 0.5$ for Signed-NP where the bold numbers represent the best ROC score by the three methods. Signed-NP outperformed both NP and CC in 14 out of 20 cases and NP alone in 18 cases. Signed-NP is clearly more capable of selecting more predictive marker genes in the experiments.

Consistency of marker genes across datasets

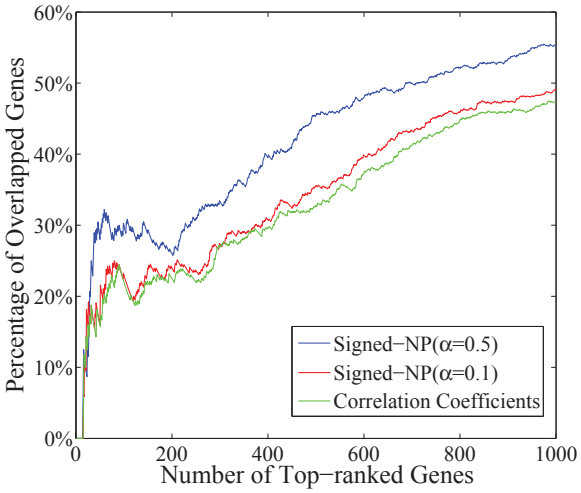

Figure 2.3: **Marker gene consistency across five breast cancer gene list.** The x-axis is the number of selected marker genes ranked by each method. The y-axis is the percentage of the overlapped genes between the selected markers across at least three of the breast cancer datasets.

To measure how consistent the selected marker genes are across the five independent

datasets, we report the percentage of common genes identified by a method in the rank lists from the datasets. This measurement assumes that the true marker genes are more likely to be selected in each dataset than the other genes. Thus, higher consistency across the datasets might indicate higher quality in gene marker selection. We plot the percentage of common genes among the first k (up to 1000) genes in the gene ranking lists from at least three of the datasets. We show the results of up-regulated genes in Figure 2.3. The network propagation method Signed-NP with parameter $\alpha = 0.5$ clearly identifies significantly more reproducible marker genes than CC. For example, Signed-NP identified 31 common genes among the first 100 genes in the gene ranking lists and CC only identified 24 common genes since CC only considers each feature independently. NP produced similar consistency in the marker genes compared with Signed-NP since both NP and Signed-NP capture the more conserved gene co-expressions.

PPI subnetworks and enriched GO terms.

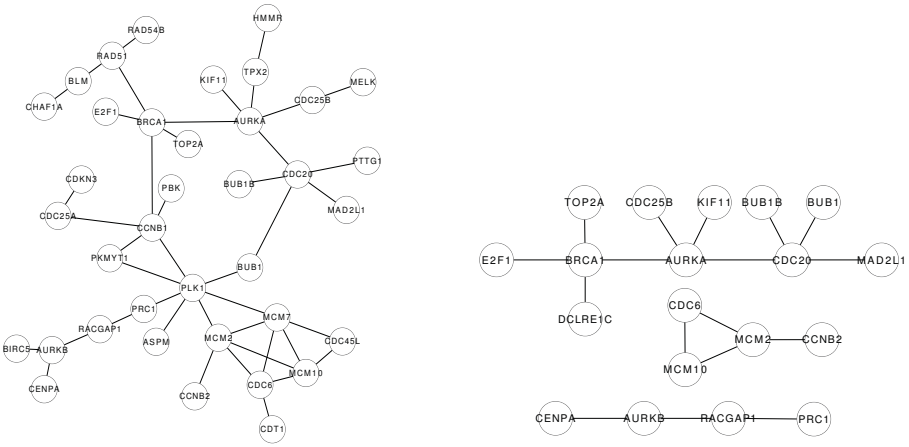

(A)Signed-NP (B)Correlation Coefficients

Figure 2.4: **Protein-Protein interaction subnetworks of signature genes identified by Signed-NP and Correlation Coefficients on the Desmedt dataset.** (A) The PPI subnetworks identified by Signed-NP. (B) The PPI subnetworks identified by Correlation Coefficients.

The top 100 marker genes identified by Signed-NP and CC in the Desmedt (GSE7390) [47] dataset were mapped to the human protein-protein interaction (PPI) network

obtained from HPRD [10] and also analyzed with the DAVID functional annotation tool [51]. We report the densely connected PPI subnetworks constructed from the top 100 up-regulated genes selected by Signed-NP in Figure 2.4(A). The subnetwork contains 37 genes and 43 connections between the genes. Compared with the PPI subnetwork generated from the marker genes selected by CC in Figure 2.4(B), which contain 19 genes and 17 connections, the subnetwork is larger and denser. In Figure 2.4(A), HMMR and RAD51 were reported as oncogenes of breast cancer in Online Mendelian Inheritance in Man (OMIM) [52], neither of which was detected by CC. Women with a variation in the HMMR gene had a higher risk of breast cancer even after accounting for mutations in the BRCA1 or BRCA2 genes. In particular, the risk of breast cancer in women under age 40 who carry the HMMR variation was 2.7 times higher than the risk in women without this variation [53]. RAD51 interacts with the evolutionarily conserved BRC motifs in the human breast cancer susceptibility gene BRCA2 [54]. In addition, the genes MAD2L1, RAD51, AURKA, BRCA1, BUB1, BUB1B, CDT1, and PTTG1 are listed on the breast cancer gene list in Genetic Association Database (GAD) [55]. Furthermore, the 37 marker genes in the subnetwork are also enriched by cell cycle process, nuclear division, DNA replication, DNA metabolic process, and ATP binding, all of which are well-known cancer relevant GO functions.

The top 100 signature genes identified by Signed-NP enriched 83 GO functions (p-value¡0.01) and the ones identified by CC only enriched 47 GO functions. The most significantly enriched GO functions are listed in Table 2.3. It is clear that Signed-NP identified signature genes that are more functionally coherent.

2.3.2 Genomic Feature Selection on Sample-feature Bipartite Graphs

Data Preparation

We prepared two microarray gene expression datasets [1,2] to study breast cancer metastasis and one arrayCGH dataset to study bladder cancer [56]. The dataset (Rosetta) in [2] measures expression profiles of 24,481 genes generated by Agilent oligonucleotide Hu25K microarrays. This dataset contains 97 patient samples among which 51 patients were free of disease after their diagnosis for an interval of at least 5 years (good outcome) and 46 patients had developed distant metastasis within 5 years (poor outcome). The

GO terms	Signed-NP	Correlation Coefficients
cell cycle	38.382	21.419
cell cycle process	34.078	19.295
cell cycle phase	32.805	17.377
M phase	32.329	17.547
mitotic cell cycle	31.849	17.468
mitosis	27.777	15.157
nuclear division	27.777	15.157
M phase of mitotic cell cycle	27.534	14.994
organelle fission	27.236	14.794
cell division	19.805	12.449
organelle organization	19.072	13.072
spindle	18.723	12.557
microtubule cytoskeleton	14.743	X
chromosome	14.389	X
nuclear part	14.028	X
regulation of cell cycle	13.611	X
cellular component organization	13.389	X
DNA replication	12.282	X
intracellular non-membrane-bounded organelle	12.091	X
non-membrane-bounded organelle	12.091	X
intracellular organelle part	11.667	X
organelle part	11.530	X
condensed chromosome	10.774	X
nucleus	10.529	X
chromosomal part	10.397	X

Table 2.3: **Enriched GO terms by the signature genes.** The **p**-values in $-\mathbf{log_{10}}$ scale are shown for the enriched GO terms. A "X" denotes a **p**-value larger than $\mathbf{1 \times 10^{-10}}$.

Vijver [1] dataset contains microarray gene expressions produced by the same technique for generating the Rosetta dataset on 295 samples (194 with good outcome and 101 with poor outcome). The two datasets were chosen for the experiment because Agilent array data by default report up/down-gene expression with positive and negative values for testing Signed-NPBi. The RMA normalized Affymetrix arrays used in the previous experiments usually contain absolute intensities. To avoid additional processing of the data, the five Affymetrix datasets were not used in this experiment. The arrayCGH dataset Blaveri [56] was generated with a HumanArray 2.0 array consisting of 2,464 probes at 1.5Mb resolution. After pruning, the dataset contained 98 samples and 2,142 probes. We classified the patient samples by the tumor stage.

Signed-NPBi was compared against SVM with linear and RBF kernels and the bipartite network propagation algorithm (NPBi) [41]. To apply NPBi, each feature in the datasets was split into two features to represent the positive portion and the negative portion in the original features. The parameter α for both Signed-NPBi and NPBi was chosen from $\{0.95, 0.5, 0.1\}$ in the analysis.

Algorithm	Rosetta	Vijver
Signed-NPBi	**0.7374**	0.6682
NPBi	0.7290	0.6162
SVM(linear)	0.7072	0.6708
SVM(RBF)	0.7030	**0.6830**

Table 2.4: The mean AUC scores of classifying patients with good/poor prognosis in the Rosetta and Vijver gene expression datasets.

Classification of gene expressions

Signed-NPBi was tested on the two breast cancer gene expression datasets. We performed four-fold cross-validation on each of the two datasets with two folds for training, one fold for validation, and one fold for testing. We first initialized the patient labels in the validation fold to zero and combined the training folds to learn the model and tune the best regularization parameter α. The results on the test fold with the optimal α are reported to measure the prediction performance. We repeated the four-fold cross-validation 100 times on each dataset for Signed-NPBi, NPBi, and SVM (linear and RBF kernel) with the same setting. The mean AUC scores for classifying patients in the test fold are shown in Table 2.4. The results on the Rosetta dataset in Table 2.4 show that Signed-NPBi outperformed both NPBi and SVM with linear or RBF kernel. On the Vijver dataset, Signed-NPBi also performed better than NPBi. Although the SVMs get better classification performance on Vijver dataset, Signed-NPBi also performed reasonably well. The results support that network propagation on signed bipartite graphs improved classification over propagation on positively weighted graphs.

Classification of CNV data

Algorithm	AUC
Signed-NPBi	**0.8654**
NPBi	0.8306
SVM(linear)	0.8565
SVM(RBF)	0.8585

Table 2.5: The mean AUCs of classifying patients by tumor stage in the bladder cancer CNV dataset.

We then evaluated Signed-NPBi on the bladder cancer CNV dataset (Blaveri). The cross-validation setup in this experiment was the same as the setup in section 2.3.2. The mean AUCs are reported in Table 2.5. Signed-NPBi also outperformed NPBi and SVMs.

Interpretation of CNV Detection with Signed-NPBi

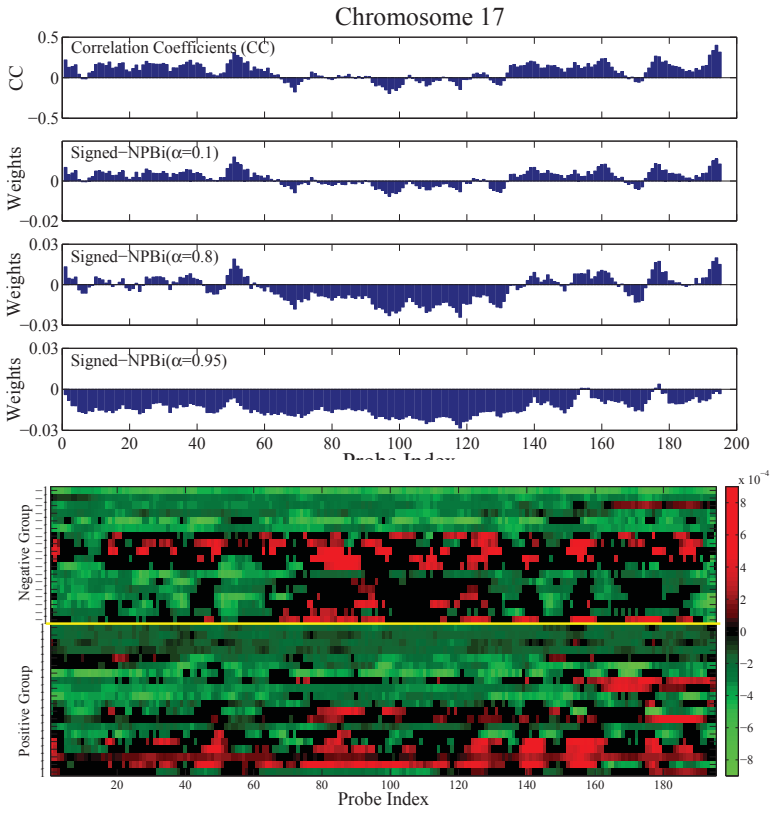

Figure 2.5: **CNV weights learned by Signed-NPBi and Correlation Coefficients and the CNV data on Chromosome 17.**

Finally, we evaluated how well Signed-NPBi smooths the CNV data in order to remove noise and identify bi-clusters. Signed-NPBi smooths the weighting of adjacent probes since the probes in proximity are more likely to be correlated. To demonstrate the smoothing effect we plot the weights of CNVs on chromosome 17 obtained by Signed-NPBi and Correlation Coefficients in the top half of Figure 2.5. In the region between probe index 60-135, CC and Signed-NPBi with $\alpha = 0.1$ detected low association with

tumor stage while Signed-NPBi with $\alpha = 0.8$ and $\alpha = 0.95$ detected a negative association. By examining the probe log-intensity-ratios across the patients shown in the bottom half of Figure 2.5, we can confirm an amplification bi-cluster within the negative group in this region which was not captured by CC or Signed-NPBi with small α. This example shows the strength of Signed-NPBi to recover hidden bi-clusters in CNV data by taking into account the dependence between nearby probes.

2.4 Discussion

In this study, we present network propagation models on signed graphs for feature selection and classification in high-dimensional microarray gene expression and copy number variation data. Network propagation is a promising approach to explore modular structures such as clusters or bi-clusters hiding in high-dimensional data. The signed network propagation models are a useful and important generalization for modeling positive and negative relations in biological networks.

Since network propagation methods explore graph structures they are usually more computationally demanding compared with other simpler feature selection methods. Our future work will focus on developing approximations based on sparse structures to improve efficiency. In addition, we also plan to further investigate other regularizations of the signed graph Laplacian to improve the applicability and flexibility of the models.

Chapter 3

Network-based Survival Analysis on Ovarian Cancer

3.1 Introduction

Survival analysis is routinely applied to analyzing microarray gene expressions to assess cancer outcomes by the time to an event of interest [57–59]. By uncovering the relationship between gene expression profiles and time to an event such as recurrence or death, a good survival model is expected to achieve more accurate prognoses or diagnoses, and in addition, to identify genes that are relevant to or predictive of the events [60,61]. The Cox proportional hazard model [16] is widely used in survival analysis because of its intuitive likelihood modeling with both uncensored patient samples and censored patient samples who are event-free by the last follow-up. Due to the high dimensionality of typical microarray gene expressions, the Cox regression model is usually regularized with penalties such as L_2 penalty in ridge regression [62–65], L_1 Lasso regularization [26,66–70] and L_2 regularization in Hilbert space [71]. While those penalties were designed as a statistical or algorithmic treatment for the high-dimensionality problem, these Cox models are still prone to noise and overfitting to the low sample size. An important prior information that has been largely ignored in survival analysis is the modular relations among gene expressions. Groups of genes are co-expressed under certain conditions or their protein products interact with each other to carry out a biological function. It has been shown that protein-protein interaction network

or co-expressions can provide useful prior knowledge to remove statistical randomness and confounding factors from high-dimensional data for several classification and regression models [72–75]. The major advantage of these network-based models is the better generalization across independent studies since the network information is consistent with the conserved patterns in the gene expression data. For example, previous studies in [72, 74] discovered that more consistent signature genes of breast cancer metastasis can be identified from independent gene expression datasets by network-based classification models. The observations also motivated several graph algorithms for detecting cancer causal genes in protein-protein interaction network [76, 77].

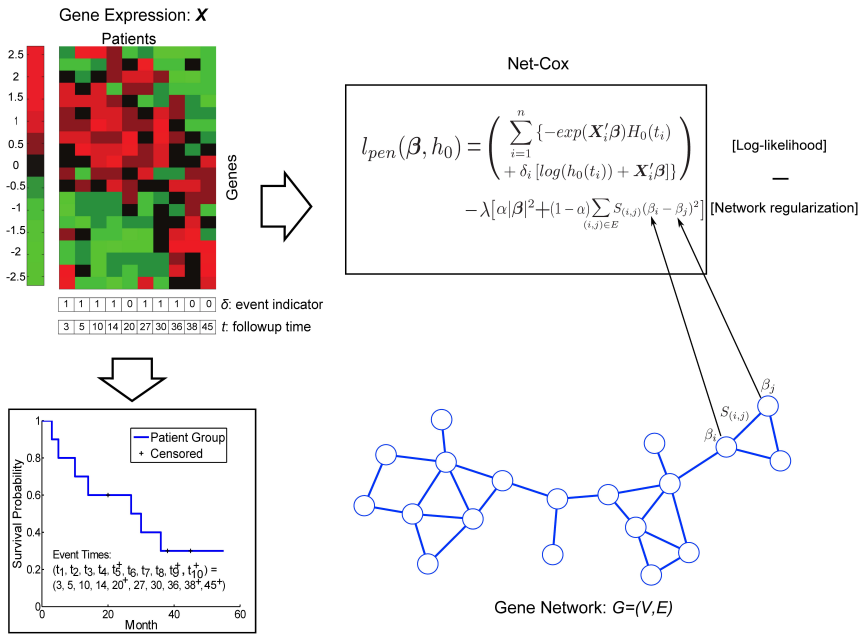

Figure 3.1: **Overview of Net-Cox.** The patient gene expression data X and the survival information specified by followup times t and event indicators δ are illustrated on the left. The cost function of Net-Cox given in the box combines the total likelihood of Cox regression with a network regularization. The gene network shown is used as a constraint to encourage smoothness among correlated genes, i.e. the coefficients of the genes connected with edges of large weights are similarly weighted.

In this chapter, we propose a network-based Cox proportional hazard model called

Net-Cox to explore the co-expression or functional relation among gene expression features for survival analysis. The relation between gene expressions are modeled by a gene relation network constructed by co-expression analysis or prior knowledge of gene functional relations. In the Net-Cox model, a graph Laplacian constraint is introduced as a smoothness requirement on the gene features linked in the gene relation network. Figure 3.1 illustrates the general framework of Net-Cox for utilizing gene network information in survival analysis. In the framework, the cost function of Net-Cox, shown in the box, combines the total likelihood of Cox regression with a network regularization. The total log-likelihood is a function of the linear regression coefficients $\boldsymbol{\beta}$ and the base hazard $h_0(t)$ on each followup time $\{t_1, t_2, ..., t_{10}\}$, represented by the likelihood ratios with the patient gene expression data and the survival information specified by followup times and event indicators. The gene network is either constructed with gene co-expression information or a given gene functional linkage network. The gene network is modeled as a constraint to encourage smoothness among correlated genes, for example gene i and j in the network, such that the coefficients of the genes connected with edges of large weights are similarly weighted. The cost function of Net-Cox can be solved by alternating optimization of $\boldsymbol{\beta}$ and $h_0(t)$ by iterations. An algorithm that solves the Net-Cox model in its dual representation is also introduced to improve the efficiency. The complete model is explained in detail in Section 3.3.

In this study, we applied Net-Cox to identify gene expression signatures associated with the outcomes of death and recurrence in the treatment of ovarian carcinoma. Ovarian cancer is the fifth-leading cause of cancer death in US women [59]. Identifying molecular signatures for patient survival or tumor recurrence can potentially improve diagnosis and prognosis of ovarian cancer. Net-Cox was applied on three large-scale ovarian cancer gene expression datasets [59, 78, 79] to predict survivals or recurrences and to identify the genes that may be relevant to the events. Our study is fundamentally different from previous survival analysis on ovarian cancer [59, 78–80], which are based on univariate Cox regression. For example, in [59], gene expression profiles from 215 stage II-IV ovarian tumors from TCGA were used to identify a prognostic gene signature (univariate Cox $p-$value < 0.01) for overall survival, including 108 genes correlated with poor (worse) prognosis and 85 genes correlated with good (better) prognosis. In [78], a Cox score is defined to measure the correlation between gene expression and survival.

The genes with a Cox score that exceeds an empirically optimized threshold in leave-one-out cross-validation were reported as signature genes. Similarly, in [79] and [80], a univariate Cox model was applied to identify association between gene expressions and survival (univariate Cox $p-$value < 0.01). Our study is based on gene networks enriched by co-expression and functional information and thus identifies subnetwork signatures for predicting survival or recurrence in ovarian cancer treatment.

3.2 Results

In the experiments, Net-Cox was applied to analyze three ovarian cancer gene expression datasets listed in Table 3.1. Net-Cox (equation (3.4)) was compared with L_2-Cox (equation (3.1)) and L_1-Cox (equation (3.2)) with performance evaluation in survival prediction and gene signature identification for the analysis of patient survival and tumor recurrence. First, for evaluation with a better focus on cancer-relevant genes, the expressions of a list of 2647 genes that are previously known to be related to cancer (Sloan-Kettering cancer genes) are used. On the data of these 2647 genes, Net-Cox, L_2-Cox and L_1-Cox were evaluated by consistency of signature gene selection across the three datasets, accuracy of survival prediction and assessment of statistical significance. Next, more comprehensive experiments on all 7562 mappable genes were conducted to identify novel signature genes associated with ovarian cancer. Finally, we further analyzed and validated ovarian cancer signatures by an additional tumor array experiment and literature survey. In all the experiments, gene co-expression networks and a gene functional linkage network were used to derive the network constraints for Net-Cox. The details of data preparation and the algorithms are described in Section 3.3.

	Dataset (GEO ID)	TCGA (N/A)	Tothill (GSE9899)	Bonome (GSE26712)
Death	**# of Censored**	227	160	24
	# of Uncensored	277	111	129
Recurrence	**# of Censored**	241	86	N/A
	# of Uncensored	263	185	N/A

Table 3.1: **Patient samples in the ovarian cancer datasets.** The number of patients categorized by censoring and uncensoring for the death and recurrent events is reported in each dataset. Note that the Bonome dataset does not provide information on recurrence.

3.2.1 Net-Cox identifies consistent signature genes across independent datasets

To evaluate the generalization of the models, we first measured the consistency among the signature genes selected from the three independent datasets by each method. Specifically, we report the percentage of common genes in the three rank lists identified by a method. This measurement assumes that even under the presence of biological variability in gene expressions and patient heterogeneities in each dataset, genes that are selected in multiple datasets are more likely to be true signature genes. Thus, higher consistency across the datasets might indicate higher quality in gene selection.

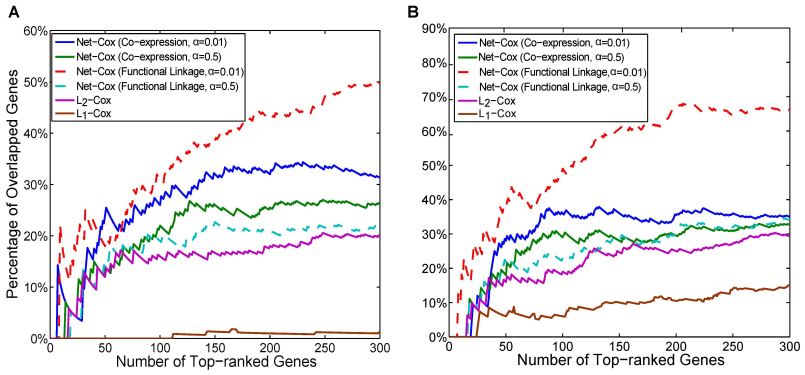

Figure 3.2: **Consistency of signature genes (Sloan-Kettering cancer genes).** The x-axis is the number of selected signature genes ranked by each method. The y-axis is the percentage of the overlapped genes between the selected genes across the ovarian cancer datasets. The plots show the results for the death outcome (A) and the tumor recurrence outcome (B).

In Figure 3.2, we plot the number of common genes among the first k (up to 300) genes in the gene ranking lists from all of the three datasets for the death event and two datasets (TCGA and Tothill) for the recurrence event. For the parameter setting of Net-Cox, we fixed λ to be the optimal parameter in the five-fold cross-validation (see Section **Materials and Methods** and report the results with $\alpha = 0.01$ and 0.5. Since the ranking lists of Net-Cox with $\alpha = 0.95$ are nearly identical to those of L_2-Cox, they are not reported for better clarity in the figure. The first observation is that the gene

rankings by Net-Cox are more consistent than those by L_2-Cox and L_1-Cox at all the cutoffs. Moreover, Net-Cox with $\alpha = 0.01$ identified more common signature genes than Net-Cox with $\alpha = 0.5$. For example, for the tumor recurrence outcome, Net-Cox (Co-expression) with $\alpha = 0.01$ and 0.5 identified 36 and 29 common genes among the first 100 genes in the gene ranking lists, Net-Cox (Functional linkage) with $\alpha = 0.01$ and 0.5 identified 49 and 23 common genes, and L_2-Cox and L_1-Cox only identified 19 and 6 common genes, respectively. In general, variable selection by L_1-Cox is not stable from high-dimensional gene expression data, and thus, the overlaps in the gene lists by L_1-Cox are significantly lower than the other methods. It is also interesting to see the gradient of the overlap ratio from $\alpha = 0.01$ to $\alpha = 0.5$, and then to $\alpha = 1$ (L_2-Cox), which indicates that, when a gene network plays more an important role in gene selection, the gene rankings tend to be more consistent. This observation is consistent with previous studies with protein-protein interaction network or gene co-expression network [72, 74, 75]. Note that since the overlaps are across three datasets for the death event and across two datasets for the recurrence event, the overlaps for the death event is expected to be lower than those for the recurrence event. Another important difference is that the same functional linkage network is always used while the co-expression network is dataset-specific. Thus, it is also expected that the overlaps by Net-Cox with the functional linkage network is higher than those by Net-Cox with the co-expression network. Together, the results demonstrate that Net-Cox effectively utilized the network information to improve gene selection and accordingly, the generalization of the model to independent data.

3.2.2 Net-Cox improves survival prediction across independent datasets

	Test Dataset	**Net-Cox (Co-exp)**	**Net-Cox (FL)**	L_2-Cox	L_1-Cox
Death	**Tothill**	1.1178E-06	2.5938E-07	2.9932E-06	0.0011
	Bonome	7.6088E-07	3.6039E-06	5.2590E-06	0.1165
Recurrence	**Tothill**	0.0567	0.0786	0.1115	0.4219

Table 3.2: **Log-rank test** $p-$values **in cross-dataset evaluation (Sloan-Kettering cancer genes).** The survival prediction performance on Tothill and Bonome datasets using the Cox models trained with TCGA dataset are reported.

Five-fold cross-validation was first conducted for parameter tuning for Net-Cox, L_2-Cox and L_1-Cox on each dataset. The optimal parameters of Net-Cox are reported

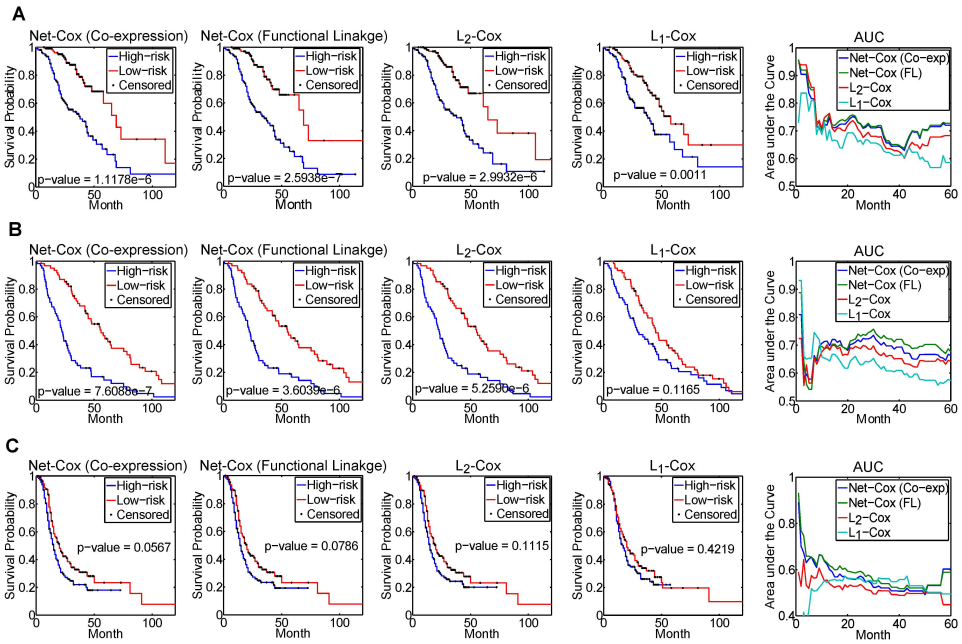

Figure 3.3: **Cross-dataset survival prediction (Sloan Kettering cancer genes).** The first four columns of plots show the Kaplan-Meier survival curves for the two risk groups defined by Net-Cox (co-expression network), Net-Cox (functional linkage network), L_2-Cox and L_1-Cox. The fifth column of plots compare the time-dependent area under the ROC acurves based on the estimated risk scores (PIs). The plots show the results for the death outcome by training with TCGA dataset and test on Tothill Dataset (A), the death outcome by training with TCGA dataset and test on Bonome Dataset (B), the tumor recurrence outcome by training with TCGA dataset and test on Tothill Dataset (C).

in Table S1 in [35]. To test how well the models generalize across the datasets, we trained Net-Cox model, L_2-Cox model, and L_1-Cox model with the TCGA dataset, and then predicted the survival of the patients in the other two datasets with the TCGA-trained models. In training, we used the optimal λ and α from the five-fold cross-validation to train the models with the whole TCGA dataset. The results are given in Table 3.2. In all the cases, Net-Cox obtained more significant $p-$values in the log-rank test than L_2-Cox and L_1-Cox. To further compare the results, we show the Kaplan-Meier survival curves and the ROC curves in Figure 3.3. The first four columns of plots in the figure show the Kaplan-Meier survival curves for the two risk groups defined by Net-Cox

with co-expression network and functional linkage network, L_2-Cox, and L_1-Cox. The fifth column of plots compare the time-dependent area under the ROC curves based on the estimated risk scores (PIs). In Figure 3.3, in many regions, Net-Cox achieved large improvement over both L_2-Cox and L_1-Cox while the improvement is less obvious in several other regions. Overall, Net-Cox achieved better or similar AUCs in all the time points in the three plots. To evaluate the statistical significance of the differences between the time-dependent AUCs generated by Net-Cox and the other two methods, in Table S2 in [35] we report $p-$values at each event time with the null hypothesis that the two time-dependent AUCs estimated by two models are equal. At many points of the event time, the time-dependent AUCs generated from Net-Cox are significant higher.

The cross-validation log-partial likelihood (CVPLs) for the combinations of (λ, α) in the five-fold cross-validation are also reported in Table S3 in [35]. In all the cases, the optimal CVPLs of Net-Cox are higher than those of L_2-Cox. L_1-Cox was fine-tuned with 1000 choices of parameters with a very small bin size. In one of the cases (TCGA: Recurrence), the optimal CVPL of L_1-Cox is higher but in the other cases, the optimal CVPLs of Net-Cox are higher. Interestingly, the optimal α is often 0.1 or 0.5, indicating the optimal CVPL is a balance of the information from gene expressions and the network. The observations prove that the network information is useful for improving survival analysis. The left column of Figure S1 in [35] shows the average time-dependent area under the ROC curves based on the estimated risk scores (PI) of the patients in the fifth fold of the five repeats, and Table S4A and S4B in [35] show log-rank $p-$values of the fifth fold of the five repeats. Net-Cox achieved the best overall survival prediction although the results are less obvious than those of the cross-dataset analysis.

3.2.3 Statistical assessment

To understand the role of the gene network on the consistency in gene selection and the contribution to the log-partial likelihood, we tested Net-Cox with randomized co-expression networks. In each randomization, the weighted edges between genes were shuffled. We report the mean and the standard deviation of the percentage of overlapping genes of 50 randomizations in Figure 3.4. Compared with the consistency plots with the true networks, the overlaps by Net-Cox on the randomized networks are much

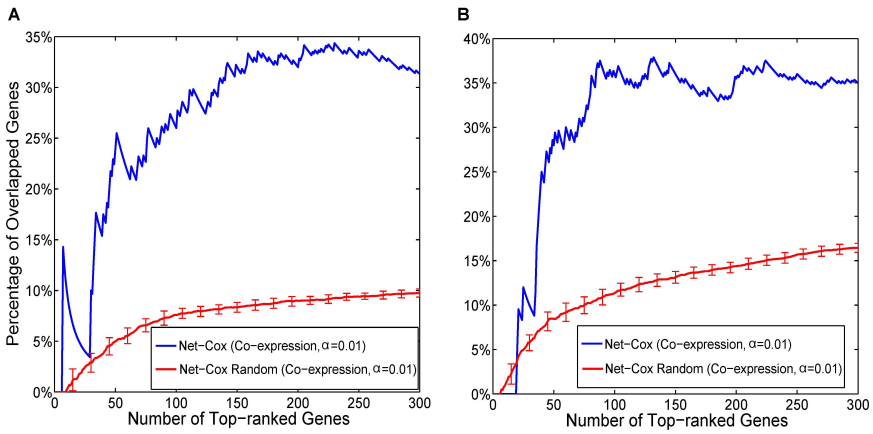

Figure 3.4: **Consistency of signature genes on randomized co-expression networks.** The x-axis is the number of selected signature genes ranked by each method. The y-axis is the percentage of the overlapped genes between the selected genes across the ovarian cancer datasets. The red curve reports the mean and the standard deviation of the percentages averaged over the experiments of 50 randomized networks. The plots show the results for the death outcome (A) and the tumor recurrence outcome (B).

lower. We also report the boxplot of the log-partial likelihood in the same 50 randomized co-expression network with $\alpha = 0.01$ in Figure 3.5. Compare with the log-partial likelihood with the real co-expression network, the range of the likelihood generated with the randomized networks is again lower by a large margin, which provides clear evidence that the co-expression network is informative for survival analysis.

To further understand the role of the network information in cross-validation, we fixed the optimal parameter λ and conducted the same five-fold cross-validation with randomized co-expression networks to compute the CVPL with different α in $\{0.01, 0.1, 0.5. 0.95\}$. We repeated the process on 20 random networks for each α. The boxplots of CVPLs with different αs are shown in Figure 3.6. In all measures, the CVPL with the true gene network is well above the mean of the 20 random cases. Another important observation is that, in both plots, when the randomized network information is more trusted with a smaller α, the variance of the CVPLs is also getting larger; and the case with $\alpha = 0.01$ gives the worst CVPL mean and the largest variance. The result indicates that the randomized networks did not provide any valuable information in

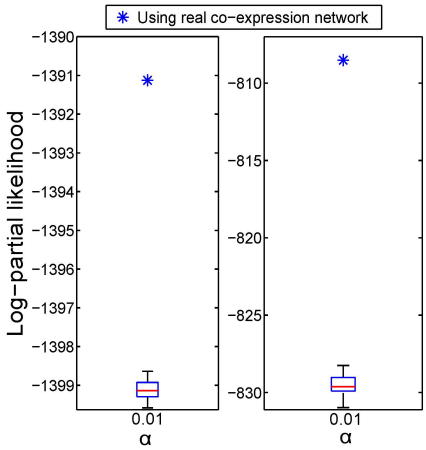

Figure 3.5: **Statistical analysis of log-partial likelihood.** The optimal λ was fixed and $\alpha = 0.01$ is set to allow better evaluation of the network information. The log-partial likelihood computed by Net-Cox on the real co-expression network and on the randomized co-expression network are reported against tumor recurrence in the TCGA and Tothill datasets. The stars represent the results with the real co-expression networks, and the boxplots represent the results with the randomized networks.

survival prediction. In contrast, with the true gene network, CVPLs generated from $\alpha = 0.01$ and $\alpha = 0.1$ are much higher than the ones from $\alpha = 0.95$ and L_2-Cox ($\alpha = 1$). Again, these results convincingly support the importance of using the network information in survival prediction.

3.2.4 Evaluation by whole gene expression data

Besides the 2647 Sloan-Kettering genes, all the 7562 mappable genes were also tested to evaluate Net-Cox, L_2-Cox and L_1-Cox by consistency of signature gene selection across the three datasets and accuracy of survival prediction in similar experiments. For the signature gene consistency, Figure S2 in [35] reports the percentage of common genes identified by each method in the ranking lists from the datasets. For the cross-dataset validation, Table S5 in [35] shows the log-rank test $p-$values by training the TCGA datasets and test on the other two datasets, and Figure S3 in [35] shows the Kaplan-Meier survival curves for the two risk groups defined by Net-Cox, L_2-Cox and L_1-Cox and compares the time-dependent area under the ROC curves. For the

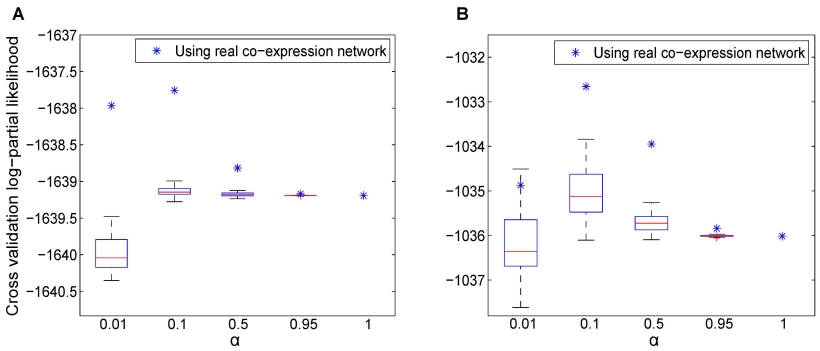

Figure 3.6: **Statistical analysis of cross-validation log-partial likelihood (CVPL).** The optimal λ was fixed and α is varied from 0.01 to 1. The CVPL of five-fold cross-validation on the real co-expression network and on the randomized co-expression network are reported against tumor recurrence in TCGA dataset (A) and Tothill dataset (B). The stars represent the results with the real co-expression networks, and the boxplots represent the results with the randomized networks.

five-fold cross-validation, the right column of Figure S1 in [35] shows the average time-dependent area under the ROC curves based on the estimated risk scores (PI) of the patients in the fifth fold of the five repeats, and Table S4C and S4D in [35] report log-rank test $p-$values of the fifth fold of the five repeats. Overall, similar observations are made in experimenting with all the genes, though the improvements are less significant compared with the results by experimenting with the Sloan-Kettering cancer genes. One possible explanation is that, since the genes in the Sloan-Kettering gene list are more cancer relevant, the gene expressions may be more readily integrated with the network information.

3.2.5 Signature genes are ECM components or modulators

To analyze the signature genes identified by Net-Cox and L_2-Cox, we created consensus rankings across the three datasets by re-ranking the genes with the lowest rank by Net-Cox and L_2-Cox in the three datasets. Specifically, for each gene, a new ranking score is assigned as the lowest of its ranks in the three datasets, and then, all the genes were re-ranked by the new ranking score. The top-15 genes selected by Net-Cox and L_2-Cox in the consensus rankings are shown in Table 3.3. For the death outcome, nine signature

Death			Recurrence		
Net-Cox (Co-exp)	**Net-Cox (FL)**	L_2-Cox	**Net-Cox (Co-exp)**	**Net-Cox (FL)**	L_2-Cox
FBN1	COL11A1	COL11A1	COL5A2	COL11A1	COL11A1
COL5A2	MFAP4	FABP4	COL1A1	COL10A1	NLRP2
VCAN	TIMP3	MFAP4	COL5A1	CRYAB	CRYAB
SPARC	MFAP5	COMP	THBS2	NPY	PTX3
AEBP1	COL5A2	BCHE	FAP	IGF1	COL10A1
AOC3	THBS2	FAP	COL3A1	COMP	CXCL12
COL3A1	FAP	COL5A2	COL11A1	KLK5	THBS2
THBS2	CXCL12	MFAP5	FBN1	THBS2	NPY
PLN	AEBP1	TIMP3	VCAN	PI3	KLK5
ADIPOQ	RYR3	THBS2	INHBA	CXCL12	COMP
COL5A1	LOX	HOXA5	CTSK	MFAP5	FAP
CNN1	COL5A1	NUAK1	COL1A2	VGLL1	MFAP5
COL6A2	EDNRA	COL5A1	SPARC	CCL11	PI3
COL1A2	NUAK1	SLIT2	AEBP1	EPHB1	PDGFD
DCN	LPL	CXCL12	SERPINE1	OXTR	CHRDL1

Table 3.3: **Top-15 signature genes.** The table lists the genes with over-expression indicating higher hazard of death or recurrence, identified by Net-Cox and L_2-Cox in the consensus ranking across the three datasets.

genes, FBN1, VCAN, SPARC, ADIPOQ, CNN1, DCN, LOX, EDNRA, LPL, known to be related to ovarian cancer [81–89] are only discovered by Net-Cox. Among the ten common genes highly ranked by both Net-Cox and L_2-Cox, three are collagen genes, and MFAP5, TIMP3, THBS2, and CXCL12 are previously known to be relevant to ovarian cancer [90–93]. For the recurrence outcome, there are eleven common signature genes detected by both Net-Cox and L_2-Cox. Net-Cox identified six additional ovarian cancer related signature genes [81–83, 94–96].

Gene Sym	Reference	Description
ADIPOQ	[84]	ADIPOQ 45T/G and 276G/T polymorphisms is associated with susceptibility to polycystic ovary syndrome(PCOS).
CCL11	[96]	CCL11 signaling plays an important role in proliferation and invasion of ovarian carcinoma cells.
CNN1	[85]	CCN1 plays a role in ovarian carcinogenesis by stimulating survival and antiapoptotic signaling pathways.
CRYAB	[97]	Low expression of lens crystallin CRYAB is significantly associated with adverse ovarian patient survival.
CXCL12	[93]	CXCL12 and vascular endothelial growth factor synergistically induce neoangiogenesis in human ovarian cancers.
DCN	[86]	Ovarian DCN is an ECM-associated component, which acts as a multifunctional regulator of GF signaling in the primate ovary.
EDNRA	[88]	Endothelin peptide is produced before ovulation and the contractile action of EDN2 within the ovary is facilitated via EDNRA.
FBN1	[81]	FBN1 controls the bioactivity of TGFβs and associate with polycystic ovary syndrome (PCOS).
IGF1	[95]	Ovarian follicular growth is controlled by the production of intraovarian growth regulatory factors such as IGF1.
INHBA	[94]	INHBA is the promoter of TAF4B; TAF4B in the ovary is essential for proper follicle development.
LOX	[87]	Inhibition of LOX expression portends worse clinical parameters for ovarian cancer.
LPL	[89]	LPL is differentially expressed between preoperative samples of ovarian cancer patients and those of healthy controls.
MFAP5	[90]	MAGP2 is an independent predictor of survival in advanced serous ovarian cancer.
NPY	[98]	NPY receptor is expressed in human primary ovarian neoplasms.
SPARC	[83]	SPARC expression in ovarian cancer cells is inversely correlated with the degree of malignancy.
THBS2	[92]	In ovarian cancer an aberrant methylation process is responsible for down-regulation of THBS2.
TIMP3	[91]	TIMP2 and TIMP3 play functional role in LPA-induced invasion as negative regulators.
VCAN	[82]	VCAN V1 isoform is overexpressed in ovarian cancer stroma compared with normal ovarian stroma and ovarian cancer cells.

Table 3.4: **Literature review of the candidate ovarian cancer genes.** This table reports the citations that describe relevance of the signature genes with over-expression indicating higher hazard of death or recurrence, identified by Net-Cox across the three datasets.

The intersection of the 60 genes identified by Net-Cox in Table 3.3 contains 41

unique genes. We performed a literature survey of the 41 genes, out of which eighteen are supported by literature to be related to ovarian cancer shown in Table 3.4. Most of the genes whose over-expression is associated with poor outcome are stromal or extracellular-related proteins. The genes such as VCAN, TIMP3, THBS2, ADIPOQ, PARC, NPY, MFAP5, DCN, LOX, FBN1, EDNRA, and CXCL12 are either components or modulators of extracellular matrix. In particular, LOX protein is involved in extracellular matrix remodeling by cross-linking collagens. Extracellular matrix remodeling through over-expression of collagens has been shown to contribute to platinum resistance, and platinum resistance is the main factor in chemotherapy failure and poor survival of ovarian cancer patients. Therefore, the identification of these extracellular matrix proteins as biomarkers of early recurrence and poor survival outcome in patients with ovarian cancer is consistent with the suggested pathobiological role of some of these proteins in platinum resistance.

3.2.6 Enriched PPI subnetworks and GO terms

The top-100 signature genes with the largest regression coefficients by Net-Cox and L_2-Cox learned from the TCGA dataset were mapped to the human protein-protein interaction (PPI) network obtained from HPRD [10] and also analyzed with DAVID functional annotation tool [51]. We report the densely connected PPI subnetworks constructed from the 100 genes selected by Net-Cox in Figure 3.7. Compared with the PPI subnetworks generated from the 100 genes selected by L_2-Cox, which contain 10 genes in the death subnetwork and 6 genes in the recurrence subnetworks (shown in Figure S4 in [35]), the subnetworks are both larger and denser. The subnetworks identified from the co-expression networks in Figure 3.7(A) are also larger than the subnetworks identified by the functional linkage network in Figure 3.7(B) although many genes are shared. In the recurrence subnetworks, DCN, THBS1, and THBS2 are members of the TGF$-\beta$ signaling KEGG pathway, and FBN1 controls the bioactivity of TGFβs and relates to polycystic ovary syndrome [81]. In addition, ten genes are members of the focal adhesion KEGG pathway. These results point to a possibility that extracellular matrix signaling through focal adhesion complexes may constitute a pathway by which tumor cells escape chemotherapy and produce recurrence in chemotherapy [99]. Nine genes in the death subnetworks are members of the extracellular matrix(ECM)-receptor

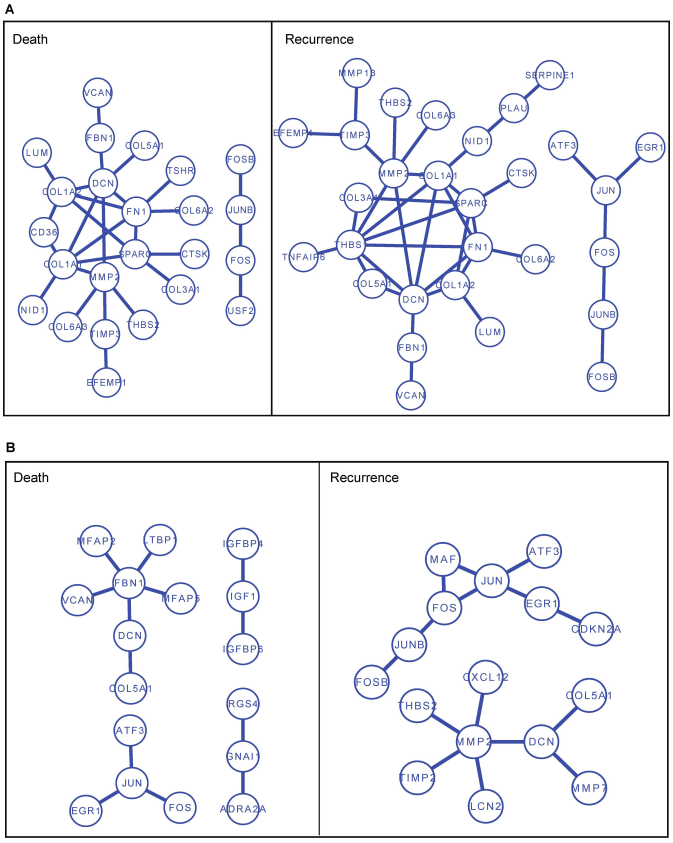

Figure 3.7: **Protein-Protein interaction subnetworks of signature genes identified by Net-Cox on the TCGA dataset.** (A) The PPI subnetworks identified by Net-Cox on the co-expression network. (B) The PPI subnetworks identified by Net-Cox on the functional linkage network.

interaction KEGG pathway, and eighteen genes are annotated as ECM component. It was shown that ECM acts as a model substratum for the preferential attachment of human ovarian tumor cells in vitro [100]. FOS and JUN constitutes a nuclear signaling components downstream of extracellular signal-regulated kinases (ERK1/2) that are mediators of growth factor and adhesion-related signaling pathways [101]. In addition, the genes are also enriched by regulation of gene expression, positive regulation of cellular process, developmental process, transcription regulator activity, and growth factor binding, all of which are well-known cancer relevant functions. The significantly enriched GO functions are listed in Table S6 and Table S7 in [35]. Extracellular matrix,

extracellular region, and extracellular structure organization are consistently the most significantly enriched in the analysis.

3.2.7 Laboratory experiment validates FBN1's role in chemo-resistance

FBN1 was ranked 1st and 8th by Net-Cox with co-expression network in death and recurrence outcomes while L_2-Cox only ranked FBN1 at 27th and 42nd, respectively. It is interesting to note that in the PPI subnetworks in Figure 3.7(A), FBN1 is connected with VCAN and DCN, both of which bear the annotation of extracellular matrix. The dense subnetwork boosted the ranking of FBN1 when Net-Cox was applied. We further validated the role of FBN1 in ovarian cancer recurrence using tumor microarrays (TMAs) consisting of a cohort of 78 independent patients (see Section **Materials and Methods**). The expression level of FBN1 in ovarian cancer was scored by one observer who is blinded to the clinical outcome and described as: absent (0), moderate (1), and high (2) as illustrated by Figure 3.8.

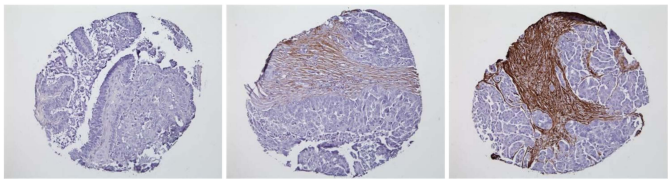

Figure 3.8: **Representative photomicrographs showing various levels of FBN1 expression in ovarian tumor arrays.** The brown regions are stromal area showing expression of FBN1.

In Figure S5A in [35], the Kaplan-Meier survival curve shows the recurrence for groups by the FBN1 staining scores. At the initial 12 month, there is no difference in the recurrence rate between the groups with high and low FBN1 staining. After 12 month, the recurrence rate is lower in the low staining group. The similar patterns are also observed in the re-examination of the gene expression datasets in Figure S5B-E in [35]. Except the TCGA dataset on the Affymetrix platform (Figure S5E in [35]), the pattern is clearly observed on the other two platforms, exon arrays and Agilent arrays. The discrepancy in the Affymetrix data could be related to data pre-processing or experimental noise. The plots suggest that FBN1 plays a role on platinum-sensitive

ovarian cancer, and it could be developed as a target for platinum-sensitive patients with high FBN1 expression after about 12 month of the treatment.

In the context of ovarian cancer treatment, a platinum-sensitive patient group can be defined as the group of patients who was free of recurrence or developed a recurrence after k month of the treatment, where $k \geq 14$ depends on the treatment plan and the follow-up. To better evaluate the role of FBN1, we plot the Kaplan-Meier survival curve only for the platinum-sensitive patients in Figure 3.9, i.e. we removed all the patients who developed recurrence before k month and considered the follow-ups up to 72 month after the treatment. Due to the small sample size of the Mayo Clinic data, we set $k = 14$ while $k = 20$ for the gene expression datasets. In Figure 3.9A, the difference between the survival curves of low FBN1 staining and high staining patient groups is more significant. Similarly, Figure 3.9B-E show the survival curves for the platinum-sensitive patients for groups by the expression value of FBN1 in gene expression datasets. Compare to the matched curves in Figure S5 in [35], the log-rank test $p-$values are more significant except the TCGA dataset on the Affymetrix platform. Overall, the observations strongly support the hypothesized role of FBN1 in platinum-sensitive ovarian cancer patients.

3.3 Materials and Methods

3.3.1 Gene relation network construction

We denote gene relation network by $\boldsymbol{G} = (\boldsymbol{V}, \boldsymbol{W})$, where $\boldsymbol{V}$ is the vertex set, each element of which represents a gene, and $\boldsymbol{W}$ is a $|\boldsymbol{V}| \times |\boldsymbol{V}|$ positively weighted adjacency matrix. $\boldsymbol{D}$ is a diagonal matrix with $D_{ii} = \sum_j W_{ij}$ and $\boldsymbol{S} = \boldsymbol{D}^{-\frac{1}{2}}\boldsymbol{W}\boldsymbol{D}^{-\frac{1}{2}}$ is the normalized weighted adjacency matrix by dividing the square root of the column sum and the row sum. Two gene relation networks were used with Net-Cox, the gene co-expression network and the gene functional linkage network.

Gene co-expression network: A gene co-expression network was generated from a gene correlation graph model. In the weighted adjacency matrix $\boldsymbol{W}$, each W_{ij} is the reliability score [102] based on the absolute value of the Pearson's correlation coefficients between genes v_i and v_j, calculated as $W_{ij} = \frac{1}{R_{i,j} \times R_{j,i}}$, where $R_{i,j}$ is gene v_i's rank among all the genes with respect to the correlation with gene v_j and $R_{j,i}$ is gene v_j's rank with

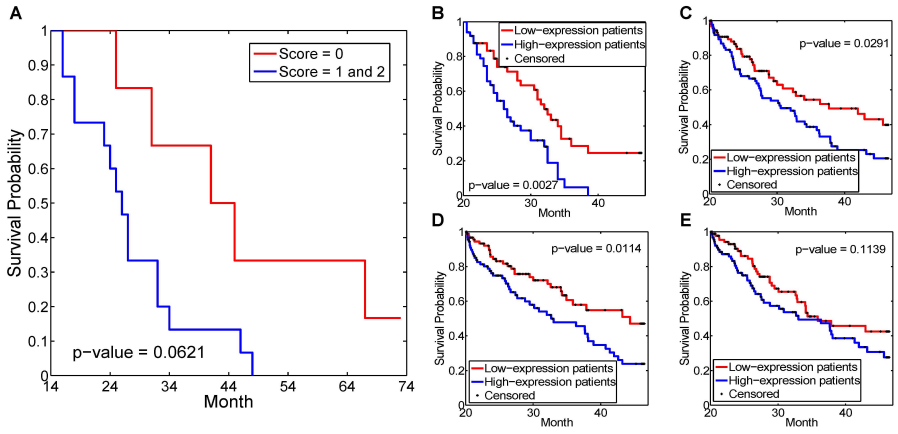

Figure 3.9: **Kaplan-Meier survival plots on FBN1 expression groups.** (A) Kaplan-Meier survival curve of recurrence between 14 to 72 month by FBN1 staining groups on Mayo Clinic dataset. (B) Kaplan-Meier survival curve of recurrence between 20 to 72 month by the expression of FBN1 on Tothill dataset. (C)-(E) Kaplan-Meier survival curves of recurrence between 20 to 72 month by the expression of FBN1 on TCGA dataset with AgilentG4502A platform, HuEx-1_0-st-v2 platform, and Affymetrix HG-U133A platform, respectively. In plot(A), the groups with FBN1 staining score 1 and 2 are combined into the high-expression group. In plots(B)-(E), the patients are divided into two groups of the same size by the expression of FBN1.

respect to the correlation with gene v_i. Note that the gene co-expression network is directly inferred from the gene expression dataset. Thus, a gene co-expression network is specific to the dataset used for computing the co-expression network.

Gene functional linkage network: A human gene functional linkage network was constructed by a regularized Bayesian integration system [103]. The network contains maps of functional activity and interaction networks in over 200 areas of human cellular biology with information from 30,000 genome-scale experiments. The functional linkage network summarizes information from a variety of biologically informative perspectives: prediction of protein function and functional modules, cross-talk among biological processes, and association of novel genes and pathways with known genetic disorders [103]. Each edge in the network is weighted between [0,1] to quantify the functional relation between two genes. Thus, the functional linkage network provides much more comprehensive information than Human protein-protein interaction network, which was more frequently used as the network prior knowledge.

3.3.2 Gene expression dataset preparation

Three independent microarray gene expression datasets for studying ovarian carcinoma were used in the experiments [59, 78, 79]. The information of patient samples in each dataset is given in Table 3.1. All the three datasets were generated by the Affymetrix HG-U133A platform. The raw .CEL files of two datasets were downloaded from GEO website (Tothill: GSE9899) and (Bonome: GSE26712) [78, 79]. The TCGA dataset was downloaded from The Cancer Genome Atlas data portal [59]. The raw files were normalized by RMA [48]. After merging probes by gene symbols and removing probes with no gene symbol, a total of 7562 unique genes were derived from the 22,283 probes and overlapped with the functional linkage network for this study. Note that the Bonome dataset does not provide information on recurrence. Thus, only TCGA and Tothill datasets were used for studying recurrence while all the three datasets were used for studying death. In cross-dataset validation, the batch effects among the three datasets were removed by applying ComBat [104]. Besides testing all the genes, for a better focus on genes that are more likely to be cancer relevant, we derived a set of 2647 genes from the cancer gene list compiled by Sloan-Kettering Cancer Center (SKCC) [105].

The TCGA datasets with AgilentG4502A platform (gene expression array) and HuEx-1_0-st-v2 (exon expression array) were used to evaluate the signature gene FBN1 in Figure 3.9. The processed level 3 data with expression calls for gene/exon were downloaded from the TCGA data portal.

3.3.3 Cox proportional hazard model

In the analysis of microarray gene expressions, the number of gene features p is larger than the number of subjects n by several magnitudes ($p \gg n$). Fitting the Cox regression model proposed in section 1.2.2 will lead to large regression coefficients, which are not reliable. One possible solution is to introduce a L_2-norm constraint to shrink regression coefficients estimates towards zero [62, 65]. In the L_2-Cox model, the regression coefficients are estimated by maximizing the penalized total log-likelihood:

$$l_{pen}(\boldsymbol{\beta}, h_0) = \sum_{i=1}^{n} \left\{ -exp(\boldsymbol{X}_i'\boldsymbol{\beta}) H_0(t_i) + \delta_i \left[log(h_0(t_i)) + \boldsymbol{X}_i'\boldsymbol{\beta} \right] \right\} - \frac{1}{2}\lambda \sum_{j=1}^{p} {\beta_j}^2, \quad (3.1)$$

where $\lambda\sum_{j=1}^{p}{\beta_j}^2$ is the penalty term and λ is the parameter controlling the amount of shrinkage. Another possibility is to introduce a L_1-norm constraint for variable selection [26, 66]. The L_1-Cox model penalizes the log-partial likelihood (equation (1.3)) by $\lambda\sum_{j=1}^{p}|\beta_j|$ leading to:

$$pl_{pen}(\boldsymbol{\beta}) = \sum_{i=1}^{n}\delta_i\left\{\boldsymbol{X}_i'\boldsymbol{\beta} - log\left[\sum_{j\in R(t_i)} exp(\boldsymbol{X}_j'\boldsymbol{\beta})\right]\right\} - \lambda\sum_{j=1}^{p}|\beta_j|. \tag{3.2}$$

In our experiments, R package "glmnet" [106] was used in the implementation of L_1-Cox.

3.3.4 Network-constrained Cox regression (Net-Cox)

We introduce a network-constraint to the Cox model as follows,

$$l_{pen}(\boldsymbol{\beta}, h_0) = l(\boldsymbol{\beta}, h_0) - \frac{1}{2}\lambda\boldsymbol{\beta}'[(1-\alpha)\boldsymbol{L} + \alpha\boldsymbol{I}]\boldsymbol{\beta}, \tag{3.3}$$

where $\boldsymbol{L}$ is a positive semidefinite matrix derived from network information, $\boldsymbol{I}$ is an identity matrix, and λ is the parameter controlling the weighting between the total likelihood and the network constraint. $\alpha \in (0, 1]$ is another parameter weighting the network matrix and the identity matrix in the network constraint. For convenience, we define $\boldsymbol{\Gamma} = (1-\alpha)\boldsymbol{L} + \alpha\boldsymbol{I}$ and rewrite the object function as

$$l_{pen}(\boldsymbol{\beta}, h_0) \;=\; \sum_{i=1}^{n}\left\{-exp(\boldsymbol{X}_i'\boldsymbol{\beta})H_0(t_i) + \delta_i\left[log(h_0(t_i)) + \boldsymbol{X}_i'\boldsymbol{\beta}\right]\right\} - \frac{1}{2}\lambda\boldsymbol{\beta}'\boldsymbol{\Gamma}\boldsymbol{\beta}. \tag{3.4}$$

The term $\lambda\boldsymbol{\beta}'[(1-\alpha)\boldsymbol{L} + \alpha\boldsymbol{I}]\boldsymbol{\beta}$ in equation (3.3) is a network Laplacian constraint to encode prior knowledge from a network. Given a normalized graph weight matrix $\boldsymbol{S}$, we assume that co-expressed (related) genes should be assigned similar coefficients by defining the following cost term over the coefficients,

$$\begin{aligned}\Psi(\boldsymbol{\beta}) &= \frac{1}{2}\sum_{i,j=1}^{p} S_{i,j}(\beta_i - \beta_j)^2 \\ &= \boldsymbol{\beta}'(\boldsymbol{I} - \boldsymbol{S})\boldsymbol{\beta} = \boldsymbol{\beta}'\boldsymbol{L}\boldsymbol{\beta}.\end{aligned} \tag{3.5}$$

As illustrated in Figure 3.1, the Laplacian constraint encourages a smoothness among the regression coefficients in the network. Specifically, for any pair of genes connected

by an edge, there is a cost proportional to both the difference in the coefficients and the edge weight. Large difference between coefficients on two genes connected with a highly weighted edge will result in a large cost in the objective function. Thus, the objective function encourages assigning similar weights to genes connected by edges of larger weights. By adding an additional L_2-norm constraint to $\Psi(\boldsymbol{\beta})$ weighted by α, we obtain the network constraint $(1-\alpha)\boldsymbol{\beta'L\beta}+\alpha|\boldsymbol{\beta}|^2=\boldsymbol{\beta'\Gamma\beta}$ in equation (3.3) and (3.4). The L_2-norm of $\boldsymbol{\beta}$ similarly regularizes the uncertainty in the network constraint, which could have a singular Hessian matrix, and the α parameter balances between the L_2-norm and the "Laplacian-norm". The smaller the α parameter, the more importance put on the network information.

3.3.5 Alternating optimization algorithm

The objective function defined by equation (3.4) can be solved by alternating optimization of $\boldsymbol{\beta}$ and $h_0(t)$. The maximization with respect to $\boldsymbol{\beta}$ is done by Newton-Raphson method. The derivative of equation (3.4) is

$$\begin{aligned}\frac{\partial l_{pen}(\boldsymbol{\beta},h_0)}{\partial\boldsymbol{\beta}} &= \sum_{i=1}^{n}\left[\delta_i - exp(\boldsymbol{X}_i'\boldsymbol{\beta})H_0(t_i)\right]\boldsymbol{X}_i - \lambda\boldsymbol{\Gamma\beta} \\ &= \boldsymbol{X'\Delta} - \lambda\boldsymbol{\Gamma\beta}, \end{aligned} \tag{3.6}$$

where $\Delta_i = \delta_i - exp(\boldsymbol{X}_i'\boldsymbol{\beta})H_0(t_i)$, and the second derivative is

$$\begin{aligned}\frac{\partial^2 l_{pen}(\boldsymbol{\beta},h_0)}{\partial\boldsymbol{\beta}\partial\boldsymbol{\beta}'} &= -\left[\sum_{i=1}^{n} exp(\boldsymbol{X}_i'\boldsymbol{\beta})H_0(t_i)\boldsymbol{X}_i\boldsymbol{X}_i'\right] - \lambda\boldsymbol{\Gamma} \\ &= -\boldsymbol{X'DX} - \lambda\boldsymbol{\Gamma}, \end{aligned} \tag{3.7}$$

where $\boldsymbol{D}$ is the diagonal matrix with $D_{ii} = exp(\boldsymbol{X}_i'\boldsymbol{\beta})H_0(t_i)$. Thus, the full algorithm to solve the Net-Cox model is given below.

1 **Initialization:** $\boldsymbol{\beta = 0}$; Compute $\boldsymbol{L = I - S}$.

2 **Do** until convergence

(a) **Do** Newton-Raphson iteration

i. Compute the first derivative $l'_{pen}(\boldsymbol{\beta}, h_0) = \frac{\partial l_{pen}(\boldsymbol{\beta}, h_0)}{\partial \boldsymbol{\beta}}$

ii. Compute the second derivative $l''_{pen}(\boldsymbol{\beta}, h_0) = \frac{\partial^2 l_{pen}(\boldsymbol{\beta}, h_0)}{\partial \boldsymbol{\beta} \partial \boldsymbol{\beta}'}$

iii. Update $\boldsymbol{\beta} = \boldsymbol{\beta} - \{l''_{pen}(\boldsymbol{\beta}, h_0)\}^{-1} l'_{pen}(\boldsymbol{\beta}, h_0)$

(b) Update $\hat{h}_0(t_i) = 1/\sum_{j \in R(t_i)} exp(\boldsymbol{X}'_j \hat{\boldsymbol{\beta}})$

3 **Return** $\boldsymbol{\beta}$

Using Newton-Raphson method to update $\boldsymbol{\beta}$ requires inverting the Hessian matrix, which is time consuming and often inaccurate. An alternative approach is to reduce the covariant space from p to n, which relates to singular value decomposition that exploits the low rank of the gene expression matrix $\boldsymbol{X}$ [65]. The equation

$$\begin{aligned} \frac{\partial l_{pen}(\boldsymbol{\beta}, h_0)}{\partial \boldsymbol{\beta}} &= \sum_{i=1}^{n} \left[\delta_i - exp(\boldsymbol{X}'_i \boldsymbol{\beta}) H_0(t_i)\right] \boldsymbol{X}_i - \lambda \boldsymbol{\Gamma} \boldsymbol{\beta} \\ &= \boldsymbol{X'\Delta} - \lambda \boldsymbol{\Gamma} \boldsymbol{\beta} = \boldsymbol{0} \end{aligned} \tag{3.8}$$

implies that $\boldsymbol{\beta} = \boldsymbol{\Gamma}^{-1} \boldsymbol{X}' \boldsymbol{\eta}$ for some $\boldsymbol{\eta}$. Thus, the dual form of equation (3.4) with respect to $\boldsymbol{\eta}$ is

$$l_{pen}(\boldsymbol{\eta}, h_0) = \sum_{i=1}^{n} \left\{-exp(\boldsymbol{Z}'_i \boldsymbol{\eta}) H_0(t_i) + \delta_i \left[log(h_0(t_i)) + \boldsymbol{Z}'_i \boldsymbol{\eta}\right]\right\} - \frac{1}{2} \lambda \boldsymbol{\eta' Z \eta} \tag{3.9}$$

with $\boldsymbol{Z}_i = \boldsymbol{X \Gamma^{-1} X}_i$ and $\boldsymbol{Z} = \boldsymbol{X \Gamma^{-1} X'}$. In its dual form, it is clear that the new object function (3.9) is equivalent to equation (3.4) but the problem dimension is reduced from p to n.

3.3.6 Cross validation and parameter tuning

To determine the optimal tuning parameters λ and α, we performed five-fold cross-validation following the procedure proposed by [65] on each of the three datasets. In the cross-validation, four folds of data are used to build a model for validation on the

fifth fold, cycling through each of the five folds in turn, and then the (λ, α) pair that maximizes the cross-validation log-partial likelihood (CVPL) are chosen as the optimal parameters. CVPL is defined as

$$CVPL(\lambda, \alpha) = \sum_{i=1}^{5} \left[pl(\hat{\boldsymbol{\beta}}^{(-i)}_{(\lambda,\alpha)}) - pl^{(-i)}(\hat{\boldsymbol{\beta}}^{(-i)}_{(\lambda,\alpha)}) \right] \tag{3.10}$$

where $\hat{\boldsymbol{\beta}}^{(-i)}$ is the optimal $\boldsymbol{\beta}$ learned from the data without the ith fold. In the equation, $pl()$ denotes the log-partial likelihood on all the samples and $pl^{(-i)}()$ denotes the log-partial likelihood on samples excluding the ith fold. We performed a grid search for the optimal (λ, α) maximizing the sum of the contributions of each fold to the log-partial likelihood in CVPL. In particular, λ was chosen from {1e-5, 1e-4, 1e-3, 1e-2, 1e-1, 1} (λs larger than 1 do not change the ranking of $\boldsymbol{\beta}$ anymore), and α was chosen from $\{0.01, 0.1, 0.5, 0.95\}$. Note that, when $\alpha = 1$, Net-Cox ignores the network information and is reduced to L_2-Cox. For L_1-Cox, the optimal λ was chosen from 1000 λs by the "glmnet" parameter setting with the largest CVPL.

3.3.7 Evaluation measures

The Log-rank test [107] and time-dependent ROC [108] were used to evaluate measurements of the prediction performance by a survival model. For the gene expression profile X in the test set, the prognostic indexes $PI = \boldsymbol{X'}\hat{\boldsymbol{\beta}}$ is computed, where $\hat{\boldsymbol{\beta}}$ is the regression coefficients of the survival model, to rank the patients by descending order. We assigned the top 40% of the patients as the *high-risk* group and the bottom 40% as the *low-risk* group.

The Log-rank test is a statistical hypothesis test for comparison of two Kaplan-Meier survival curves with the null hypothesis that there is no difference between the population survival curves, i.e. the probability of an event occurring at any time point is the same for each population. The test statistic is compared with a χ^2 distribution with one degree of freedom to derive the significance $p-$value reflecting the difference between two survival curves. The log-rank test only evaluates whether the patients are assigned to the "right group" but not how well the patients are ranked within the group by examining the PI. A more refined approach is afforded by the time-dependent ROC curves [108,109]. Time-dependent ROC curves evaluate how well the PI classifies

the patients into *high-risk* and *low-risk* prognosis groups. Letting $f(\boldsymbol{X})=\boldsymbol{X'}\hat{\boldsymbol{\beta}}$, we can define time-dependent sensitivity and specificity functions at a cutoff point c as

$$sensitivity[c,t|f(\boldsymbol{X})] = Pr\left\{f(\boldsymbol{X}) > c|\delta(t)=1\right\},$$
$$specificity[c,t|f(\boldsymbol{X})] = Pr\left\{f(\boldsymbol{X}) \leq c|\delta(t)=0\right\}$$

with $\delta(t)$ being the event indicator at time t [109]. The corresponding ROC curve for any time t, $ROC[t|f(\boldsymbol{X})]$, is the plot of $sensitivity[c,t|f(\boldsymbol{X})]$ versus $1-specificity[c,t|f(\boldsymbol{X})]$ with different cutoff point c. $AUC[t|f(\boldsymbol{X})]$ is denoted as the area under the $ROC[t|f(\boldsymbol{X})]$ curve. A larger $AUC[t|f(\boldsymbol{X})]$ indicates better prediction of time to event at time t, as measured by sensitivity and specificity evaluated at time t. We plot the AUCs at each time t to compare the methods.

To select gene variables in the multi-variate scenario by Net-Cox and L_2-Cox, we ranked the genes by the magnitude of the coefficients $\boldsymbol{\beta}$. To justify this simple ranking method, we examined the relation between the magnitude of the coefficients for each gene and the contribution of the gene to the log-partial likelihood in Figure S6 in [35]. It is clear in the plot that the genes towards the two tails of the ranking list contributes most of the likelihood, and the proportion of the contributions are consistent with the ranking. For L_1-Cox, we ranked the genes by the first-time jump into the active set when decreasing the tuning parameter λ in the solution path.

3.3.8 Tumor array preparation

With approval by the Mayo Clinic Institutional Review Board, archived ovarian epithelial tumor specimens from patients with advanced-stage, high-grade serous, or endometrioid tumors obtained prior to exposure to any chemotherapy were utilized to construct the TMA array. The array was constructed using a custom-fabricated device that utilizes a 0.6-mm tissue corer and a 240-capacity recipient block. Triplicate cores from each tumor were included, as were cores of liver as fiducial markers and controls for immunohistochemistry reactions. Five-micrometer-thick sections were cut from the TMA blocks. Immunohistochemistry was performed essentially as described in [110]. Sections of tissue arrays were deparaffinized, rehydrated, and submitted to antigen retrieval by a steamer for 25 minutes in target retrieval solution (Dako, Carpinteria, CA, USA). Endogenous peroxide was diminished with 3% H_2O_2 for 30 min. Slides were

blocked in protein block solution for 30 min and then blocked with avidin and biotin for 10 min each, followed by overnight incubation with 1:1000 diluted Anti-FBN1 antibody (HPA021057, Sigma-Aldrich) at 4°C. The sections were then incubated with biotinylated universal link for 15 min and streptavidin for 25 min at 25°C. Slides were developed in diaminobenzine and counterstained with hematoxylin.

3.4 Discussion

Many methods were proposed for survival analysis on high-dimensional gene expression data with highly correlated variates [60, 61]. In this study, we propose Net-Cox, a network-based survival model, which to our knowledge is among the first models that directly incorporate network information in survival analysis. The graph Laplacian constraint introduced in Net-Cox is positive definite and thus, the Net-Cox model can be solved as efficiently as solving the L_2-Cox model. In the dual form of Net-Cox, the model is scalable to genomic data with $p \gg n$. Net-Cox not only makes survival predictions but also generate densely connected subnetworks enriched by genes with large regression coefficients.

Net-Cox is most related to the L_p shrinkage-based Cox models typically with L_1 (Lasso) and L_2 (ridge) penalties [61]. The purpose of applying L_1 regularization is to obtain a sparse estimate of the linear coefficients for solving the high-dimensionality problem. A Ridge penalty results in small regression coefficients to avoid overfitting problem with the small sample size. Compared with Net-Cox, neither Lasso nor ridge regularized Cox regression models are designed to incorporate any prior information among genes in the objective function for survival analysis. Another alternative solution in the literature is to apply dimension reduction methods to obtain a small number of features for subsequent survival analysis such as principal components analysis (PCA) [111–113] and partial least squares (PLS) [114–117]. These methods first compute the principle components to capture the maximal covariance with the outcomes or the maximal variance in the gene expression data, and then project the original high-dimensional gene expressions into a space of the directions of the principle components. Typically, these methods do not utilize any prior information. It is also usually difficult

to interpret the results since the features in the project space are not directly mappable to any particular gene expression. There are also tree-based ensemble methods for survival analysis such as bagging of survival trees and random forests [118,119]. The tree-based methods usually also require a variable selection step to reduce the dimensionality. Multiple trees are then built from different samplings of training data and the results of the individual trees are aggregated for making predictions. Since the trees are built from random sampling, the resulted forests consist of different trees. Thus, the interpretation of the trees can be very difficult [60].

In [120], a supervised group Lasso approach (SGLasso) is proposed to account for the cluster structure in gene expression data as prior information in survival analysis. In this approach, gene clusters are first identified with clustering. Important genes are then identified with Lasso model within each cluster and finally, the clusters are selected with group Lasso. More recently, the method in [121] combined a group Lasso constraint with Lasso Cox regression (sparse-group Lasso). An additional parameter is introduced to balance between Lasso and group Lasso constraints. There are two major discrepancies between Net-Cox and the graph Lasso methods. First, while group Lasso assumes non-overlapping cluster structures among gene expressions, the gene network introduced in Net-Cox captures more global relation among all the genes. Specifically, beyond the cluster partition of genes into co-expression groups, a gene network represents pairwise relationships between genes, which contain information of modularities, subgraph structures and other global properties such as centralities and closenesses. Second, while SGLasso adopts an unsupervised strategy to cluster genes as predefined groups for selection, Net-Cox identifies subnetwork signatures in a supervised manner, in which the selected subnetworks are enriched by genes with large regression coefficients by the design of the network constraint. In Table S3(g) in [35], we reported the results of group Lasso and sparse-group Lasso in the five-fold cross-validation with the R package "SGL" [121]. Compared with the CVPLs by the other methods in Table S3(a)-(f), the CVPLs in Table S3(g) in [35] for group Lasso and sparse-group Lasso are consistently lowest when 25 or 100 gene clusters are used as groups. Thus, we did not further compare and analyze other results by the group Lasso models.

The experiments in this study clearly demonstrated that the network information is

useful for improving the accuracy of survival prediction as well as increasing the consistency in discovering signature genes across independent datasets. Since the signature genes were discovered based on their relation in the networks, they enrich dense PPI subnetworks, which are useful for pathway analysis. It is also interesting to note that the PPI subnetworks of signature genes identified by Net-Cox on the TCGA dataset is enriched by extracellular matrix proteins such as collagens, fibronectin, and decorin. Previous gene expression studies had identified stromal gene signatures in ovarian tumors to be associated with poor survival outcome [78]. Therefore, our observation that the stromal subnetwork enriched by extracellular matrix proteins and stromal-related proteins is consistent with the role of stromal gene signature in poor prognosis. Finally, collagen matrix remodelling has been linked to platinum resistance, and ovarian cancer cells grown on collagens are more resistant to platinum agents than their counterpart grown on non-collagen substratum [122]. The tumor array validation indicates that FBN1 can serve as a biomarker for predicting recurrence of platinum-sensitive ovarian cancer.

Chapter 4

Network-based Isoform Quantification with RNA-Seq Data for Cancer Transcriptome Analysis

4.1 Introduction

Application of next generation sequencing technologies to mRNA sequencing (RNA-Seq) is a widely used approach in transcriptome study [123–125]. Compared with microarray technologies, RNA-Seq provides information for expression analysis at transcript level and avoids the limitations of cross-hybridization and restricted range of the measured expression levels. Thus, RNA-Seq is particularly useful for quantification of isoform transcript expressions and identification of novel isoforms. Accurate RNA-Seq-based transcript quantification is a crucial step in other downstream transcriptome analyses such as isoform function prediction in the pioneer work in [126], and differential gene expression analysis [127] or transcript expression analysis [25]. Detecting biomarkers from transcript quantifications by RNA-Seq is also a frequent common practice in biomedical research. However, transcript quantification is challenging since a variety

of systematical sampling biases have been observed in RNA-Seq data as a result of library preparation protocols [21, 28, 128, 129]. Moreover, in the aligned RNA-Seq short reads, most reads mapped to a gene are potentially originated by more than one transcript. The ambiguous mapping could result in hardly identifiable patterns of transcript variants [28, 29].

A useful prior knowledge that has been largely ignored in RNA-Seq transcriptome quantification is the relation among the isoform transcripts by the interactions between their protein products. The protein products of different isoforms coded by the same gene may contain different domains interacting with the protein products of the transcripts in other genes. Previous studies suggested that alternative splicing events tend to insert or delete complete protein domains/functional motifs [130] to mediate key linkages in protein interaction networks by removal of protein domain-domain interactions [131]. The work in [126, 132] also suggested unique patterns in isoform co-expressions. Thus, the abundance of an isoform transcript in a gene can significantly impact the quantification of the transcripts in other genes when their protein products interact with each other to accomplish a common function as illustrated by a real subnetwork in Figure 4.1, which is constructed based on domain-domain interaction databases [133,134] and Pfam [135]. Motivated by our observation that the protein products of highly co-expressed transcripts are more likely to interact with each other by protein domain-domain binding in four TCGA RNA-Seq datasets (see the section **Results**), we constructed two human transcript interaction networks of different sizes based on protein domain-domain interactions to improve transcript quantification. Based on the constructed transcript network, we propose a network-based transcript quantification model called Net-RSTQ to explore domain-domain interaction information for estimating transcript abundance. In the Net-RSTQ model, Dirichlet prior representing prior information in the transcript interaction network is introduced into the likelihood function of observing the short read alignments. The new likelihood function of Net-RSTQ can be alternating-optimized over each gene with expectation maximization (EM). It is important to note that the Dirichlet prior from the neighboring isoforms play two possible roles. On one hand, for the isoforms in the same gene but with different interacting partners, the different prior information will help differentiate their expressions to reflect their different functional roles. On the other hand, for the isoforms in the same gene with the same

interacting partners, the uniform prior assumes no difference in their functional roles and thus, promotes a smoother expression patterns across the isoforms. In both cases, the Dirichlet prior captures the functional variations/similarities across the isoforms in each gene as prior information for estimation of their abundance.

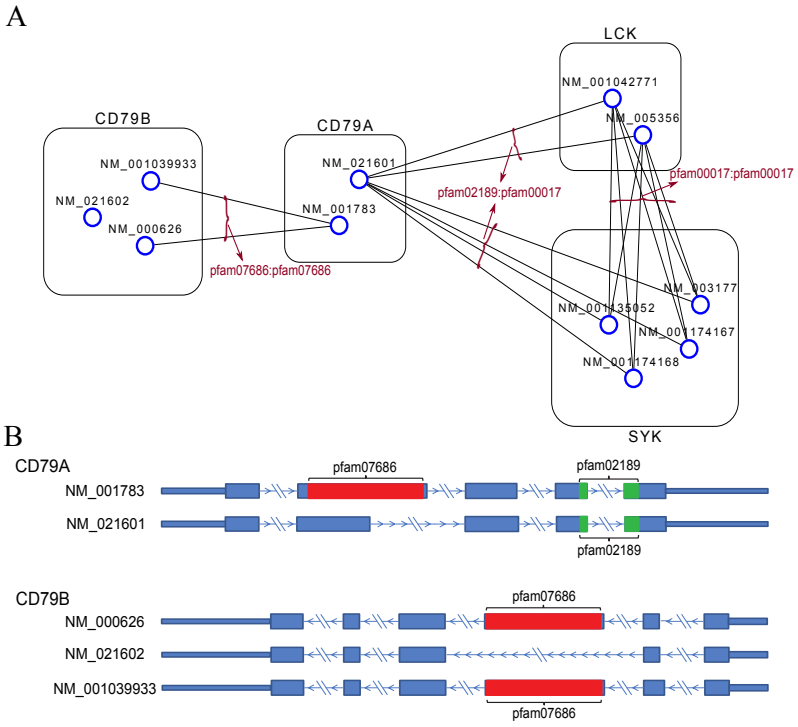

Figure 4.1: **An isoform transcript network based on protein domain-domain interactions.** (A) The subnetwork shows the domain-domain interactions among transcripts from four human genes, CD79B, CD79A, LCK and SYK. In the network, the nodes represent isoform transcripts, which are further grouped and annotated by their gene name; and the edges represent domain-domain interactions between two transcripts. Each edge is also annotated by the interacting domains in the two transcripts. (B) RefSeq transcript annotations of CD79A and CD79B are shown with Pfam domain marked in color. The Pfam domains were detected with Pfam-Scan software. Note that no interaction is included between transcripts NM_001039933 and NM_000626 of gene CD79B without assuming self-interactions for modeling simplicity. For better visualization, only the interactions coincide with PPI are shown in the figure.

The chapter is organized as following. In the section **Materials and Methods**, we describe the procedure to construct protein domain-domain interaction networks, the mathematic description of the probabilistic model and the Net-RSTQ algorithm, qRT-PCR experiment design, and RNA-Seq data preparation. In the section **Results**, we first demonstrate the correlation between protein domain-domain interactions and isoform transcript co-expressions across samples in four cancer RNA-Seq datasets from The Cancer Genome Atlas (TCGA) to justify using domain-domain interactions as prior knowledge. We then compared the predicted isoform proportions with qRT-PCR experiments on 25 multi-isoform genes in three cell lines, H9 stem cell line, OVCAR8 ovarian cancer cell line and MCF7 breast cancer cell line. Net-RSTQ was also applied to four cancer RNA-Seq datasets to quantify isoform expressions to classify patient samples by the survival or relapse outcomes. In addition, simulations were also performed to measure the statistical robustness of Net-RSTQ over randomized networks.

4.2 Materials and Methods

In this section, we first describe the construction of the transcript interaction network. We then introduce the network-based transcript quantification model (Net-RSTQ) by applying the protein domain-domain interaction information as prior knowledge based on the base EM model mentioned in section 1.2.3. The notations used in the equations are summarized in Table 4.1. At last, qRT-PCR experiment design and RNA-Seq data preparation are explained.

Notation	Description
N	total # of genes
$\boldsymbol{T}$	set of transcripts; T_{ik} is the k^{th} transcript of the i^{th} gene; $\boldsymbol{T}_i$ denotes the transcripts of the i^{th} gene
l_{ik}	length of transcript T_{ik}
$\boldsymbol{r}$	set of reads; r_{ij} is the j^{th} read aligned to the i^{th} gene; $\boldsymbol{r}_i$ is the read set aligned to the i^{th} gene
p_{ik}	the probability of a read generated by transcript T_{ik} in the i^{th} gene
$\boldsymbol{P}_i$	the probability of a read generated by transcript $\boldsymbol{T}_i$ in the i^{th} gene, specifically, $[p_{i1}, ..., p_{i,\lvert\boldsymbol{T}_i\rvert}]$
$\boldsymbol{P}$	concatenate of all $\boldsymbol{P}_i$, specifically, $[\boldsymbol{P}_1, \boldsymbol{P}_2, ..., \boldsymbol{P}_N]$
ρ_{ik}	relative abundance of the transcript T_{ik} in the i^{th} gene
$\boldsymbol{\pi}$	transcript expression; π_{ik} is the expression of the k^{th} transcript of the i^{th} gene
ϕ_{ik}	average expressions (normalized) of transcript T_{ik}'s neighbors in the transcript network
$\boldsymbol{\alpha}$	parameters of Dirichlet distribution; $\alpha_{ik} = \lambda\phi_{ik} + 1$ is the parameter of the Dirichlet distribution of p_{ik}
q_{ijk}	read sampling probability, $q_{ijk} = \frac{1}{l_{ik} - l_r + 1}$ if read r_{ij} is aligned to transcript T_{ik}, otherwise $q_{ijk} = 0$
$\boldsymbol{S}$	binary matrix for transcript interaction network

Table 4.1: **Notations.**

4.2.1 Transcript network construction

Two binary transcript networks were constructed by measuring the protein domain-domain interactions (DDI) between the domains in each pair of transcripts in four steps. First, the translated transcript sequences of all human genes were obtained from RefSeq [136]. Second, Pfam-Scan was used to search Pfam databases for the matched Pfam domains on each transcript with 1e-5 e-value cutoff [135]. Note that only high quality, manually curated Pfam-A entries in the database were used in the search. Third, domain-domain interactions were obtained from several domain-domain interaction databases, and if any domain-domain interaction exists between a pair of transcripts, the two transcripts are connected in the transcript network. Specifically, 6634 interactions between 4346 Pfam domain families from two 3D structure-based DDI datasets (iPfam [133] and 3did [134]) inferred from the protein structures in Protein Data Bank (PDB) [137] were used in the experiments. Besides these highly confident structure-based DDIs, transcript interactions constructed from 2989 predicted high-confidence DDIs and 2537 predicted medium-confidence DDIs in DOMINE [138] were also included if the transcript interaction agrees with protein-protein interactions (PPI) in HPRD [139].

In the experiments, we focused on the transcripts from two cancer gene lists from the literature for better reliability in annotations. The first smaller transcript network consists of 11736 interactions constructed from the 3D structure-based DDIs and 421 interactions constructed from the predicted DDIs among the 898 transcripts in 397 genes from the first gene list [140]. The second larger transcript network contains 711,516 interactions constructed from the 3D structure-based DDIs among 5599 transcripts in 2551 genes in a larger gene list [141]. Since inclusion of the predicted DDIs results in a much higher density in the large network, the large network does not include predicted DDIs to prevent too many potential false positive interactions. The characteristics of the two transcript networks are summarized in Table 4.2. The density of the two networks are 3.02% and 4.54% respectively, which are in similar scale with the PPI network. Both networks show high clustering coefficients, suggesting modularity of subnetworks. Note that self-interactions (interactions between transcript(s) in the same gene) are not considered since Net-RSTQ only utilizes positive correlation between the expressions of neighboring transcripts in different genes. For simplicity, Net-RSTQ assumes that

self-interactions will not change the transcript quantification of an individual gene in the model.

	# of Gene	# of Transcripts	# of Interactions	Density	Diameter	Avg. # of Neighbors	Avg. Cluster Coefficients
Small Network	397	898	12157	3.02%	9	27.08	0.3578
Large Network	2551	5599	711516	4.54%	9	254.16	0.5255

Table 4.2: **Network characteristics.**

In Figure 4.1(A) a subnetwork of the transcripts in gene CD79A and CD79B with their direct neighbors in the small transcript network is shown. The RefSeq transcript annotations of CD79A and CD79B are shown in Figure 4.1(B). In CD79A transcript NM_001783 contains an extra domain pfam07686 while transcript NM_021601 only contains a shorter hit pfam02189. Note pfam02189 also has the same hit in NM_001783 with an e-value larger than 1e-5. In CD79B transcripts NM_001039933 and NM_000626 contain a domain pfam07686, which is removed in alternative splicing of NM_021602. In the transcript subnetwork shown in Figure 4.1(A), the transcripts in CD79A or CD79B have different interaction partners in the network. In the transcripts in CD79A, the expression of NM_021601 will correlate with the transcripts in LCK and SYK, and NM_001783 will correlate with two transcripts in CD79B. The isoform transcripts in LCK and SYK show no different DDIs suggesting there is no functional variation by protein bindings and more similar expression patterns are potentially expected as prior knowledge.

4.2.2 Network-based transcript quantification model

In the Net-RSTQ model, the transcript interaction network $\boldsymbol{S}$ based on protein domain-domain interactions is introduced to calculate a prior distribution for estimating $\boldsymbol{P}$ jointly across all the genes and all the transcripts. The model assumes that the prior distribution of $\boldsymbol{P}_i$ is a Dirichlet distribution specified by parameters $\boldsymbol{\alpha}_i$ and each α_{ik} is proportional to the read count by average expression of the transcript T_{ik}'s neighbors in the transcript network $\boldsymbol{S}$. The prior read count ϕ_{ik} is defined as follows,

$$\phi_{ik} = l_{ik}(\boldsymbol{\pi}' \frac{\boldsymbol{S}_{*,(i,k)}}{\sum(\boldsymbol{S}_{*,(i,k)})}), \tag{4.1}$$

where $\boldsymbol{S}_{*,(i,k)}$ is a binary vector represents the neighborhood of transcript T_{ik} in transcript network $\boldsymbol{S}$ and $\sum(\boldsymbol{S}_{*,(i,k)})$ is the size of the neighborhood. The calculation of

each ϕ_{ik} is illustrated in Figure 4.2. The Dirichlet parameter $\boldsymbol{\alpha}_i$ is defined as a function of ϕ_{ik} as

$$\alpha_{ik} = \lambda\phi_{ik} + 1, \tag{4.2}$$

where $\lambda > 0$ is a tuning parameter balancing the belief between the prior-read count and the aligned-read count.

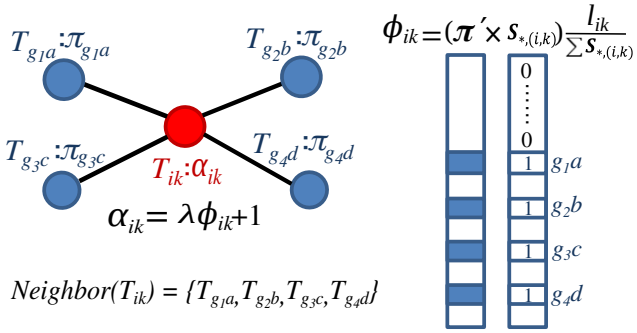

Figure 4.2: **Transcript interaction neighborhood.** In this toy example, transcript T_{ik} has four neighbor transcripts $\{T_{g_1a}, T_{g_2b}, T_{g_3c}, T_{g_4d}\}$, which are transcripts from g_1, g_2, g_3 and g_4, respectively. The neighborhood expression ϕ_{ik} of T_{ik} is then calculated as the average of its neighbor transcripts' expressions and further normalized by transcript length, represented as the vector product between $\boldsymbol{\pi}$ and $\boldsymbol{S}_{*,(ik)}$ normalized by the number of neighbors $\sum \boldsymbol{S}_{*,(ik)}$ and the transcript length l_{ik} in the figure.

To obtain the optimal $\boldsymbol{P}$ jointly for all genes, we introduce a pseudo-likelihood model to estimate $\boldsymbol{P}$ iteratively in each iteration. Assuming uniform $Pr(\boldsymbol{r}_i)$, the pseudo-likelihood function is defined as,

$$\mathcal{L}(\boldsymbol{P}, \boldsymbol{\alpha}; \boldsymbol{r}) = \prod_{i=1}^{N} \mathcal{L}(\boldsymbol{P}_i, \boldsymbol{\alpha}_i; \boldsymbol{r}_i) = \prod_{i=1}^{N} \frac{Pr(\boldsymbol{P}_i|\boldsymbol{\alpha}_i)Pr(\boldsymbol{r}_i|\boldsymbol{P}_i)}{Pr(\boldsymbol{r}_i)} \propto \prod_{i=1}^{N} Pr(\boldsymbol{P}_i|\boldsymbol{\alpha}_i)Pr(\boldsymbol{r}_i|\boldsymbol{P}_i). \tag{4.3}$$

Note that the pseudo-likelihood model relies on the independence assumption among the likelihood functions of each individual gene when the $\boldsymbol{\alpha}$ parameters of the Dirichlet priors are pre-computed. Thus, the model simply takes the product of the likelihood function from each gene. Each prior distribution $Pr(\boldsymbol{P}_i|\boldsymbol{\alpha}_i)$ follows the Dirichlet distribution,

$$Pr(\boldsymbol{P}_i|\boldsymbol{\alpha}_i) = C(\boldsymbol{\alpha}_i)\prod_{k=1}^{|\boldsymbol{T}_i|} {p_{ik}}^{\alpha_{ik}-1}, \text{where } C(\boldsymbol{\alpha}_i) = \frac{\Gamma(\sum_k \alpha_{ik})}{\prod_k \Gamma(\alpha_{ik})}. \tag{4.4}$$

Integrating equations (1.7) and (4.4), the pseudo-likelihood function in equation (4.3) can be rewritten with Dirichlet prior as

$$\begin{aligned}
\mathcal{L}(\boldsymbol{P};\boldsymbol{r}) &= \prod_{i=1}^{N}\left[C(\boldsymbol{\alpha}_i)\prod_{k=1}^{|\boldsymbol{T}_i|}{p_{ik}}^{\alpha_{ik}-1}\right]\left[\prod_{j=1}^{|\boldsymbol{r}_i|}\sum_{k=1}^{|\boldsymbol{T}_i|} p_{ik}q_{ijk}\right] \\
&= \prod_{i=1}^{N}\left[C(\lambda\boldsymbol{\phi}_i+1)\prod_{k=1}^{|\boldsymbol{T}_i|}{p_{ik}}^{\lambda\phi_{ik}}\right]\left[\prod_{j=1}^{|\boldsymbol{r}_i|}\sum_{k=1}^{|\boldsymbol{T}_i|} p_{ik}q_{ijk}\right].
\end{aligned} \tag{4.5}$$

In the pseudo-likelihood function in equation (4.5), the only hyper-parameter λ balances the proportion between the Dirichlet priors and the observed read counts of each transcript. The larger the λ, the more belief put on the priors.

4.2.3 The Net-RSTQ algorithm

The Net-RSTQ algorithm optimizes equation (4.5) by dividing the optimization into sub-optimization problems of sequentially estimating each $\boldsymbol{P}_i$. Specifically, we fix all $\boldsymbol{P}_c$, $c \neq i$, and thus $\boldsymbol{\phi}_i$ when estimating $\boldsymbol{P}_i$ with EM in each iteration and repeat the process multiple rounds throughout all the genes. In each step, the neighborhood expression $\boldsymbol{\phi}$ is recomputed with new $\boldsymbol{P}_i$ for computing the quantification of the next gene. For each sub-optimization problem, we estimate $\boldsymbol{P}_i$ with a fixed $\boldsymbol{\phi}$, the part of the likelihood function in equation (4.5) involved with the current variables $\boldsymbol{P}_i$ is

$$\bar{\mathcal{L}}(\boldsymbol{P}_i;\boldsymbol{r}_i) = \left[\prod_{g\in\boldsymbol{nb}(i)} C(\lambda\boldsymbol{\phi}_g+1)\prod_{k=1}^{|\boldsymbol{T}_g|}{p_{gk}}^{\lambda\phi_{gk}}\right]\left[C(\lambda\boldsymbol{\phi}_i+1)\prod_{k=1}^{|\boldsymbol{T}_i|}{p_{ik}}^{\lambda\phi_{ik}}\right]\left[\prod_{j=1}^{|\boldsymbol{r}_i|}\sum_{k=1}^{|\boldsymbol{T}_i|} p_{ik}q_{ijk}\right], \tag{4.6}$$

where $\boldsymbol{nb}(i)$ is the set of the genes containing transcripts that are neighbors of the transcripts in gene i in the transcript network. Equation (4.6) consists of three terms separated by the braces. The second and the third terms are the Dirichlet prior and the likelihood of the observed counts in the data for gene i. The first term is the Dirichlet priors of the neighbor transcripts of each T_{ik}. These prior probabilities are involved since $\boldsymbol{\phi}_g$ are functions of the current variable $\boldsymbol{P}_i$ (equations (1.9), (4.1) and (4.2)). Equation (4.6) cannot be easily solved with standard techniques. We adopt a heuristic approach

to only take steps that will increase the whole pseudo-likelihood function in equation (4.5). The Net-RSTQ algorithm is outlined below

Algorithm 1 NET-RSTQ

1: **Initialization**: random initialization or base EM (equation (1.7)) estimation of $\boldsymbol{P}^{(0)}$
2: **for** round $t = 1, \ldots$ **do**
3: $\quad \boldsymbol{P}^{(t)} = \boldsymbol{P}^{(t-1)}$
4: $\quad$ **for** gene $i = 1, \ldots, N$ **do**
5: $\quad\quad$ compute $\boldsymbol{\phi}_i$ based on $\boldsymbol{P}^{(t)}$ with equations (1.9) and (4.1)
6: $\quad\quad$ estimate $\boldsymbol{P}_i$ with EM algorithm (see next section)
7: $\quad\quad$ **if** $\bar{\mathcal{L}}(\boldsymbol{P}_i) > \bar{\mathcal{L}}(\boldsymbol{P}_i^{(t)})$ **then**
8: $\quad\quad\quad \boldsymbol{P}_i{}^{(t)} = \boldsymbol{P}_i$
9: $\quad\quad$ **end if**
10: $\quad$ **end for**
11: $\quad$ **if** $max(abs(\boldsymbol{P}^{(t)} - \boldsymbol{P}^{(t-1)}))$ <1e-6 **then**
12: $\quad\quad$ **break**
13: $\quad$ **end if**
14: **end for**
15: **return** $\boldsymbol{P}$

In the algorithm, the outer for-loop between line 2-14 performs multiple passes of updating $\boldsymbol{P}$. The inner for-loop between line 4-10 scans through each gene to update each $\boldsymbol{P}_i$. Line 7 checks the the difference in the likelihood $\bar{\mathcal{L}}$ of gene i before and after the estimated $\boldsymbol{P}_i$ is applied. The newly estimated $\boldsymbol{P}_i$ is kept in line 8 only if the likelihood $\bar{\mathcal{L}}$ in equation (4.6) is higher. The convergence of $\boldsymbol{P}$ is checked at line 11. In each sub-optimization problem, EM algorithm (described in the next section) is applied to estimate $\boldsymbol{P}_i$. After convergence, the transcripts expression $\boldsymbol{\pi}$ can be learned by equation (1.9) with the optimal $\boldsymbol{P}$.

4.2.4 EM algorithm in Net-RSTQ

In line 6 of Algorithm 1, we maximize the likelihood function of the sub-optimization problem in equation (4.6) to learn $\boldsymbol{P}_i$ given $\boldsymbol{\phi}_i$ as

$$\mathcal{L}(\boldsymbol{P}_i; \boldsymbol{r}_i) = \left[C(\lambda\boldsymbol{\phi}_i + 1) \prod_{k=1}^{|\boldsymbol{T}_i|} p_{ik}{}^{\lambda\phi_{ik}} \right] \left[\prod_{j=1}^{|\boldsymbol{r}_i|} \sum_{k=1}^{|\boldsymbol{T}_i|} p_{ik} q_{ijk} \right]. \tag{4.7}$$

Note that equation (4.7) is the part of equation (4.6) without the Dirichlet priors of the neighboring genes. In line 7 of Algorithm 1, the ignored Dirichlet priors are combined with the likelihood in equation (4.7), when $\bar{\mathcal{L}}(\boldsymbol{P_i})$ is computed, to evaluate the whole likelihood in equation (4.6). The likelihood function in equation (4.7) is defined on a categorical variable with Dirichlet prior, which can be solved with EM algorithm. Following EM formulation in [20], the expectation a_{ijk}, a soft assignment of read j to transcript k in gene i, is first estimated in the expectation step and $\boldsymbol{P}_i$ is then learned in the maximization step. When $\boldsymbol{\phi}_i$ is given, by taking log of equation (4.7) we can write the EM steps to find $\boldsymbol{P}_i$ below.

E step:

Letting ***Match*** signify a matching between reads and transcripts, and *Match(j)* be the transcript from which read j originates, we get:

$$\log[\mathcal{L}(\boldsymbol{P}_i; \boldsymbol{r}_i, \boldsymbol{Match})] = \log C(\lambda\boldsymbol{\phi}_i + 1) + \sum_{k=1}^{|\boldsymbol{T}_i|} \lambda\phi_{ik} \log(p_{ik}) + \sum_{j=1}^{|\boldsymbol{r}_i|} \log(p_{iMatch(j)} q_{ijMatch(j)}), \quad (4.8)$$

which leads to

$$\begin{aligned} \mathcal{Q}(\boldsymbol{P}_i|\boldsymbol{P}_i^{(it)}) &= E_{\boldsymbol{Match}|\boldsymbol{r}_i, \boldsymbol{P}_i^{(it)}}[\log(\mathcal{L}(\boldsymbol{P}_i; \boldsymbol{r}_i))] \\ &= \log C(\lambda\boldsymbol{\phi}_i + 1) + \sum_{k=1}^{|\boldsymbol{T}_i|} \lambda\phi_{ik} \log(p_{ik}^{(it)}) + \sum_{j=1}^{|\boldsymbol{r}_i|} \sum_{k=1}^{|\boldsymbol{T}_i|} (\log p_{ik}^{(it)} + \log q_{ijk}) * \frac{p_{ik}^{(it)} q_{ijk}}{\sum_{k=1}^{|\boldsymbol{T}_i|} p_{ik}^{(it)} q_{ijk}} \\ &= \log C(\lambda\boldsymbol{\phi}_i + 1) + \sum_{k=1}^{|\boldsymbol{T}_i|} \lambda\phi_{ik} \log(p_{ik}^{(it)}) + \sum_{j=1}^{|\boldsymbol{r}_i|} \sum_{k=1}^{|\boldsymbol{T}_i|} a_{ijk} \log(p_{ik}^{(it)}) + \sum_{j=1}^{|\boldsymbol{r}_i|} \sum_{k=1}^{|\boldsymbol{T}_i|} a_{ijk} \log(q_{ijk}) \end{aligned} \quad (4.9)$$

where it is the it^{th} iteration in EM and

$$a_{ijk} = \frac{p_{ik}^{(it)} q_{ijk}}{\sum_{k=1}^{|\boldsymbol{T}_i|} p_{ik}^{(it)} q_{ijk}}. \quad (4.10)$$

M step:

Given that q_{ijk} and $\boldsymbol{\phi}_i$ are known, the above reduces to maximizing

$$\boldsymbol{P}_i^{(it+1)} = \arg\max_{\boldsymbol{P}_i} \left[\sum_{k=1}^{|\boldsymbol{T}_i|} \lambda\phi_{ik} log(p_{ik}) + \sum_{j=1}^{|\boldsymbol{r}_i|} \sum_{k=1}^{|\boldsymbol{T}_i|} a_{ijk} log(p_{ik}) \right]. \quad (4.11)$$

Using Lagrange multipliers and differentiating, equation (4.11) is maximized when

$$p_{ik}^{(it+1)} = \frac{\lambda\phi_{ik} + \sum_{j=1}^{|\boldsymbol{r}_i|} a_{ijk}}{\sum_{k=1}^{|\boldsymbol{T}_i|} (\lambda\phi_{ik} + \sum_{j=1}^{|\boldsymbol{r}_i|} a_{ijk})}. \quad (4.12)$$

After EM algorithm converges, we update $\boldsymbol{P}$ with the newly estimated $\boldsymbol{P}_i$ only if the update leads to increase of equation (4.6). It can be seen from equation (4.12) that the role of λ is a parameter controlling the balance between the prior-read count and the aligned-read count. To see that, recall ϕ_{ik} is the prior-read count of transcript T_{ik} by the average expression of its neighbors (equation (4.1)) and $\sum_{j=1}^{|\boldsymbol{r}_i|} a_{ijk}$ is the expected aligned-read count of transcript T_{ik}. λ directly balances the contributions from the two terms. Therefore, a reasonable choice of λ should apply to RNA-Seq data with similar level of noise or bias in general.

4.2.5 qRT-PCR experiment design

Three qRT-PCR experiments are designed to measure the isoform proportions of 25 multi-isoform genes in three cell lines, H9 stem cell line, OVCAR8 ovarian cancer cell line and MCF7 breast cancer cell line. The cell lines were selected based on the available of both RNA-Seq data and cell culture in our labs. The qRT-PCR experiments focused on the gene with most different quantification results reported by Net-RSTQ and other compared methods. Due to the limitations in time and cost of running qRT-PCR experiments, only the 25 genes in the three cell lines were tested with all the results reported in the experiments. Quantitation of the real-time PCR results was done on the data from H9 human embryonic stem cells to obtain the absolute expressions for comparing more than two transcripts and comparative Ct method was done on the data from OVCAR8 ovarian cancer cells and MCF7 breast cancer cells to obtain the ratio between a pair of transcripts.

H9 Stem cell line

Total RNA was extracted from human embryonic stem (ES) H9 cells by using TRIzol (Invitrogen). To repeat the experiments of triplicate three times, 5μg RNA was used to synthesize complementary DNA with ReverTra Ace (Toyobo) and oligo-dT (Takara) according to the manufacturer's instructions. Transcript levels of genes were determined by using Premix Ex Taq (Takara) and analysed with a CFX-96 Real Time system (Bio-Rad). The templates for different transcripts were generated with PCR by using the template primers in S1 Table in [36]. After isolation and purification, the templates were used to generate the standard curves with qRT-PCR by using the qRT-PCR primers for

different transcripts. The generated standard curves have coefficient of determination (R2) over 0.999. The qRT-PCR primers were then applied to determine the expression levels of different transcripts in H9 ES cells by calculating with the standard curves. The expressions were carried out in three independent replications and the standard deviations were provided after the average.

Ovarian cancer cell line

1μg of total RNAs were isolated from untreated OVCAR8 cells using Trizol (Invitrogen). RNA was reverse-transcribed using Superscript II reverse transcriptase (Invitrogen) according to manufacture protocol. Real-time PCR was performed on CFX384 Real-time system (Bio-Rad) with FastStart SYBR Green Master (Roche) with the primer sets in S2 Table in [36]. PCR conditions are 10 min at 95°C and 40 cycles of 95°C for 45 sec and 60°C for 45 sec. Quantitation of the real-time PCR results was done using comparative Ct method. Two replicates of qRT-PCR were performed using total RNAs isolated.

Breast cancer cell line

0.5μg of total RNAs purified from MCF7 cells was used for oligo d$(T)_{20}$-primed reverse transcription (Superscript III; Life Technologies). SYBR Green was used to detect and quantitate PCR products in real-time reactions with the primer sets in S3 Table in [36]. PCR conditions for qRT-PCR analysis are 2 min 94°C and 40 cycles of 94°C for 30 sec, 60°C for 20 sec and 72°C for 30 sec. Quantitation of the real-time PCR results was done using comparative Ct method. GAPDH mRNA was used as a normalization control for quantitation. Three replicates of qRT-PCR were performed using total RNAs isolated.

4.2.6 RNA-Seq data preparation

Three cell line RNA-Seq datasets were used for evaluating the accuracy of transcript quantification by comparison with qRT-PCR results. The first dataset is the H9 embryonic stem cell line data from [142]. The raw RNA-Seq fastq file were downloaded from SRA website (SRR1015682) under GEO accession GSE51607. The second dataset

is an in-house dataset from the ovarian cancer cell line OVCAR8 prepared at University of Kansas Medical Center. The third dataset is the MCF7 breast cancer cell line data from [143]. The raw RNA-Seq fastq file was downloaded from SRA website (SRR925723) under GEO accession GSE48213. There are 23,397,325 single-end 34bp reads in the stem cell line dataset, 19,892,473 paired-end 100bp reads in the OVCAR8, and 21,855,632 paired-end 76bp reads in the MCF7 mapped to the human hg19 reference genome by TopHat2.0.9 [144] with up to 2 mismatches allowed. Exon coverages and read counts of exon-exon junctions were generated by SAMtools [145] to be utilized with Net-RSTQ and base EM (equation (1.7)). Cufflinks [23] directly infers transcript expressions based on the alignment by TopHat with the min isoform fraction set to 0 for better sensitivity.

TCGA RNA-Seq datasets of Ovarian serous cystadenocarcinoma (OV), Breast invasive carcinoma (BRCA), Lung adenocarcinoma (LUAD) and Lung squamous cell carcinoma (LUSC) were analyzed for patient outcome prediction with transcript expressions estimated by Net-RSTQ, base EM (equation (1.7)), RSEM [24] and Cufflinks [23]. Both the gene expression and transcript expression data reported by RSEM [24] in TCGA (level 3 data) were utilized as two baselines for cancer outcome prediction. The raw RNA-Seq fastq files (level 1 data) were downloaded from Cancer Genomics Hub (CGHub) and processed by TopHat for use with Net-RSTQ, base EM and Cufflinks. The patient samples in each dataset were classified into cases and controls based on the survival and relapse outcomes as shown in Table 4.3. The command lines for preparing the data with RSEM and Cufflinks are available in the S3 Text in [36].

Cancer Type	**Event**	**# of Patients by years**
Ovarian serous cystadenocarcinoma(OV)	Survival	76(<3 ys) **vs** 62(>4 ys)
	Relapse	79(<1.5 ys) **vs** 68(>2 ys)
Breast invasive carcinoma(BRCA)	Survival	66(<5 ys) **vs** 57(>8 ys)
	Relapse	42(<5 ys) **vs** 38(>8 ys)
Lung adenocarcinoma(LUAD)	Survival	47(<2 ys) **vs** 56(>3 ys)
Lung squamous cell carcinoma(LUSC)	Survival	67(<2 ys)**vs** 77 (>3 ys)

Table 4.3: **Summary of patient samples in TCGA datasets.** The samples are classified by cutoffs on survival and relapse time based on the available clinical information in each dataset.

4.3 Results

There are six major results in this section, 1) isoform co-expression analysis on TCGA data to show the correlation with protein domain-domain interactions; 2) overlapping the DDIs and KEGG pathways to understand the transcript networks; 3) simulations for model validation and statistical analysis; 4) qRT-PCR experiments to measure the performance of transcript quantification; 5) cancer outcome prediction on TCGA data to measure the quality of transcript quantification as molecular markers; and 6) running time of Net-RSTQ.

Net-RSTQ was compared with base EM (the base model in equation (1.7)), Cufflinks [23] and RSEM (isoform expression or gene expression) [24]. The accuracy of transcript quantification was directly measured on the simulated data with ground-truth expressions and qRT-PCR data from the three cell lines. Cancer outcome prediction on four TCGA cancer datasets evaluates the potential of using isoform expressions as predictive biomarkers in clinical settings. Statistical assessment was also performed on randomized transcript networks to evaluate the significance of the results.

4.3.1 Isoform co-expressions correlate with protein domain-domain interactions

To investigate the correlation between protein domain-domain interactions and isofrom transcript co-expressions, we calculated the number of transcript pairs that are both nearby (being neighbors or having a distance up to 2) in the transcript network and highly co-expressed in the TCGA samples. The transcript co-expressions were calculated by Pearson's correlation coefficients of each pair of transcripts across all the samples in each dataset with the isoform transcript quantification by Cufflinks. The transcript pairs were then sorted by the correlation coefficients from the largest to the smallest and grouped into bins of size 1000. The number of transcript pairs that are nearby in the transcript networks out of 1000 pairs are calculated within each bin and plotted in Figure 4.3(A) and Figure 4.3(B) for the two cancer gene lists, respectively. In both Figure 4.3(A) and Figure 4.3(B), the left column shows the plots of the number of pairs that are neighbors in the transcript network, and the right column shows the plots of the number of transcript pairs with a distance up to 2 in the transcript network, among

the 1000 pairs in each bin. In all the plots, similar trends are observed in all the four cancer datasets: there are more interacting isoform pairs in the bins with higher co-expressions. For example, among the 1000 transcript pairs with the highest correlation coefficients, there are 73 interactions in the transcript network in OV dataset and thus, 73 interactions (y-axis) for bin index 1 (x-axis) is plotted in the left column of Figure 4.3(A). In all the plots, there is a clear pattern that the numbers of matched nearby transcripts in the transcript network among the 1000 pairs in the first few bins are higher than the expected average of 30 in the small network of density 3.02%, 114 in the small network of density 11.41% (with distance up to 2), 45 in the larger network of density 4.54%, and 203 in the larger network of density 20.33% (with distance up to 2). Moreover, the 2-step walk clearly promoted the number of overlaps with the pairs of higher co-expressions in the small network. For example, the significant overlap is extended from the first 25 bins to approximately the first 50 bins or more in the four datasets. The observation suggests that higher co-expressions exist not only in the direct neighbors in the transcript network but also the nearby nodes by a small distance. By exploring the network structure with prior information through neighbors by many steps in iterations, Net-RSTQ model is expected to propagate the expression values from each transcript to its nearby nodes in the network to capture the co-expressions. Note that considering the neighboring pairs with distance up to 2 in the larger network will result in a graph of density 20.33%, which is likely to contain too many false relations by the two-step walk. Thus, the plots of the larger network of distance-2 pairs are only included for the completeness of the analysis.

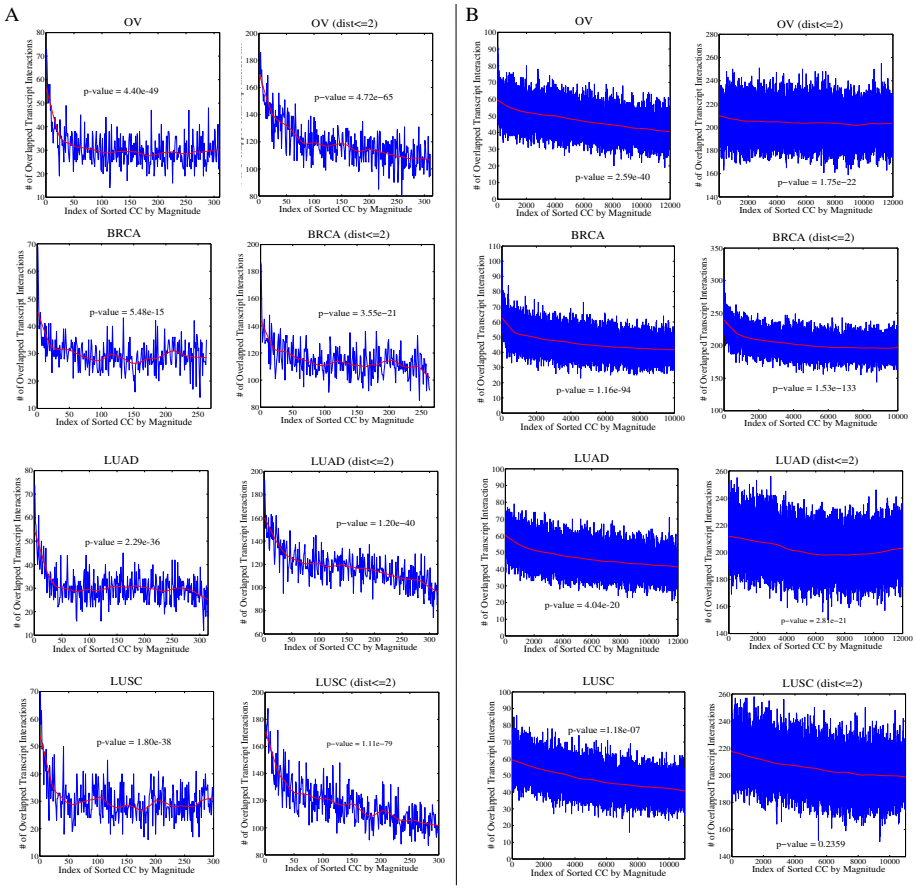

Figure 4.3: **Correlation between transcript co-expression and protein domain-domain interaction in TCGA datasets.** The correlation coefficients between transcript expressions across all patient samples are first calculated in each dataset for each pair of transcripts by Cufflinks. The correlation coefficients are then sorted from largest to smallest and grouped into bins of size 1000 each. The x-axis is the index of the bins with lower index indicating larger correlation coefficients. The y-axis is the number of the pairs among the 1000 pairs of transcripts in each bin coincide with protein domain-domain interaction between the transcript pair. The red line is the smooth plot by fitting local linear regression method with weighted linear least squares (LOWESS) to the curves. p-value is reported by chi-square test. (A) Co-expressions are calculated based on the small gene list. (B) Co-expressions are calculated based on the large gene list. In both (A) and (B), the left column shows the plots based on the connected transcript pairs in the transcript network and the right column shows the plots based on the transcript pairs with distance up to 2 in the network.

The canonical 2x2 chi-square test was also applied to compare the number of the domain-domain interactions in the first 10,000 transcript pairs (first 10 bins) with the number in the rest of the pairs. In all the four datasets in both Figure 4.3(A) and Figure 4.3(B) with one exception in the LUSC dataset on the large network of distance-2 relation, there is a significant difference that the highly co-expressed transcripts are more likely to interact with each other in the transcript network, confirmed by the significant p-values. As explained previously, the exception is likely due to the large number of false-positive pairs in the dense network. The observation further support the hypothesis that protein domain-domain interactions correlate transcript co-expressions reported in previous studies [130, 131].

To further understand the specificity of the domain-domain interactions in the highly co-expressed transcripts, we calculated the number of domain-domain pairs that construct the DDIs in the top 10,000 co-expressed transcript pairs. The statistics suggest high diversity of the type of DDIs. For example, there are 547 interacting transcript pairs among the 201 out of 898 transcripts in the top 10,000 co-expressed transcript pairs in OV dataset for small network. The 547 interacting transcript pairs represent 770 different domain-domain interactions (There might be more than one DDIs between a pair of transcripts). There are 739 interacting transcript pairs among the 538 out of 5599 transcripts in the top 10,000 co-expressed transcript pairs in OV dataset for large network. The 739 interacting transcript pairs represent 1277 different domain-domain interactions. The statistics suggest that the correlation between protein domain-domain interactions and transcript co-expressions is not a bias due to a few highly spurious DDIs. It is a general correlation in many different DDIs and co-expressed transcripts. Very similar statistics were observed in all the datasets and both networks.

To further demonstrate the co-expression relations in the transcript network, two examples are shown in S1 Figure in [36]. In S1(A) Figure, WHSC1L1 contains two isoforms connected with different interactions in the transcript network. Isoform NM_017778 interacts with 12 transcripts with average correlation coefficients 0.22 and the other isoform NM_023034 interacts with 13 more transcripts with average correlation coefficients 0.30 compared with the average correlation coefficient 0.188 against the other unconnected isoforms across the samples in the OV dataset. In S1(B) Figure, gene BRD4 contains two isoforms both of which are connected with the same 14 neighbors

in the network. The average correlation coefficients between these two isoforms and the 14 neighboring isoforms are both above 0.26 compared with the average correlation coefficient less than 0.15 against the other unconnected isoforms across the samples on the BRCA dataset. In both examples, we observed high degree of agreement between co-expressions and DDIs.

4.3.2 Protein domain-domain interactions enrich KEGG pathways

To further understand the transcript networks, we overlapped the DDIs between genes in the two networks with the 294 human KEGG pathways [146]. Among the 397 genes in the small network, 10.97%(17284) of the pairs are co-members in at least one KEGG pathway. The 10.97% KEGG co-member pairs covers 42.70%(2122) of the DDIs among the genes while the other 89.03%(140352) non-co-member pairs covers 57.30%(2748) of the DDIs. By these numbers, there is about 6-fold enrichment of DDIs in the KEGG co-member genes in the small network. Among the 2551 genes in the large network, the 5.15%(335372) KEGG co-member pairs covers 12.45%(40812) of the DDIs among genes while the other 94.85%(6172229) non-co-member pairs covers 87.55%(287090) of the DDIs. By these numbers, there is about 2.6-fold enrichment of DDIs in the KEGG co-member genes in the large network. We also list the KEGG pathways that are highly enriched with DDIs in the large network in S4 Table in [36]. Specifically, we consider the subnetwork of genes that are members of one KEGG pathway and calculated the density of DDIs in the subnetwork to compare to the overall density of 5.04% in the whole network. Interestingly, most of the enriched pathways are signaling pathways and disease pathways with very high DDI densities.

4.3.3 Net-RSTQ captures network prior in simulations

In the simulations, we applied flux-simulator [147] to generate paired-end short reads simulating real RNA-Seq experiment *in silico* based on a ground truth transcript expression profile, using hg19 reference human genome and RefSeq annotations downloaded from UCSC Genome Browser. To generate the ground-truth expression profiles, the gene expressions were sampled from a poisson distribution and the proportions of the isoforms in each gene were derived based on a neighbor average expression in the small

transcript network and an initial mixed power law expression profile with gaussian noise. A sequential updating was used to compute the proportion of each isoform by adding the neighbors' average expressions to the initial expression. The update procedure can be found in the S2 Text in [36]. At last, flux-simulator was applied to simulate the short reads based on the ground truth transcript expression file. 15 million 76-bp paired reads were generated by Flux Simulator and mapped to the reference genome by TopHat [144] with up to two mismatches allowed. To account for the large dynamic range of abundances, the expressions were normalized by $\log 2(\text{expression}+1)$.

The correlation coefficients between the transcript abundances estimated by Net-RSTQ under various λ, base EM (equation (1.7)), Cufflinks and RSEM, and the ground truth transcript abundances are reported in Figure 4.4. Furthermore, Net-RSTQ was also tested with 100 randomized networks with permuted indexes of transcripts in the transcript network. To assess the impact of the network prior, two cases are shown. Figure 4.4(A) reports the correlation between the transcripts in which isoforms coded by the same gene are connected with different neighbors (109 out of 898 transcripts in 29 genes). Figure 4.4(B) reports the results from all the genes with more than one isoform (712 out of 898 transcripts in 211 genes). In both comparisons, the transcript expressions estimated by Net-RSTQ achieve higher correlation with the ground truth compared with base EM, Cufflinks and RSEM. Slightly higher improvement was observed in the first case than in the second case since the network prior plays more significant role in differentiating the isoform expressions by their different neighbors. When randomized networks are used, Net-RSTQ leads to similar or worse results due to the wrong prior information. Note that since the datasets were generated to partially conform to the network prior, the isoform expressions are relatively "smooth" among the neighboring isoforms. Net-RSTQ tends to generate smoother expressions than base EM, Cufflinks and RSEM. When applying Net-RSTQ with small λs and randomized network priors, slight improvement was also observed due to the smoothness assumption on the data.

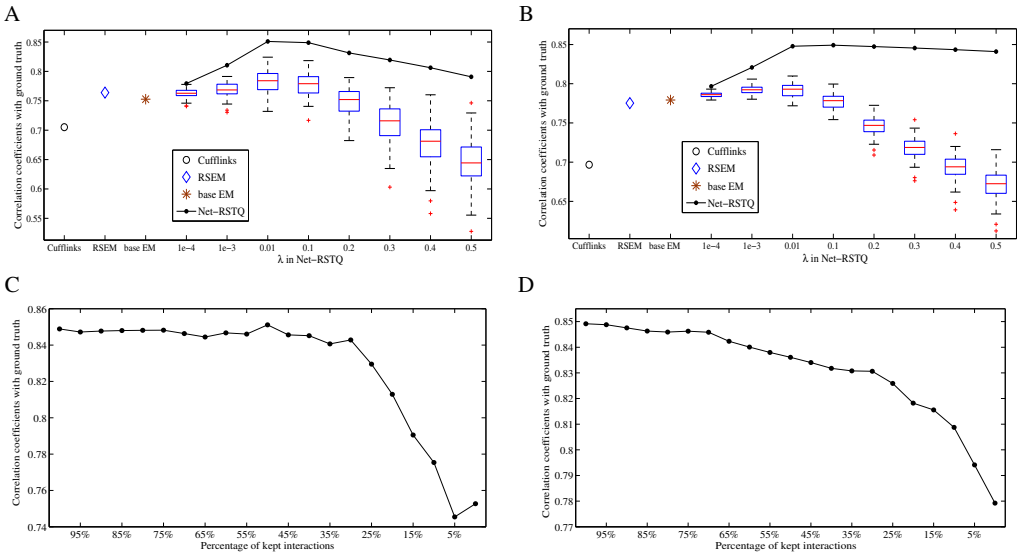

Figure 4.4: **Correlation between estimated transcript expressions and ground truth in simulation.** In (A) and (B) x-axis are labeled by the compared methods and different λ parameters of Net-RSTQ. The bar plots show the results of running Net-RSTQ with 100 randomized networks. In (C) and (D), x-axis are are the percentage of edges that are removed from the networks. The plots show the results of running Net-RSTQ with the incomplete networks. (A) and (C) report the results of 109 transcripts of the isoforms in the same gene with different domain-domain interactions. (B) and (D) report the results of 712 isoforms in genes with multiple isoforms.

To evaluate the effect of missing edges in the transcript network due to the undetected protein domain-domain interactions, we randomly removed certain percentages of the edges in the transcript network and then run Net-RSTQ with $\lambda = 0.1$ on the incomplete networks. The results are shown in Figure 4.4 (C) and (D) for the 109 transcripts with different neighbors and the 712 transcripts in the gene with more than one transcript, respectively. It is intriguing to observe that only when a large percentage of the edges are removed, the performance of Net-RSTQ is affected. Intuitively, the observation can be explained by the fact that the Dirichlet prior parameter is proportional to the average of the neighbors' expressions. As long as some of the neighbors are still connected to the target transcript in the network, the prior information is still useful. The result suggests that Net-RSTQ is relatively robust to utilize transcript networks

potentially constructed with a large percentage of undetected protein domain-domain interactions.

4.3.4 Three qRT-PCR experiments confirmed overall improved transcript quantification

The isoform proportions estimated by Net-RSTQ, base EM, RSEM, and Cufflinks were compared to the qRT-PCR results on the three cell lines. Parameter $\lambda = 0.1$ was fixed in all the Net-RSTQ experiments. Among the genes that Net-RSTQ, base EM, RSEM, and Cufflinks report most different quantification results, qRT-PCR experiments were performed to test the genes with relatively higher coverage of RNA-Seq data, coding two to three isoforms, and the feasibility of designing isoform-specific primers in the qRT-PCR products (see S1, S2 and S3 Tables in [36]). Twenty-five genes in total were tested in the three cell lines: seven in H9 stem cell line, five in OVCAR8 ovarian cancer cell line, and thirteen in MCF7 breast cancer cell line. The scatter plots of the relative abundance of the first transcript in each gene estimated by Net-RSTQ, base EM, Cufflinks and RSEM were compared to the qRT-PCR results in Figure 4.5(A) and (E). In the scatter plot, the estimated relative abundance by Net-RSTQ were closer to qRT-PCR results measured by the accuracy of various thresholds and Root Mean Square Errors. Net-RSTQ achieved the lowest Root Mean Square Error of 0.291, which is more than 0.05 less than 0.3435, the second best achieved by RSEM. In the 20% confidence region, Net-RSTQ puts 59.3% of the pairs in the region compared with 37%, 29.6%, and 51.9% by base EM, Cufflink, and RSEM, respectively. RSEM performed well by putting 37.0% of the pairs within 10% confidence regions but performed poorly in about half of the pairs with more than 25% error.

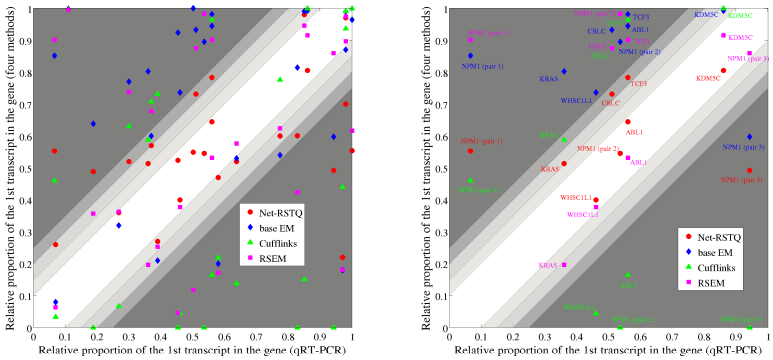

(A) All three cell lines

(B) H9 stem cell line

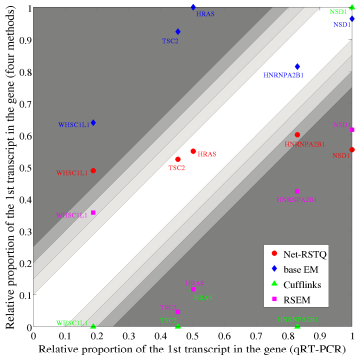

(C) OVCAR8 ovarian cancer cell line

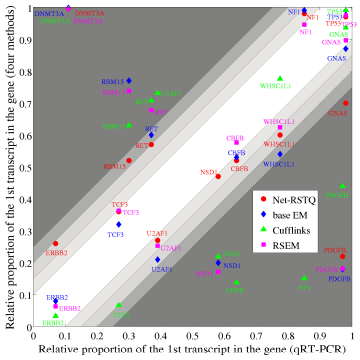

(D) MCF7 breast cancer cell line

	Cut-off	Net-RSTQ	base EM	Cufflink	RSEM
Accuracy	0.1	29.6%	18.5%	18.5%	37.0%
	0.15	44.4%	33.3%	22.2%	40.7%
	0.2	59.3%	37.0%	29.6%	51.9%
	0.25	74.4%	44.4%	33.3%	51.9%
Root Mean Square Error		0.2915	0.3701	0.4111	0.3435

(E) Accuracy and correlation

Figure 4.5: **Validation by comparison with qRT-PCR results.** (A) The scatter plots compare the reported relative proportion of each pair of the isoforms of each gene between the computational methods (Net-RSTQ, base EM, Cufflinks, and RSEM) and qRT-PCR experiments. The proportions of the two compared isoforms in a pair are normalized to adding to 1. The x-axis and y-axis are the relative proportion of one of the two isoform (the other is 1 minus the proportion) reported by qRT-PCR and the computational methods, respectively. The scatter points aligning closer to the diagonal line indicate better estimations by a computational method matching to the qRT-PCR results. The unshaded gradient around the diagonal line shows the regions with scatter differences less than 0.1, 0.15, 0.2 and 0.25, within which the estimations are more similar to the qRT-PCR results. (B)-(D) The scatter plots on each individual dataset. (E) The table shows the percentage of predictions by each method within the unshaded regions and the overall Root Mean Square Error of the predictions by each method compared to the qRT-PCR results.

The relative abundance of the seven genes in H9 stem cell line is shown in Figure 4.5(B), S2(A) Figure and S5 Table in [36]. In all seven genes tested, the relative abundance estimated by Net-RSTQ is closer to the qRT-PCR results compare to that by base EM and Cufflinks. RSEM performed similarly well on four genes and worse on the other three genes, CBLC, TCF3 and NPM1. The same comparison on the five selected genes in OVCAR8 ovarian cancer cell line is shown in Figure 4.5(C), S2(B) Figure and S6 Table in [36]. Cufflinks reports very low expressions in the first transcript in four genes, three of which do not agree with the highly expressed transcript in the qRT-PCR results. While base EM performed better for two genes (NSD1 and HNRNPA2B1), Net-RSTQ performed better on the other three genes (HRAS, TSC2, and WHSC1L1). Net-RSTQ correctly predicted the overall enrichment of isoforms of HNRNPA2B1 and NSD1 (NM_031243 > NM_002137 in HNRNPA2B1 and NM_022455 > NM_172349 in NSD1). It is possible that the expressions of NM_002137 transcript in gene HNRNPA2B1 and NM_172349 in gene NSD1 were slightly over-smoothed by network information in Net-RSTQ with the fixed λ parameter. RSEM performed slightly better on WHSC1L1 and NSD1 but much worse in the other three genes. The same comparison on the thirteen genes in MCF7 breast cancer cell line is shown in Figure 4.5(D), S2(C) Figure and S7 Table in [36]. Cufflinks performed poorly on 8 genes with more than 25% error while RSEM, base EM and Net-RSTQ performed poorly on 5, 4 and 3 genes, respectively. Overall, Net-RSTQ performed better than base EM and Cufflinks and slightly better than RSEM. In summary, Net-RSTQ improved the overall isoform quantification significantly in the H9 stem cell data and predicted more consistent cases in OVCAR8 and MCF7 cancer cell lines data. Note that there could be more uncertainties in primer designs due to somatic DNA variations and cell differentiation and proliferation in cancer cell lines, potentially a larger variation in the qRT-PCR experiments on the cancer cell lines is expected than H9 stem cell line.

4.3.5 Net-RSTQ improved overall cancer outcome predictions

To provide an additional evaluation of the quality of transcript quantification, we designed six cancer outcome prediction tasks by the assumption that better transcript quantification always leads to better isoform markers for cancer outcome prediction. Net-RSTQ was compared with base EM, RSEM [24], and Cufflinks [23] by classification

with the quantification of isoform transcripts in two cancer gene lists (397 and 2551 genes) on four cancer datasets. Each dataset is divided into four folds with two folds for training, one fold for validation (parameter tuning), and one fold for test in a four-fold cross-validation. Support Vector Machine (SVM) with RBF kernel [49] were chosen as the classifier. We repeated the four-fold cross-validation 100 times by each method in each dataset.

The average area under the curve (AUC) of receiver operating characteristic of the 100 repeats are reported in Table 4.4 when the small gene list was used and Table 4.5 when the large gene list was used. The transcript expressions estimated by Net-RSTQ consistently achieved better average classification results than those by the base EM. To evaluate the statistical significance of the differences between the AUCs generated by Net-RSTQ and the base EM in the 100 repeats, we also report the p-values by a binomial test on the number of wins/loses in all the experiments between Net-RSTQ and the base EM in Table 4.4 and Table 4.5. When the small gene list was tested, three cases were significant with low p-values less than 0.001 and two cases were significant with p-values just below 0.02 while in the BRCA (survival) data, the p-value is only moderately significant even though the average by Net-RSTQ is higher. Overall, Net-RSTQ outperformed the base EM significantly. When the larger gene list was tested, the improvements are not as significant. The improvement was only significant in one dataset, BRCA (survival), and slightly significant in two datasets, OV (relapse) and LUSC (survival). In the other three datasets, the improvements are not significant. Net-RSTQ also outperformed Cufflinks and RSEM (transcript or gene) in five cases except the experiment on BRCA (relapse) dataset in Table 4.4. In Table 4.5, the improvements are less obvious. Moreover, the isoform expression features are not more informative than gene expression features. Overall, the classification performance with the small gene list in Table 4.4 is generally better than or similar to the large gene list in Table 4.5 possibly suggesting less relevance to survival and relapse in the large gene list.

Dataset	OV(Survival)	OV(Relapse)	BRCA(Survival)	BRCA(Relapse)	LUAD(Survival)	LUSC(Survival)
Net-RSTQ(Isoform)	**0.5973**	**0.6070**	**0.6826**	0.5902	**0.6353**	**0.5666**
base EM(Isoform)	0.5696	0.5886	0.6727	0.5419	0.5789	0.5496
RSEM(Isoform)	0.5865	0.5501	0.6510	**0.6156**	0.6132	0.5362
Cufflinks(Isoform)	0.5630	0.5770	0.6762	0.5933	0.5554	0.5563
RSEM(Gene)	0.5911	0.5804	0.6513	0.5581	0.6151	0.5585
p-value(Net-RSTQ vs base EM)	0.0011	0.0198	0.1356	2.248e-5	1.948e-8	0.0167

Table 4.4: **Classification performance of estimated transcript expressions and gene expression on the small cancer gene list.** The mean AUC scores of classifying patients by estimated transcript (gene) expression in four-fold cross-validation for each dataset are reported. The best AUCs across the five models using isoforms as features are bold.

Dataset	OV(Survival)	OV(Relapse)	BRCA(Survival)	BRCA(Relapse)	LUAD(Survival)	LUSC(Survival)
Net-RSTQ(Isoform)	0.5989	**0.5852**	0.6793	0.5920	0.6038	**0.5662**
base EM(Isoform)	0.5901	0.5720	0.6509	0.5710	0.5971	0.5555
RSEM(Isoform)	0.5842	0.5694	0.6629	0.5935	0.5867	0.5432
Cufflinks(Isoform)	0.5623	0.5819	**0.6825**	0.5800	0.5834	0.5591
RSEM(Gene)	**0.6041**	0.5766	0.6746	**0.5980**	**0.6266**	0.5535
p-value(Net-RSTQ vs base EM)	0.3798	0.0967	0.0018	0.3822	0.6178	0.1356

Table 4.5: **Classification performance of estimated transcript expressions and gene expression on the large cancer gene list.** The mean AUC scores of classifying patients by estimated transcript (gene) expression in four-fold cross-validation for each dataset are reported. The best AUCs across the five models are bold.

The parameter λ was tuned by the AUC on the validation set and the optimal λ was used to train the Net-RSTQ model to be tested on the test set. The process is repeated for each fold in 100 repeats. To show the effect of varying the λ on the classification performance in Net-RSTQ, we plotted the average AUC on the validation set across the 100 repeats on the BRCA (survival) dataset with small gene list in S3(A) Figure in [36]. The optimal λ was 0.1 in this experiment. The local gradient around the optimal λ suggesting that the transcript network is playing an important role in inferring better transcript quantification from the RNA-Seq data. In S3(B) Figure in [36], the convergence of Net-RSTQ is also illustrated by each update through all the genes in each iteration. After less than 10 overall iterations across 397 genes, Net-RSTQ converged well to a local optimum. Similar convergence patterns were observed in all other TCGA samples.

To understand the role of the transcript network in the transcript expression estimation, we used 100 randomized networks to learn the transcript proportion in each experiment with λ fixed to be 0.1. In each randomization, the edges were shuffled

among all the transcripts in the small gene list. For transcript expressions learned by each randomized network, we conducted the same four-fold cross validation to compute the average AUCs among 100 repeats. The boxplot of the AUCs learned with the 100 randomized networks is shown in Figure 4.6. Compared with the classification results from the true transcript network, the result with randomized networks is always worse. Another important observation is that, the median value of the AUCs across the 100 randomized networks is lower or close to the result by the base EM, which suggests that the randomized networks play no role in improving classification and even lead to worse result. Overall, the results provide a clear evidence that the transcript network is informative for the transcript expression estimation, and supplies more discriminative features for cancer outcome prediction.

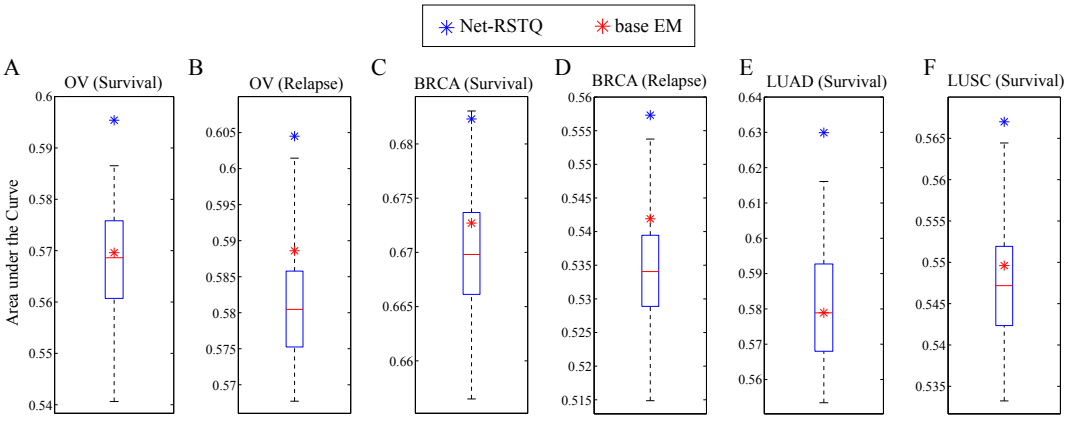

Figure 4.6: **Statistical analysis with randomized networks.** Comparison of the classification results by the randomized networks and the true network. The λ parameter was fixed to be 0.1 in all the experiments. The blue star and the red star represent the results with the real network and without network (base EM), respectively. The boxplot shows the results with the randomized networks.

4.3.6 Running time

To measure the scalability of Net-RSTQ, we tested the Net-RSTQ algorithm on the data of the MCF7 breast cancer cell line with three different networks, the small network (898 transcripts), the large network (5599 transcripts) and an artificial huge network

(10000 transcripts). Figure 4.7 plots the CPU seconds of running Net-RSTQ on the three networks under different λs. On the small network, the running time is at most about 100 seconds while on the large network and the huge network, the running time is in the scale of 1-e^3∼1-e^4 and 1-e^5∼1-e^6, respectively. When $\lambda = 0.1$, the CPU time for the small network is 32.4 seconds; for the large network is 2755 seconds; and for the artificial large network is 27806 seconds. The results suggest that Net-RSTQ might scale up to about 10000 transcripts, and thus the performance is sufficient for studies focusing on any pathway with up to several thousand genes in the pathway.

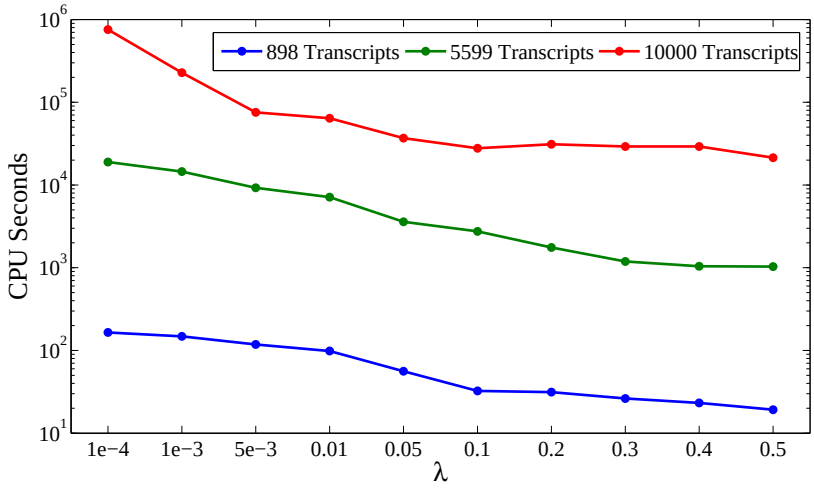

Figure 4.7: **Running time.** The plots show the CPU time (Intel Xeon E5-1620 with 3.70GHZ) for running the Net-RSTQ algorithm one three networks, the small transcript network, the large transcript network, and an artificial huge network of 10000 transcripts.

4.4 Discussion

In the study, we explored the possibility of improving short-read alignment based transcript quantification with relevant prior knowledge, protein domain-domain interactions. The observation of the correlation between isoform co-expressions and protein domain-domain interactions suggests that the approach is a well-grounded exploration. Different from previously methods [22], Net-RSTQ is a network-based approach that directly incorporates protein domain-domain interaction information for transcript proportion

estimation. The experiments suggested a great potential of exploring protein domain-domain interactions to overcome the limitations of short-read alignments and improve transcript quantification for better sample classification.

The Dirichlet prior from the neighboring isoforms play two different roles: differentiating isoform expressions to reflect different functional roles or smoothing isoform expressions to reflect similar functional roles, depending on whether the isoforms of a gene share the same or different interacting partners. This principle in modeling is based on the hypothesis that isoforms playing different functional roles (e.g. containing different protein domains) are more likely to behavior differently than isoforms with the same or similar functional roles (e.g. containing the same protein domains). When the isoforms of a gene interact with different partners, their expressions correlates with their partners' expressions. And, when the isoforms of a gene interact with the same partners, there is no benefit on differentiating their proportions to drive the functionality. A limitation is that when the functional difference among the isoforms are not captured by domain content, the smoothing role might under-estimate the difference in their proportions. Thus, our future goal is to bring in other type of functional information to distinguish their functional roles in cancer such as preferential adoption of post-transcriptional regulations.

Currently, Net-RSTQ does not directly model multi-hits reads in multiple loci. In the TCGA experiments, around 5-10% of the aligned reads in four datasets have multiple alignments reported by TopHat and only one of the best alignments is considered. To check the effect of the multiple-alignment reads in transcript quantification, we allow up to 20 best alignments by TopHat and normalized the read assignment q_{ijk} by the number of loci that the reads aligned to. The correlation coefficients between the estimated gene expressions before and after the normalization are above 0.98 in all the datasets. A potential rigorous solution is to add iteratively reassignment of the reads to the potential origins based on updated abundance of the involved isoforms. The modification will significantly decrease the computational efficiency and make it impractical on large RNA-Seq datasets.

There is also another alternative of integrating the network information directly as a regularization term on the joint likelihood function of all the genes. We also explored this model in the S1 Text in [36]. In the preliminary experiments, we observed very similar

outputs between the alternative model and the Net-RSTQ model shown in S8 Table in [36]. However, since the alternative model directly works with one large optimization problem across all the genes, the convergence is much slower as shown in S4 Figure in [36] and the optimization package used in the experiments ran into numerical issues. Thus, we believe the Net-RSTQ model is more scalable and robust in comparison.

Currently, Net-RSTQ can scale on transcript network with up to around 5000 transcripts, which is sufficient for more focused analysis of several thousand genes. The running time of Net-RSTQ on such large transcript network is below 2 hours on each TCGA sample, compared with 5-8 hours needed for aligning the short reads. To further scale up Net-RSTQ, we will investigate other faster strategies of utilizing short read information, such as Sailfish [148] which directly estimates isoform expressions by counting k-mer occurrences in reads rather than reads from the alignments. This will be our future direction.

Chapter 5

Detecting mRNA 3'-UTR shortening in mTORC1 activated MEFs

5.1 Introduction

In eukaryotes, a large portion of mRNAs contains multiple polyadenylation signals (PASs) in their 3'-untranslated region (3'-UTR). Alternating the usage of PAS, namely alternative cleavage and polyadenylation (ApA), produces mRNA isoforms with the same coding capacity but with various lengths of 3'-UTR [7, 149–151]. As 3'-UTR provides a binding platform for microRNAs and RNA-binding proteins, it serves as an important determinant for mRNA fate such as translation and stability [149,150,152,153]. Therefore, ApA provides an additional layer of complexity in regulating gene expression at the posttranscriptional level. Powerful high-profiling technologies focusing on 3'-UTRs of mRNAs provided high-resolution snap shots of alternatively polyadenylated mRNA isoforms in various tissues and cells across many species [4,153–157]. An important insight that emerged from these studies is that 3'-UTR length undergoes dynamic changes under pathogenic conditions such as cancer and in diverse biological processes such as cell proliferation, differentiation and development [23, 149, 153, 154, 158, 159]. Although the information on alternative polyadenylation sites in transcriptomes across

different species and tissues is rapidly accumulating, it is not clear what cellular mechanism(s) controls the switches between proximal and distal polyadenylation sites and how this process is regulated.

The mammalian target of rapamycin (mTOR) pathway is crucial for regulating cell proliferation/growth and its dysregulation causes many human diseases [160]. mTOR exists as two distinctive multi-protein complexes, mTORC1 and mTORC2. Raptor and Rictor are specific components of mTORC1 and mTORC2, respectively, and they are essential for cellular function of each mTOR complex [160, 161]. mTORC1 is negatively regulated by tuberous sclerosis complexes (TSC1 and TSC2) and is an evolutionarily conserved kinase that phosphorylates the ribosomal protein S6 kinases and the eukaryotic initiation factor 4E-binding proteins for efficient translation [160, 161]. Recent studies identified cis-acting elements in mRNAs such as 5'-terminal oligopyrimidine tract (TOP) or 5'-pyrimidine-rich translational element (PRTE) that render the association of a transcript with polysomes. mRNAs containing these elements in their 5'-UTRs encode proteins for cellular pathways including translation, cell invasion and metastasis, suggesting their relevance in cancer pathogenesis [162, 163]. mTOR also plays an important role for activating transcriptional networks and regulates multiple cellular pathways for lipid and nucleotide metabolism [164,165]. Recently, mTOR was shown to play a role in the regulation of proteasome activity by upregulating a transcription factor Nrf-1 (ref. [166]). Although these studies were mainly focusing on the role of mTOR in the synthesis of proteins, lipids and nucleic acids through transcriptional networks, whether mTOR is involved in other cellular processes by modulating gene expression at posttranscriptional level is relatively unclear.

In this study, we used isogenic non-cancerous mouse embryonic fibroblast (MEF) cell lines to understand changes of molecular features on dysregulated activation of mTOR. We employed RNA sequencing (RNA-seq) and two-dimensional liquid chromatography tandem mass spectrometry (2D LC-MS/MS) approaches to investigate the changes at high resolution and found an unexpected link between mTOR and ubiquitin-mediated proteolysis pathway through 3'-UTR shortening. These findings expand our understanding of mTOR to regulation of RNA processing and protein degradation pathways.

5.2 Results

5.2.1 3'-UTR shortening of mRNAs is caused by mTOR activation and is a down stream target of mTORC1

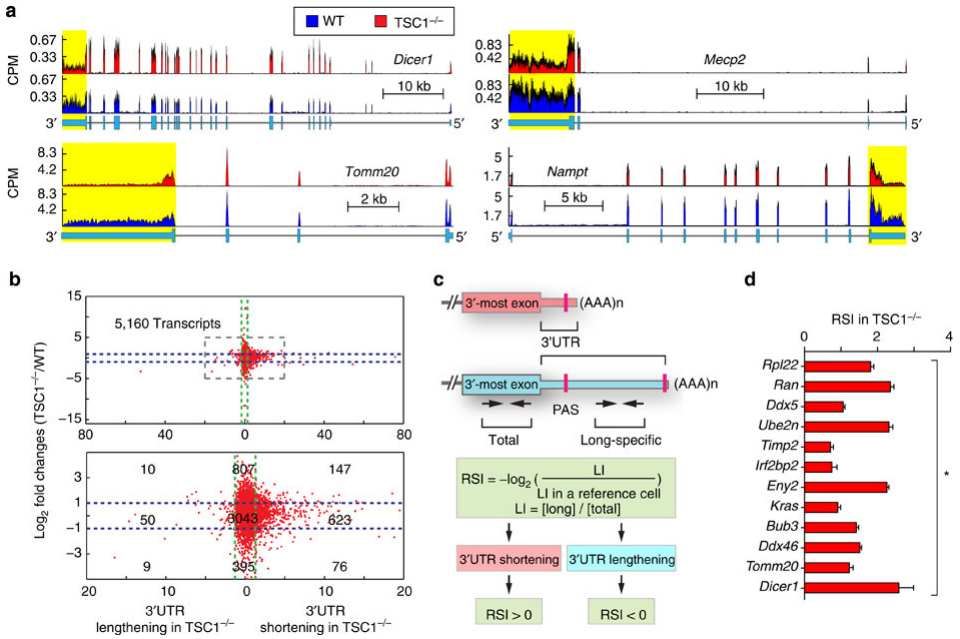

Figure 5.1: **mTOR activation leads to genome-wide 3'-UTR shortening.** (a) RNA-seq reads from WT and TSC1$^{-/-}$ are aligned to mouse genome mm10 RefSeq. Representative examples of transcripts with 3'-UTR shortening are presented. Annotated gene structures are at the bottom of the alignment. The yellow boxes highlight the aligned reads in 3'-UTRs. (b) Scatter plot of RNA-seq data. Red dots represent individual transcripts in the analysis. Horizontal blue-dashed lines represent the cutoff values for twofold changes in differential gene expression. Vertical green-dashed lines represent the cutoff values for $\log_{10}$ (p-value) of 3'-UTR shortening (1.3 corresponds to p-value=0.05) in TSC1$^{-/-}$ and WT, which was determined by χ^2-test. (c) A schematic presenting primer sets for RT-qPCR and the RSI determination. Pairs of primers were used to detect a total (short+long) or a long-specific transcript. The RSI was calculated to determine the 3-UTR shortening in a target cell line by RT-qPCR. (d) Validation of RNA-seq data. Error bars represent s.e. from three repeats of experiments. Student's t-tests are done for statistical significance. $*p\text{-}value < 0.0025$.

To explore mTOR function in gene expression at a single nucleotide resolution, we performed RNA-seq experiments (Supplementary Table 1 in [34]) using Tsc1 knockout ($TSC1^{-/-}$) and wild-type (WT) MEF cells [167]. Knockout of Tsc1, a negative regulator of mTOR, leads to uncontrolled mTOR hyperactivation compared with WT [167, 168]. One of the striking features in our data set was that many transcripts in $TSC1^{-/-}$ showed an abrupt signal drop only for a segment of the 3'-most exon of an annotated gene compared with WT (Fig.1a and Supplementary Fig.1a in [34]). For example, the read signal for Dicer1 in $TSC1^{-/-}$ dropped after the termination codon in the 3'-most exon, although the signal from upstream exons increased (Fig.1a). In some cases, upstream exons showed either similar (for example, Mecp2 and Tomm20) or decreased (for example, Anxa7 and Timp2) signal, although we observed the same pattern of signal drop in the 3'-most exon from $TSC1^{-/-}$ (Fig.1a and Supplementary Fig.1a in [34]). Further sequence analysis revealed that canonical or non-canonical PAS(s) exists around the regions showing the signal drop. This indicates that the synthesis of these transcripts terminated early in the 3'-most exon using the proximal PASs for polyadenylation, suggesting a predominant production of mRNA isoforms with a shorter 3'-UTR in the mTOR-activated transcriptome (Fig.1a and Supplementary Fig.1a in [34], yellow box, and Supplementary Data 1 in [34]). For some transcripts such as Tomm20 and Nampt, 3'-UTR-shortened transcripts were already present in WT where the mTOR activity is low but not entirely absent (Fig.1a and Supplementary Fig.1a in [34]). These 3'-UTR-shortened transcripts increased significantly in $TSC1^{-/-}$ (Fig.1a and Supplementary Fig.1a in [34]), indicating that individual transcripts differ in the regulation of their 3'-UTR length in response to cellular mTOR activity. As the signals from upstream exons reflecting the amount of transcripts varied among the 3'-UTR-shortened transcripts, we examined whether 3'-UTR shortening in the mTOR-activated transcriptome correlates to differential gene expression. To this end, we enriched 5,160 transcripts in our data set that are eligible for combined analysis of 3'-UTR shortening and differential expression (see Methods for details). Next, each transcript was plotted by fold changes in the differential gene expression (y axis in Fig.1b) and the significance of 3'-UTR shortening (x axis in Fig.1b). This approach identified 846 3'-UTR-shortened transcripts (about 16.4%) out of 5,160 transcripts in $TSC1^{-/-}$ (Fig.1b). Although 26.3% (223/846) of the 3'-UTR-shortened transcripts either increased (147/846) or decreased

(76/846) their expression level, a significant proportion (73.7%) of them in the mTOR-activated transcriptome remained unchanged (Fig.1b), indicating no strong correlation between the differential gene expression and the 3'-UTR shortening in the mTOR-activated transcriptome. Of note, only a small percentage (1.3%) of transcripts showed 3'-UTR shortening in WT over TSC1$^{-/-}$ MEFs. To confirm the RNA-seq data, we developed a method to determine 3'-UTR shortening or lengthening by calculating relative shortening index (RSI) (see Methods for details; Fig.1c). Twelve genes, covering a wide range of p-values, were randomly selected from the 3'-UTR shortening data set; all showed the RSI >0 in TSC1$^{-/-}$ (Fig.1d and see also Supplementary Fig.1d,e in [34] for alternative presentations of the data using different experimental and calculation methods), validating our RNA-seq data analysis. Together, these data strongly suggest that mTOR activation in cells leads to a preferred usage of proximal PAS in the 3'-most exon of mRNAs and results in transcriptome-wide 3'-UTR shortening.

To determine whether 3'-UTR shortening due to ApA is a previously uncharacterized cellular target downstream of mTOR pathway, our collaborator established a stable mTOR knockdown cell line TSC1$^{-/-}$ MEFs (TSC1$^{-/-}$ mTOR kd; Supplementary Fig.2a in [34]). The tested transcripts showed the RSI <0 in TSC1$^{-/-}$ mTOR kd MEFs as compared with a control knockdown cell line, indicating the enrichment of 3'-UTR-lengthened transcripts in mTOR-deficient cells (Fig.2a and Supplementary Fig.2b in [34]), thus supporting the idea that mTOR functions in 3'-UTR length regulation. Consistently, the same results were observed in a human embryonic kidney stable cell line and a bladder cancer cell line with the same treatment [169,170]. These results suggest that the function of mTOR in 3'-UTR shortening is a general phenomenon and evolutionarily conserved between human and mouse (Supplementary Fig.2c-e in [34]).

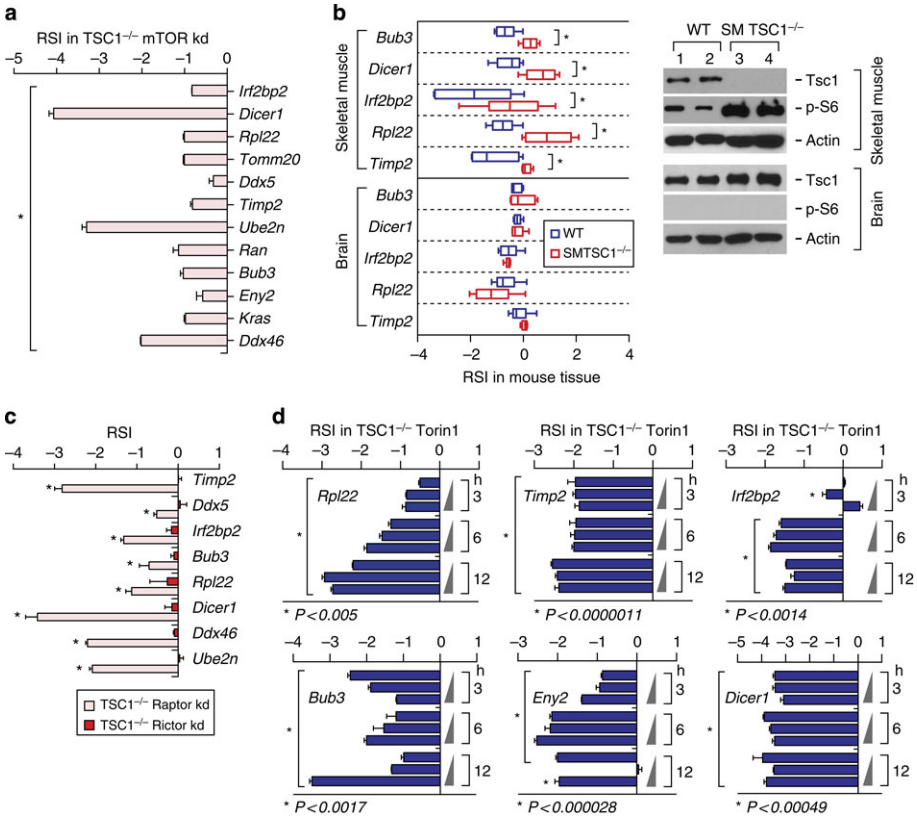

Figure 5.2: **3'-UTR shortening is a downstream target of mTORC1.** (a) mTOR knockdown (kd) in TSC1$^{-/-}$ recovers the 3-UTR length. The RSI was measured using total RNAs isolated from TSC1$^{-/-}$ MEFs with mTOR kd. $*p$-value<0.015. (b) Activation of mTOR in terminally differentiated skeletal muscle leads to 3'-UTR shortening. Total RNAs from skeletal muscles in WT or skeletal muscle-specific knockout of Tsc1 (SM TSC1$^{-/-}$) mice were used for the RSI measurement. The brain was used as an additional tissue control. Western blotting on tissue extracts from two randomly chosen mice was done. p-S6 denotes phosphorylated S6, a downstream target of activated mTOR kinase. $*p$-value<0.016. (c) mTORC1 but not mTORC2 is crucial for 3'-UTR shortening. mTORC1 or mTORC2 was specifically deactivated by targeting Raptor or Rictor, respectively, using short hairpin RNAs in TSC1$^{-/-}$ MEFs. The RSI was measured using RT-qPCR. $*p$-value<0.05. (d) A selective inhibitor of mTOR, Torin1, alters 3'-UTR length in mRNAs. TSC1$^{-/-}$ MEFs were treated with Torin1 at various doses (10, 50 and 250nM, presented as incremental triangles) and time courses (3, 6 and 12h). Changes in the 3'-UTR length were determined by measuring the RSI. $*$The conditions that accumulate the long 3'-UTR-containing transcripts with statistical significance.

Proliferative cells are known to carry short 3'-UTRs in their transcriptome and terminally differentiated tissues are known to produce transcripts with long 3'-UTRs [153, 154, 157]. We asked whether mTOR activation could be an underlying reason that explains these observations. The experiments done by our collaborator on a mouse model with skeletal muscle provide evidence that the mTOR activation is sufficient to drive 3'-UTR shortening in terminally differentiated skeletal muscles (Fig.2b and Supplementary Fig.2m in [34]).

To address which mTOR complex regulates 3'-UTR shortening, our collaborator established stable cell lines using short hairpin RNA that specifically knocks down Raptor (a component of mTORC1) or Rictor (a component of mTORC2) in $TSC1^{-/-}$ MEFs (Supplementary Fig.2g in [34]). The knockdown of Raptor but not Rictor resulted in the RSI <0 when compared with control knockdown cells, suggesting that mTORC1 plays an important role in 3'-UTR shortening (Fig.2c and Supplementary Fig.2h in [34]). mTOR is a key therapeutic target for many human disease treatments [160] and several versions of selective mTOR inhibitors have been developed including Torin1 (ref. [171]). The experiments done by our collaborator shows that the cellular ApA pattern changes drastically on the pharmacological inhibition of mTOR (Fig.2d and Supplementary Fig.2i,j,n in [34]). Furthermore, our collaborator proved that the 3'-UTR lengthening after Torin1 treatment is not caused by the inhibition of cell proliferation but rather from the inactivation of mTOR (Supplementary Fig.2r,s in [34]). Taken together, we conclude that the mTOR pathway is an upstream regulator for ApA process and determines the 3'-UTR length in the transcriptome independent of cell proliferation status.

5.2.2 3'-UTR shortening activates ubiquitin-mediated proteolysis

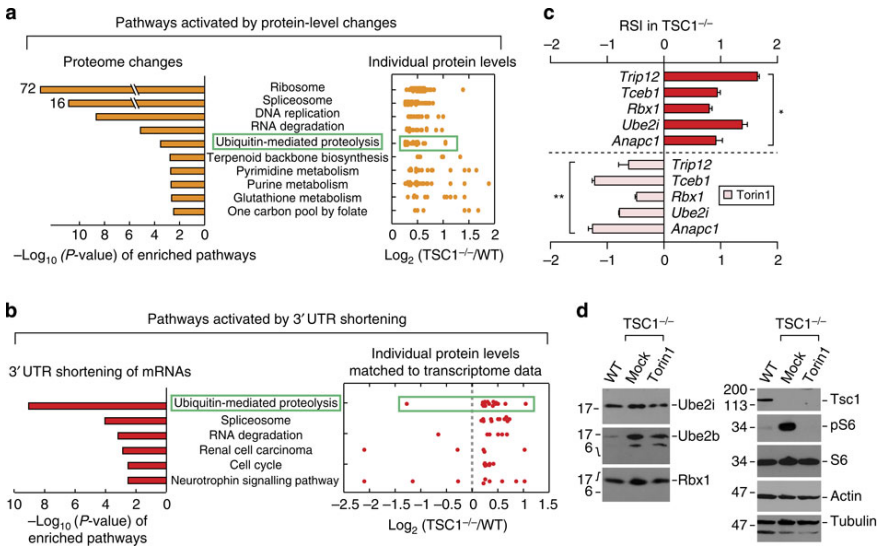

Figure 5.3: **3'-UTR shortening due to mTOR activation targets specific cellular pathways including ubiquitin-mediated proteolysis.** (a) Analysis of mTOR-activated proteome. The KEGG pathway enrichment analysis was performed using the catalogue of identified proteins from 2D LC-MS/MS. The left panel shows the enriched pathways in $\log_{10}(p\text{-value})$. The right box shows the distribution of individual proteins in each KEGG pathway index shown in the left panel. Proteins showing more than 1.2 fold changes in $TSC1^{-/-}$ compared with WT MEFs are plotted. Ubiquitin-mediated proteolysis pathway is marked with a light green box. (b) Analysis of enriched KEGG pathways by 3'-UTR shortening in $TSC1^{-/-}$ MEFs. The mTOR-activated transcriptome is described in Figure 1. The KEGG pathways enriched in $TSC1^{-/-}$ MEFs by 3'-UTR shortening are shown in $\log_{10}(p\text{-value})$. Fold changes of individual proteins in each pathway index are plotted in the right box. Ubiquitin-mediated proteolysis pathway is marked with a light green box. (c) The RSI was measured for the transcripts enriched in ubiquitin-mediated proteolysis pathway in $TSC1^{-/-}$ MEFs. The lengthening of 3'-UTR in $TSC1^{-/-}$ MEFs treated with Torin1 at 50nM for 24h was shown by the RSI. $*p\text{-value}<1.5\times10^{-6}$, $**p\text{-value}<6.3\times10^{-6}$. (d) Western blot analysis of E2 and E3 enzymes showing the 3'-UTR shortening in the RNA-seq experiments. Cells were treated with Torin1 for 24h at 50nM for 3'-UTR lengthening. pS6 denotes phosphorylated S6.

Activation of mTOR increases global protein synthesis by controlling multiple downstream events such as ribosome biogenesis and cap-dependent translation initiation and elongation [160,161]. Especially, mTOR promotes the translation of a subset of mRNAs carrying 5'-UTR sequences such as 5'TOP, 5'TOP-like motif and 5'PRTE [162, 163]. Similar to 5'-UTR, 3'-UTR in mRNA also plays an important role in the regulation of gene expression. In particular, 3'-UTR shortening in a transcript has been shown to increase protein production [150, 153, 154, 172]. Therefore, we asked whether the mTOR-activated 3'-UTR shortening contributes to mTOR-mediated upregulation of protein synthesis and influences mTOR-related biology. To this end, our collaborator first conducted quantitative proteomic studies using tandem mass tag (TMT)-labelled total cell lysates prepared from WT and TSC1$^{-/-}$ MEFs, to quantitatively profile the changes in the cellular proteome due to mTOR activation. They identified a total of 2,754 proteins that were found in either cell line by two or more unique peptides via 2D LC-MS/MS (Supplementary Data 2 in [34]). I did the KEGG (Kyoto Encyclopedia of Genes and Genomes) enrichment analysis on the catalogue of proteins with >20% increase (1,014 proteins) in abundance (TSC1$^{-/-}$ compared with WT) and found that multiple cellular pathways are activated in TSC1$^{-/-}$ (Fig.3a). We also performed the KEGG pathway analysis using the catalogue of 846 3'-UTR-shortened transcripts (Supplementary Data 1 in [34]) and the differentially expressed transcripts in TSC1$^{-/-}$ MEFs (Supplementary Fig.3a and Supplementary Data 3 in [34]). By comparing the enriched pathways from these three data sets, we found that multiple pathways in the mTOR-activated proteome such as spliceosome (mmu03040) and RNA degradation (mmu03018) are upregulated by both 3'-UTR shortening and differential gene expression, whereas other enriched pathways such as DNA replication (mmu03030) and pyrimidine/purine metabolism (mmu00240/mmu00230) are attributable solely to the differential gene expression (Fig.3a and Supplementary Fig.3a,b in [34]).

Intriguingly, among those enriched pathways in the quantitative proteome analysis, ribosome- (mmu03010) and ubiquitin-mediated proteolysis pathways (mmu04120) did not appear in the differential gene expression data set (Fig.3a and Supplementary Fig.3b,c in [34]). This indicates that these two pathways are most likely to be activated by other mTOR-mediated regulatory mechanisms rather than transcriptional regulation. It is known that the ribosome pathway is activated by mTOR through the

translational regulation of mTOR-responsive 5'-UTR cis-elements such as 5'TOP and 5'PRTE in the mRNAs [162,163,173]. On the other hand, mTOR-responsive 5'-UTR sequence elements do not exist in most transcripts from the ubiquitin-mediated proteolysis pathway, supporting the idea that 3'-UTR shortening could be an explanation for the activation of ubiquitin-mediated proteolysis pathway in the mTOR-activated proteome (the light green box in Fig.3a,b and Supplementary Fig.3d in [34]). All transcripts from the ubiquitin-mediated proteolysis pathway containing short 3'-UTR encode the components of E2 ubiquitin-conjugating enzymes and E3 ubiquitin ligases such as Anapc1, Rbx1, Trip12, Ube2i and Tceb1. Consistent with our findings in this study, these transcripts carry an mTOR-dependent short 3'-UTR in $TSC1^{-/-}$ MEFs as determined by the RSI in the presence or the absence of Torin1 treatment (Fig.3c). As shown by western blotting (Fig.3d), the expression of Ube2i, Ube2b and Rbx1 proteins matched the progression of 3'-UTR shortening in these transcripts, supporting our conclusions from quantitative proteomics studies and 3'-UTR-shortening analysis. Together, these results suggest that 3'-UTR shortening by mTOR activation plays an important role in altering gene expression. These results also identify the ubiquitin-mediated proteolysis pathway as an additional cellular target of mTOR. Thus, mTOR-driven 3'-UTR shortening might explain part of cellular phenotypic changes in $TSC1^{-/-}$ over WT MEFs.

5.3 Method

5.3.1 RNA-Seq and alignments

To evaluate transcriptome features under mTOR hyperactivation at nucleotide-wise resolution, we performed RNA-seq analysis of poly(A+) RNAs isolated from WT and $TSC1^{-/-}$ MEFs. In total, 63,742,790 paired-end reads for WT and 74,251,891 paired-end reads for $TSC1^{-/-}$ MEFs were produced from Hi-Seq pipeline with length of 50bp of each end. The short reads were aligned to the mm10 reference genome by TopHat [174], with up to two mismatches allowed. The unmapped reads were first trimmed to remove poly-A/T tails (repeats of [A/N]s or [T/N]s) from read ends/starts and then aligned to the reference genome. It is worth noting that we only retained the reads with at least 30bp in both ends after trimming. Finally, 87.1% of short reads from WT and 87.5% of sequence reads from $TSC1^{-/-}$ MEFs were mapped to the reference genome by TopHat

for ApA analysis in the study.

5.3.2 ApA analysis

To detect the potential alternative PAS of a transcript between WT and TSC1$^{-/-}$ MEFs, we evaluated candidate PAS motifs (AATAAA, ATTAAA, AGTAAA, CATAAA, TATAAA, GATAAA, ACTAAA, AATACA, AATATA, AAGAAA, AATAGA, AATGAA, TTTAAA, AAAATA, TATATA, AGATAA, ATTACA, AGAATA) [31, 175] in the 3'-UTR of the transcript by contrasting the short-read coverage up/downstream of the site across WT and TSC1$^{-/-}$ samples with χ^2-test. Specifically, we first scanned the 3'-UTR of a transcript (by mm10 annotation) to identify PAS motifs as candidates of alternative PAS. For each candidate PAS, we calculated the mean coverage upstream of the site (N and M) and downstream of the site (n and m) with (N, n) denoting the coverage in WT and (M, m) denoting the coverage in TSC1$^{-/-}$. In the calculation, the upstream region starts at the beginning of the last coding exon adjacent to the 3'-UTR of the transcript and ends at the beginning of the PAS motif site. Next, a canonical 2×2 χ^2-test was applied to report a p-value for each candidate site. The candidate PAS with the most significant p-value $\leq$0.05 was considered for further analysis. It is noteworthy that the χ^2-test will report shortening events in both WT (when N/n>M/m) and TSC1$^{-/-}$ (when N/n<M/m). Out of the 5,160 transcripts, 846 (16.4%) show a p-value $\leq$0.05 in TSC1$^{-/-}$ MEFs and 69 (1.3%) a show p-value $\leq$0.05 in WT MEFs.

5.3.3 Scatter plot for differential expression and ApA analysis

To select candidate transcripts with sufficient signal for reliable differential expression analysis and 3'-UTR-shortening identification, we first analysed the short-read alignments of the RNA-seq data against mouse mm10 reference genome using Cufflink [23]. In the alignments, 14,378 and 14,175 transcripts are considered 'expressed' in WT and TSC1$^{-/-}$ cell lines, respectively, with a FPKM (fragments per kilobase of transcript per million mapped reads) cutoff=0.17. The union of the two sets gives 15,340 transcripts that are expressed in at least one of the cell lines. We further filtered out the transcripts with positional short-read coverage $\leq$25 in the entire 3'-UTR in both cell lines. In addition, transcripts with 3'-UTR overlapping exons in the strand in opposite direction

were removed to avoid mingled short-read signals that might lead to inaccurate 3'-UTR-shortening identification. Finally, to allow precise PAS analysis, only transcripts with at least two occurrences of the 18 PAS motifs in the 3'-UTR are retained in the study. The entire pruning procedure left 5,160 transcripts for further analysis.

5.3.4 Measurement of RSI

A numerical presentation of 3'-UTR shortening was developed by calculating the RSI of a given transcript. A relative expression of total or longer 3'-UTR-containing transcripts was measured by normalizing to total amount of RNAs used in RT-qPCR analysis. The following equation was used to determine the RSI.

LI=[normalized expression of longer 3'-UTR-containing transcript]/[normalized expression of total (long+short) transcript]

RSI=$\log_2$(LI/[LI in reference cell line]); thus, RSI=0 for a reference cell line.

If RSI >0 in a target cell line, then there is a 3'-UTR shortening. If RSI <0 in a target cell line, then there is a 3'-UTR lengthening. The RSI contains the information about the changes in the proportion of a longer 3'-UTR-containing transcript in a given cellular context compared with a reference cell. For example, a value of 1 in the RSI of a transcript indicates that the proportion of the longer 3'-UTR-containing transcript of the total (long+short) transcript decreases by 50% compared with that of the reference cell line, indicating an enrichment of 3'-UTR-shortened transcript (that is, 3'-UTR shortening).

5.4 Discussion

In this study, we used genetically well-defined MEFs to investigate the molecular signatures of mTOR-activated transcriptome and discovered widespread 3'-UTR shortening due to dysregulated mTOR activation. Although a precise mechanism(s) of how mTOR activation leads to the 3'-UTR shortening in selected transcripts is unknown, we found that almost all known 3'-end processing factors alter their expression on changes in cellular mTOR activity in TSC1$^{-/-}$ compared with WT MEFs, suggesting that mTOR-mediated 3'-UTR shortening occurs by multiple factors (Supplementary Data 3 in [34]).

Analysis on pathways enriched in 3'-UTR-shortened transcripts and quantitative proteomics on mTOR activation identified ubiquitin-mediated proteolysis as an additional target pathway of mTOR. Considering the well-documented function of mTOR in the activation of cellular anabolic metabolism for rapid cell proliferation [176], the newly discovered function of mTOR in ubiquitin-mediated proteolysis through 3'-UTR shortening is surprising. A recent study suggests a role of mTOR in the activation of proteasome through the modulation of a transcriptional network [166]. This study argued that the promotion of protein degradation pathway on mTOR activation is required for a continuous supply of amino acids to cellular systems, to maintain the steady-state protein synthesis. Our data set also indicates a marginal increase in the proteasome activity through a transcriptional upregulation of several proteasomal subunits (Supplementary Fig.4d in [34]) and an increase in the polyubiquitination of proteins on mTOR activation (Supplementary Fig.4i in [34]). Moreover, our data demonstrate that mTOR-promoted 3'-UTR shortening leads to the overexpression of selected E2 and E3 components in ubiquitin ligase complexes (Figs 3b,d), which is known to increase polyubiquitination of their substrates [177–183]. Therefore, it is possible that the enrichment of polyubiquitination in cellular proteins on mTOR activation could come from selective polyubiquitination of those E2 and E3 substrates. Together, our study proposes the molecular mechanism of how mTOR pathway selects proteins to degrade through 3'-UTR shortening of a subset of mRNAs. The E2 and E3 enzymes upregulated by mTOR-driven 3'-UTR shortening mostly target cell cycle regulators, tumour suppressors and pro-apoptotic proteins for ubiquitin-proteasome system [178, 184]. For instance, Rbx1, Trip12 or Anapc1/5 are all components of E3 ligase complexes that selectively polyubiquitinate Arf and Cyclins, and Birc6 E3 ligase targets Caspase 3/7 for degradation [178, 184, 185]. For rapidly proliferating cells, a timely removal of cell cycle regulators such as Arf and Cyclins is a key step for rapid progression of the cell cycle [178]. Therefore, our findings are particularly important, because unlike a previous argument it explains how upregulated mTOR and consequent proteasome activation recycles proteins that are only needed to foster a cellular environment favourable to rapid cell proliferation. Thus, we suggest that this selective proteolysis not only provides a surplus of amino acids to cellular systems but also makes cells proliferate rapidly by efficient modulation of the cellular levels of cell cycle regulators.

Chapter 6

Conclusion and Discussion

This thesis has presented several network-based learning methods and a pipeline for utilize high-dimensional microarray gene expression and RNA-Sequencing genomic data that integrate biological prior knowledge for cancer transcriptome analysis. We approached this problem with three consecutive directions. (1) Accurate quantification of the molecular features in the genomic data. (2) Develop reliable methods to identify the reproducible cancer relevant biomarkers from all the candidate genomic features. (3) Develop robust predictive models for patient samples classification. In this chapter, we summarized the works present in the thesis based on the three directions mentioned above and then a discussion of possible extensions of the works.

6.1 Conclusion

Accurate quantification of molecular features is the crucial step in other downstream transciptome analysis such as isoform function prediction, biomarker identification, and patient samples classification. In the thesis, (1) we described a network-based method *Net-RSTQ* integrate protein domain-domain interaction network with short read alignments for transcript abundance estimation in Chapter 4. Compared to the existing methods, *Net-RSTQ* is proven a useful tool for isoform-based analysis in functional genomes and systems biology validated by qRT-PCR experiments, simulation and classification of TCGA patient samples. All the experiments suggested a great potential of exploring protein domain-domain interactions to overcome the limitations of short-read

alignments. (2) We developed a pipeline for the study in Chapter 5 to quantify the different polyadenylation sites in the 3'-UTR region for the same gene with RNA-Seq data. We then identified ApA events between $TSC1^{-/-}$ and WT based on the quantified polyadenylation with χ^2-test. The experiments support the accuracy of the identified ApA events.

Discovered biomarkers can possibly provide better prognosis and diagnosis than the current available clinical measures for risk assessment of cancer patients. Building reliable computational methods to identify reproducible cancer relevant biomarkers from high-throughput genomic data is a challenge problem. In the thesis, (1) we present network propagation models *Signed-NP* for feature selection in high-dimensional microarray gene expression for detecting differentially expressed genes in Chapter 2. (2) We introduce a network-based Cox regression model *Net-Cox* to identify relevant features for survival analysis in cancer genomics in Chapter 3. Both models presented in these two chapters introduce a graph Laplacian matrix as a smoothness requirement on the gene features linked in the gene relation network. The gene relation network is constructed by co-expression analysis or prior knowledge of gene functional relations. Compared to the existing models, introducing a gene relation network in the model capture more global relation among all the genes, such as centralities, closenesses, modularities, and subgraph structures. The experiments in Chapter 2 and 3 show that the network-based methods identified highly consistent signature genes across several datasets for the same study purpose. Moreover, the identified signature genes contain more discriminative power for cancer prediction and survival prediction compared with the marker genes identified by the other methods. One of the marker genes, FBN1, which was detected as a signature gene of high confidence by *Net-Cox* with network information, was validated as a biomarker for predicting early recurrence in platinum-sensitive ovarian cancer patients in laboratory.

Developing a predictive model based on the identified molecular features or the whole feature space for cancer patient survival prediction or classification is critical for cancer treatment and etiology. The classification model, *Signed-NPBi*, which is described in Chapter 2, is a semi-supervised learning algorithm on bipartite graphs was introduced to explore sample-feature bi-clusters for feature selection and cancer outcome classification. Large scale experiments on several microarray gene expression datasets

and CNV datasets validated that *Signed-NPBi* performed better classification of gene expression and CNV data than the existing methods. The survival prediction model, *Net-Cox*, which is described in Chapter 3 also consistently improved the accuracy of survival prediction over the Cox models regularized by L_2-norm or L_1-norm.

In summary, all models proposed in this thesis showed promising results in both simulations and experiments on real high-throughput genomic data, and the findings are useful for the cancer studies.

6.2 Future Work

In this section, we will discuss several future directions extending the work presented in this thesis.

6.2.1 Transfer learning across cancers

We introduce a transfer learning framework to discover common genomic features shared across different cancer types and cancer specific features to extend the work proposed in Chapter 2.

Suppose we have δ datasets (studies/cancer types) measured from the same p genomic features, each dataset i contains n_i samples. We can learn the common genomic features across the datasets and datasets specific features from

$$\begin{aligned}\mathcal{L}(\boldsymbol{f}_c, \boldsymbol{f}_i) &= \sum_{i=1}^{\delta} \left[\alpha(\boldsymbol{f}_c + \boldsymbol{f}_i)^T \boldsymbol{L}_i(\boldsymbol{f}_c + \boldsymbol{f}_i) + (1-\alpha)\|\boldsymbol{f}_c + \boldsymbol{f}_i - \boldsymbol{y}_i\|_2^2 + \gamma_1\|\boldsymbol{f}_i\|_1\right] \\ &\quad +\gamma_2\|\boldsymbol{f}_c\|_1, \end{aligned} \tag{6.1}$$

where $\boldsymbol{f}_c$ is the common feature vector and $\boldsymbol{f}_i$ is the feature vector specific in dataset i. Alternating optimize $\boldsymbol{f}_c$ and $\boldsymbol{f}_c$ can solve the problem in equation 6.1. When $\boldsymbol{f}_c$ is fixed, we can learn one $\boldsymbol{f}_i$ at a time, which is equivalent to solve a lasso penalized linear regression problem. The same for updating $\boldsymbol{f}_c$.

We can also extend the framework in equation 6.1 on a bipartite graph as a semi-supervised learning model to identify common cancer genomic features, cancer specific features, and classify the samples in each study simultaneously. Suppose we have δ

studies and i is the index of the studies. $\boldsymbol{S}_{(i)} = \boldsymbol{D}_{v_{(i)}}^{-\frac{1}{2}} * \boldsymbol{W} * \boldsymbol{D}_{u_{(i)}}^{-\frac{1}{2}}$.

$$\begin{aligned}\mathcal{L}(\boldsymbol{f}_{v_{(c)}}, \boldsymbol{f}_{v_{(i)}}, \boldsymbol{f}_{u_{(i)}}) &= \sum_{i=1}^{\delta}\{\|\boldsymbol{f}_{v_{(c)}} + \boldsymbol{f}_{v_{(i)}}\|_2^2 + \|\boldsymbol{f}_{u_{(i)}}\|_2^2 - 2(\boldsymbol{f}_{v_{(c)}} + \boldsymbol{f}_{v_{(i)}})^T \boldsymbol{S}_{(i)} \boldsymbol{f}_{u_{(i)}} \\ &\quad +\alpha\|\boldsymbol{f}_{v_{(c)}} + \boldsymbol{f}_{v_{(i)}} - \boldsymbol{y}_{v_{(i)}}\|_2^2 + \alpha\|\boldsymbol{f}_{u_{(i)}} - \boldsymbol{y}_{u_{(i)}}\|_2^2 \\ &\quad +\lambda_1\|\boldsymbol{f}_{v_{(i)}}\|_1\} + \lambda_2\|\boldsymbol{f}_{v_{(c)}}\|_1 \end{aligned} \tag{6.2}$$

where $\boldsymbol{f}_{v_{(c)}}$ is the common feature vector, $\boldsymbol{f}_{v_{(i)}}$ is the feature vector specific in dataset i, and $\boldsymbol{f}_{u_{(i)}}$ is the label vector for the samples in dataset i.

6.2.2 Improving transcript quantification by integrating RNA-Seq and NanoString/qRT-PCR data

We introduce an integrative model to learn the transcript expression by integrating RNA-Seq data and NanoString/qRT-PCR to provide the accurate transcript quantification with the same purpose of the algorithm, *Net-RSTQ* described in Chapter 4. Instead of providing all the individual isoform expression in the gene, NanoString or qRT-PCR only need to provide the expression of the isoform groups in the gene as a reference. For example, suppose there are five transcripts in gene A, we only need to design the primers for NanoString(or qRT-PCR) to separate the five transcripts into at least two groups, the groups can be overlapped with each other. The objective function can be formulated to learn the probability p_{ik} of a read generated by transcript T_{ik} in the i^{th} gene as follow,

$$\boldsymbol{P}_i = \arg\max_{\boldsymbol{P}_i} \left[\sum_{j=1}^{|\boldsymbol{r}_i|} log(\sum_{k=1}^{|\boldsymbol{T}_i|} p_{ik} q_{ijk}) - \lambda\|\boldsymbol{G}_i|\boldsymbol{r}_i| - \alpha \boldsymbol{E}_i\|^2 \right], \tag{6.3}$$

where $\boldsymbol{P}_i$ is the probability of a read generated by transcript $\boldsymbol{T}_i$ in the i^{th} gene, specifically, $\boldsymbol{P}_i = [p_{i1}, ..., p_{i,|\boldsymbol{T}_i|}]$. $\boldsymbol{E}_i$ is the expression of the isoform groups in the i^{th} gene estimated from NanoString(or qRT-PCR). α is a parameter make the expressions estimated by RNA-Seq and NanoString(or qRT-PCR) are comparable. $\boldsymbol{G}_i$ is the relative abundance of the isoform groups in the i^{th} gene which is a function of p_{ik}.

Equation 6.3 consists of two terms. The first term is the log-likelihood of the observed read counts in the data for gene i, and the second term encourages consistency between the expressions reported by RNA-Seq and NanoString (or qRT-PCR).

6.2.3 Identify 3'-UTR shortening by integrating RNA-Seq and PAS-Seq data

The pipeline to identify the ApA events presented in Chapter 5 is solely based on the candidate PAS motifs since the exact polyadenylation sites in the 3'-UTR region are not available. It may not accurately estimate the cleavage position from the candidate PAS to identify the ApA events. A recently developed deep sequencing-based method called Poly(A) Site Sequencing (PAS-Seq) for quantitatively profiling RNA polyadenylation at the transcriptome level [186] is available. PAS-Seq not only accurately and comprehensively identifies polyadenylation sites in mRNAs and noncoding RNAs, but also provides quantitative information on the relative abundance of polyadenylated RNAs. By integrating PAS-Seq data with RNA-Seq data, we can improve the pipeline presented in Chapter 5 with an integrative model to identify 3'-UTR shortening events.

The integrative model can be formulated to learn the probability p_{ik} of a read generated by the polyadenylated RNA C_{ik} in the i^{th} gene as follow,

$$\boldsymbol{P}_i = \arg\max_{\boldsymbol{P}_i} \left[\sum_{j=1}^{|\boldsymbol{r}_i|} log(\sum_{k=1}^{|\boldsymbol{C}_i|} p_{ik} q_{ijk}) - \lambda \| \frac{\boldsymbol{P}_i |\boldsymbol{r}_i|}{\boldsymbol{L}_i} - \alpha \boldsymbol{E}_i \|^2 \right], \tag{6.4}$$

where $\boldsymbol{P}_i$ is the probability of a read generated by the polyadenylated RNA $\boldsymbol{C}_i$ in the i^{th} gene, specifically, $\boldsymbol{P}_i = [p_{i1}, ..., p_{i,|\boldsymbol{C}_i|}]$. $\boldsymbol{L}_i$ is a vector contains the length of the 3'-UTRs for polyadenylated RNAs in the i^{th} gene. $\boldsymbol{E}_i$ is the expression of the polyadenylated RNAs in the i^{th} gene estimated from PAS-Seq. α is a parameter to make the expression estimated by RNA-Seq and PAS-Seq comparable.

References

[1] van de Vijver MJ, He YD, van 't Veer LJ, et al. (2002) A gene-expression signature as a predictor of survival in breast cancer. New England Journal of Medicine 347: 1999-2009.

[2] Van't Veer L, Dai H, Van de Vijver M, He Y, Hart A, et al. (2001) Gene expression profiling predicts clinical outcome of breast cancer. Nature 415: 530-536.

[3] Jazaeri AA, Yee CJ, Sotiriou C, Brantley KR, Boyd J, et al. (2002) Gene expression profiles of brca1-linked, brca2-linked, and sporadic ovarian cancers. Journal of the National Cancer Institute 94: 990-1000.

[4] Wang ET, Sandberg R, Luo S, Khrebtukova I, Zhang L, et al. (2008) Alternative isoform regulation in human tissue transcriptomes. Nature 456: 470–476.

[5] David CJ, Manley JL (2010) Alternative pre-mrna splicing regulation in cancer: pathways and programs unhinged. Genes & development 24: 2343–2364.

[6] Silvera D, Formenti SC, Schneider RJ (2010) Translational control in cancer. Nature Reviews Cancer 10: 254–266.

[7] Elkon R, Ugalde AP, Agami R (2013) Alternative cleavage and polyadenylation: extent, regulation and function. Nature Reviews Genetics 14: 496–506.

[8] Mayr C, Hemann MT, Bartel DP (2007) Disrupting the pairing between let-7 and hmga2 enhances oncogenic transformation. Science 315: 1576–1579.

[9] Lee YS, Dutta A (2007) The tumor suppressor microrna let-7 represses the hmga2 oncogene. Genes & development 21: 1025–1030.

[10] Peri S, Navarro JD, Amanchy R, Kristiansen TZ, Jonnalagadda CK, et al. (2003) Development of human protein reference database as an initial platform for approaching systems biology in humans. Genome Res 13: 2363-2371.

[11] Barabási AL, Gulbahce N, Loscalzo J (2011) Network medicine: a network-based approach to human disease. Nature Reviews Genetics 12: 56–68.

[12] Ulitsky I, Shamir R (2007) Identification of functional modules using network topology and high-throughput data. BMC systems biology 1: 8.

[13] Zhou D, Bousquet O, Lal T, Weston J, Scholkopf B (2004) Learning with local and global consistency. Advances in Neural Information Processing Systems 16: 321-328.

[14] Zhang W, Hwang B, Wu B, et al. (2010) Network propagation models for gene selection. In: Genomic Signal Processing and Statistics (GENSIPS), 2010 IEEE International Workshop on. pp. 1-4. doi:10.1109/GENSIPS.2010.5719689.

[15] Winter C, Kristiansen G, Kersting S, et al. (2012) Google goes cancer: Improving outcome prediction for cancer patients by network-based ranking of marker genes. PLoS Comput Biol 8: e1002511.

[16] Cox DR (1972) Regression Models and Life-Tables. Journal of the Royal Statistical Society Series B (Methodological) 34: 187-220.

[17] Xing Y, Yu T, Wu YN, Roy M, Kim J, et al. (2006) An expectation-maximization algorithm for probabilistic reconstructions of full-length isoforms from splice graphs. Nucleic acids research 34: 3150-3160.

[18] Li B, Ruotti V, Stewart RM, Thomson JA, Dewey CN (2010) RNA-Seq gene expression estimation with read mapping uncertainty. Bioinformatics 26: 493-500.

[19] Breslow NE (1972) Discussion of professor cox's paper. J R Statist Soc : 216-217.

[20] Rozov R, Halperin E, Shamir R (2012) MGMR: leveraging RNA-Seq population data to optimize expression estimation. BMC Bioinformatics 13: S2.

[21] Li B, Ruotti V, Stewart RM, Thomson JA, Dewey CN (2010) RNA-Seq gene expression estimation with read mapping uncertainty. Bioinformatics 26: 493-500.

[22] Pachter L (2011) Models for transcript quantification from RNA-Seq. ArXiv : 1104.3889.

[23] Trapnell C, Williams BA, Pertea G, Mortazavi A, Kwan G, et al. (2010) Transcript assembly and quantification by RNA-Seq reveals unannotated transcripts and isoform switching during cell differentiation. Nat Biotech 28: 511-515.

[24] Li B, Dewey CN (2011) RSEM: accurate transcript quantification from RNA-Seq data with or without a reference genome. BMC Bioinformatics 12: 323.

[25] Trapnell C, Hendrickson DG, Sauvageau M, Goff L, Rinn JL, et al. (2012) Differential analysis of gene regulation at transcript resolution with RNA-Seq. Nature Biotechnology : 46–53.

[26] Gui J, Li H (2005) Penalized cox regression analysis in the high-dimensional and low-sample size settings, with applications to microarray gene expression data. Bioinformatics 21: 3001-3008.

[27] Zhang W, Johnson N, Wu B, Kuang R (2012) Signed Network Propagation for Detecting Differential Gene Expressions and DNA Copy Number Variations. In: Proceedings of the ACM Conference on Bioinformatics, Computational Biology and Biomedicine. New York, NY, USA: ACM, BCB '12, pp. 337–344. doi:10.1145/2382936.2382979.

[28] Huang Y, Hu Y, Jones CD, MacLeod JN, Chiang DY, et al. (2013) A Robust Method for Transcript Quantification with RNA-Seq Data. Journal of Computational Biology 20: 167-187.

[29] Jiang H, Wong WH (2009) Statistical inferences for isoform expression in RNA-Seq. Bioinformatics 25: 1026-1032.

[30] Derti A, Garrett-Engele P, MacIsaac KD, Stevens RC, Sriram S, et al. (2012) A quantitative atlas of polyadenylation in five mammals. Genome Research 22: 1173-1183.

[31] Tian B, Hu J, Zhang H, Lutz CS (2005) A large-scale analysis of mrna polyadenylation of human and mouse genes. Nucleic Acids Res 33: 201-212.

[32] Pickrell JK, Marioni JC, Pai AA, Degner JF, Engelhardt BE, et al. (2010) Understanding mechanisms underlying human gene expression variation with RNA sequencing. Nature 464: 768–772.

[33] Xia Z, Donehower LA, Cooper TA, Neilson JR, Wheeler DA, et al. (2014) Dynamic analyses of alternative polyadenylation from rna-seq reveal a 3-utr landscape across seven tumour types. Nature communications 5.

[34] Chang JW, Zhang W, Yeh HS, de Jong EP, Jun S, et al. (2015) mRNA 3'UTR shortening is a molecular signature of mTORC1 activation. Nature Communications 6: 7218.

[35] Zhang W, Ota T, Shridhar V, Chien J, Wu B, et al. (2013) Network-based Survival Analysis Reveals Subnetwork Signatures for Predicting Outcomes of Ovarian Cancer Treatment. PLoS Comput Biol 9: e1002975.

[36] Zhang W, Chang JW, Lin L, Minn K, Wu B, et al. (2015) Network-based Isoform Quantification with RNA-Seq Data for Cancer Transcriptome Analysis. PLoS Comput Biol 9: e1004465.

[37] Wilks C, Cline MS, Weiler E, Diehkans M, Craft B, et al. (2014) The cancer genomics hub (cghub): overcoming cancer through the power of torrential data. Database 2014.

[38] Barrett T, Wilhite SE, Ledoux P, Evangelista C, Kim IF, et al. (2013) Ncbi geo: archive for functional genomics data setsupdate. Nucleic Acids Research 41: D991-D995.

[39] Gevaert O, Smet FD, Timmerman D, et al. (2006) Predicting the prognosis of breast cancer by integrating clinical and microarray data with bayesian networks. Bioinformatics 22: 184-190.

[40] Rebbeck TR, Khoury MJ, Potter JD (2007) Genetic association studies of cancer: Where do we go from here? Cancer Epidemiology Biomarkers and Prevention 16: 864-865.

[41] Hwang T, Sicotte H, Tian Z, et al. (2008) Robust and efficient identification of biomarkers by classifying features on graphs. Bioinformatics 24: 2023–2029.

[42] Kunegis J, Schmidt S, Lommatzsch A, et al. (2010) Spectral analysis of signed graphs for clustering, prediction and visualization. Proceedings of the Eleventh SIAM International Conference on Data Mining, SDM2010 : 559-570.

[43] Pawitan Y, Bjohle J, Amler L, Borg A, Egyhazi S, et al. (2005) Gene expression profiling spares early breast cancer patients from adjuvant therapy: derived and validated in two population-based cohorts. Breast Cancer Res 7: R953-R964.

[44] Wang Y, Klijn JGM, Zhang Y, Sieuwerts A, Look M, et al. (2005) Gene-expression profiles to predict distant metastasis of lymph-node-negative primary breast cancer. The Lancet 365: 671-679.

[45] Miller L, Smeds J, George J, Vega V, Vergara L, et al. (2005) An expression signature for p53 status in human breast cancer predicts mutation status, transcriptional effects, and patient survival. Proceedings of the National Academy of Sciences 102: 13550-13555.

[46] Loi S, Haibe-Kains B, Desmedt C, Lallemand F, Tutt A, et al. (2007) Definition of clinically distinct molecular subtypes in estrogen receptor-positive breast carcinomas through genomic grade. Journal of Clinical Oncology 25: 1239-1246.

[47] Desmedt C, Piette F, Loi S, Wang Y, Lallemand F, et al. (2007) Strong time dependence of the 76-gene prognostic signature for node-negative breast cancer patients in the transbig multicenter independent validation series. Clinical Cancer Research 13: 3207.

[48] Irizarry RA, Hobbs B, Collin F, Beazer-Barclay YD, Antonellis KJ, et al. (2003) Exploration, normalization, and summaries of high density oligonucleotide array probe level data. Biostatistics 4: 249-264.

[49] Vapnik VN (1998) Statistical Learning Theory. Wiley-Interscience.

[50] Gribskov M, Robinson NL (1996) Use of receiver operating characteristic (ROC) analysis to evaluate sequence matching. Computers and Chemistry 20: 25-33.

[51] Huang DW, Sherman BT, Lempicki RA (2009) Systematic and integrative analysis of large gene lists using david bioinformatics resources. Nature Protocols 4: 44-57.

[52] Hamosh A, Scott AF, Amberger JS, et al. (2005) Online mendelian inheritance in man (omim), a knowledgebase of human genes and genetic disorders. Nucleic Acids Research 33: D514-D517.

[53] Pujana M, Han J, Starita L, et al. (2007) Network modeling links breast cancer susceptibility and centrosome dysfunction. Nat Genet 39: 1338-1349.

[54] Wong AKC, Pero R, Ormonde PA, et al. (1997) Rad51 interacts with the evolutionarily conserved brc motifs in the human breast cancer susceptibility gene brca2. Journal of Biological Chemistry 272: 31941-31944.

[55] Becker KG, Barnes KC, Bright TJ, et al. (2004) The genetic association database. Nat Genet 36: 431-432.

[56] Blaveri E, Brewer JL, Roydasgupta R, et al. (2005) Bladder cancer stage and outcome by array-based comparative genomic hybridization. Clinical Cancer Research 11: 7012-7022.

[57] Rosenwald A, Wright G, Chan WC, Connors JM, Campo E, et al. (2002) The use of molecular profiling to predict survival after chemotherapy for diffuse large-b-cell lymphoma. New England Journal of Medicine 346: 1937-1947.

[58] Bøvelstad HM, Nygård S, Størvold HL, Aldrin M, Borgan Ø, et al. (2007) Predicting survival from microarray data-a comparative study. Bioinformatics 23: 2080-2087.

[59] Cancer Genome Atlas Research Network (2011) Integrated genomic analyses of ovarian carcinoma. Nature 474: 609-615.

[60] Van Wieringen W, Kun D, Hampel R, Boulesteix A (2009) Survival prediction using gene expression data: a review and comparison. Computational statistics & data analysis 53: 1590-1603.

[61] Witten D, Tibshirani R (2010) Survival analysis with high-dimensional covariates. Stat Methods Med Res 19: 29-51.

[62] Hoerl AE, Kennard RW (1970) Ridge regression: biased estimation for non-orthogonal problems. Technometrics 12: 55-67.

[63] Pawitan Y, Bjohle J, Wedren S, Humphreys K, Skoog L, et al. (2004) Gene expression profiling for prognosis using cox regression. Stat Med 23: 1767-1780.

[64] Hastie T, Tibshirani R (2004) Efficient quadratic regularization for expression arrays. Biostatistics 5: 329-340.

[65] Van Houwelingen HC, Bruinsma T, Hart AAM, Van't Veer LJ, Wessels LFA (2006) Cross-validated cox regression on microarray gene expression data. Statistics in Medicine 25: 3201-3216.

[66] Tibshirani R (1997) The lasso method for variable selection in the cox model. Stat Med 16: 385-395.

[67] Efron B, Hastie T, Johnstone I, Tibshirani R (2004) Least angle regression. The Annals of statistics 32: 407-499.

[68] Segal MR (2006) Microarray gene expression data with linked survival phenotypes: diffuse large-b-cell lymphoma revisited. Biostatistics 7: 268-285.

[69] Park M, Hastie T (2007) L1-regularization path algorithm for generalized linear models. Journal of the Royal Statistical Society: Series B (Statistical Methodology) 69: 659-677.

[70] Sohn I, Kim J, Jung SH, Park C (2009) Gradient lasso for cox proportional hazards model. Bioinformatics 25: 1775-1781.

[71] Li H, Luan Y (2003) Kernel cox regression models for linking gene expression profiles to censored survival data. Pac Symp Biocomput : 65-76.

[72] Chuang HY, Lee E, Liu YT, Lee D, Ideker T (2007) Network-based classification of breast cancer metastasis. Mol Syst Biol 3: 140.

[73] Li C, Li H (2008) Network-constrained regularization and variable selection for analysis of genomic data. Bioinformatics 24: 1175-1182.

[74] Hwang T, Sicotte H, Tian Z, Wu B, Kocher J, et al. (2008) Robust and efficient identification of biomarkers by classifying features on graphs. Bioinformatics 24: 2023-2029.

[75] Tian Z, Hwang T, Kuang R (2009) A hypergraph-based learning algorithm for classifying gene expression and arraycgh data with prior knowledge. Bioinformatics 25: 2831-2838.

[76] Vandin F, Upfal E, Raphael B (2011) Algorithms for detecting significantly mutated pathways in cancer. J Comput Biol 18: 507-522.

[77] Kim Y, Wuchty S, Przytycka T (2011) Identifying causal genes and dysregulated pathways in complex diseases. PLoS Comput Biol 7: e1001095.

[78] Tothill RW, Tinker AV, George J, Brown R, Fox SB, et al. (2008) Novel molecular subtypes of serous and endometrioid ovarian cancer linked to clinical outcome. Clinical Cancer Research 14: 5198-5208.

[79] Bonome T, Levine DA, Shih J, Randonovich M, Pise-Masison CA, et al. (2008) A gene signature predicting for survival in suboptimally debulked patients with ovarian cancer. Cancer research 68: 5478-5486.

[80] Crijns APG, Fehrmann RSN, Jong SD, Gerbens F, Meersma GJ, et al. (2009) Survival-related profile, pathways, and transcription factors in ovarian cancer. PLoS Med 6: e1000024.

[81] Hatzirodos N, Bayne RA, Irving-Rodgers HF, Hummitzsch K, Sabatier L, et al. (2011) Linkage of regulators of tgf-β activity in the fetal ovary to polycystic ovary syndrome. FASEB J 25: 2256-2265.

[82] Ghosh S, Albitar L, LeBaron R, Welch WR, Samimi G, et al. (2010) Up-regulation of stromal versican expression in advanced stage serous ovarian cancer. Gynecologic oncology 119: 114-120.

[83] Yiu GK, Chan WY, Ng SW, Chan PS, Cheung KK, et al. (2001) Sparc (secreted protein acidic and rich in cysteine) induces apoptosis in ovarian cancer cells. The American journal of pathology 159: 609-622.

[84] Xian L, He W, Pang F, Hu Y (2012) Adipoq gene polymorphisms and susceptibility to polycystic ovary syndrome: a huge survey and meta-analysis. European Journal of Obstetrics & Gynecology and Reproductive Biology 161: 117-124.

[85] Gery S, Xie D, Yin D, Gabra H, Miller C, et al. (2005) Ovarian carcinomas: Ccn genes are aberrantly expressed and ccn1 promotes proliferation of these cells. Clinical Cancer Research 11: 7243-7254.

[86] Adam M, Saller S, Ströbl S, Hennebold J, Dissen G, et al. (2012) Decorin is a part of the ovarian extracellular matrix in primates and may act as a signaling molecule. Human Reproduction 27: 3249-3258.

[87] Rocconi RP, Kirby TO, Seitz RS, Beck R, Straughn Jr JM, et al. (2008) Lipoxygenase pathway receptor expression in ovarian cancer. Reproductive Sciences 15: 321-326.

[88] Bridges PJ, Jo M, Al Alem L, Na G, Su W, et al. (2010) Production and binding of endothelin-2 (edn2) in the rat ovary: endothelin receptor subtype a (ednra)-mediated contraction. Reproduction, Fertility and Development 22: 780-787.

[89] Sutphen R, Xu Y, Wilbanks GD, Fiorica J, Grendys Jr EC, et al. (2004) Lysophospholipids are potential biomarkers of ovarian cancer. Cancer Epidemiology Biomarkers & Prevention 13: 1185-1191.

[90] Mok SC, Bonome T, Vathipadiekal V, Bell A, Johnson ME, et al. (2009) A gene signature predictive for outcome in advanced ovarian cancer identifies a survival factor: microfibril-associated glycoprotein 2. Cancer cell 16: 521-532.

[91] Sengupta S, Kim KS, Berk MP, Oates R, Escobar P, et al. (2006) Lysophosphatidic acid downregulates tissue inhibitor of metalloproteinases, which are negatively involved in lysophosphatidic acid-induced cell invasion. Oncogene 26: 2894-2901.

[92] Czekierdowski A, Czekierdowska S, Danilos J, Czuba B, Sodowski K, et al. (2008) Microvessel density and cpg island methylation of thbs2 gene in malignant ovarian tumors. J Physiol Pharmacol 59: 53-65.

[93] Kryczek I, Lange A, Mottram P, Alvarez X, Cheng P, et al. (2005) Cxcl12 and vascular endothelial growth factor synergistically induce neoangiogenesis in human ovarian cancers. Cancer research 65: 465-472.

[94] Geles KG, Freiman RN, Liu WL, Zheng S, Voronina E, et al. (2006) Cell-type-selective induction of c-jun by taf4b directs ovarian-specific transcription networks. Proc Natl Acad Sci U S A 103: 2594-2599.

[95] Richards JS, Russell DL, Ochsner S, Hsieh M, Doyle KH, et al. (2002) Novel signaling pathways that control ovarian follicular development, ovulation, and luteinization. Recent Prog Horm Res 57: 195-220.

[96] Levina V, Nolen BM, Marrangoni AM, Cheng P, Marks JR, et al. (2009) Role of eotaxin-1 signaling in ovarian cancer. Clinical Cancer Research 15: 2647-2656.

[97] Stronach EA, Sellar GC, Blenkiron C, Rabiasz GJ, Taylor KJ, et al. (2003) Identification of clinically relevant genes on chromosome 11 in a functional model of ovarian cancer tumor suppression. Cancer research 63: 8648-8655.

[98] Körner M, Waser B, Reubi JC (2003) Neuropeptide y receptor expression in human primary ovarian neoplasms. Laboratory investigation 84: 71-80.

[99] Sood AK, Coffin JE, Schneider GB, Fletcher MS, DeYoung BR, et al. (2004) Biological significance of focal adhesion kinase in ovarian cancer: role in migration and invasion. Am J Pathol 165: 1087-1095.

[100] Allen HJ, Sucato D, Woynarowska B, Gottstine S, Sharma A, et al. (1990) Role of galaptin in ovarian carcinoma adhesion to extracellular matrix in vitro. J Cell Biochem 43: 43-57.

[101] Yang X, Kovalenko OV, Tang W, Claas C, Stipp CS, et al. (2004) Palmitoylation supports assembly and function of integrintetraspanin complexes. The Journal of Cell Biology 167: 1231-1240.

[102] Ucar D, Neuhaus I, Ross-MacDonald P, Tilford C, Parthasarathy S, et al. (2007) Construction of a reference gene association network from multiple profiling data: application to data analysis. Bioinformatics 23: 2716-2724.

[103] Huttenhower C, Haley EM, Hibbs MA, Dumeaux V, Barrett DR, et al. (2009) Exploring the human genome with functional maps. Genome Research 19: 1093-1106.

[104] Johnson WE, Li C, Rabinovic A (2007) Adjusting batch effects in microarray expression data using empirical bayes methods. Biostatistics 8: 118-127.

[105] Higgins ME, Claremont M, Major JE, Sander C, Lash AE (2007) Cancergenes: a gene selection resource for cancer genome projects. Nucleic Acids Research 35: D721-D726.

[106] Simon N, Friedman J, Hastie T, Tibshirani R (2011) Regularization paths for cox's proportional hazards model via coordinate descent. Journal of Statistical Software 39: 1-13.

[107] Mantel N (1966) Evaluation of survival data and two new rank order statistics arising in its consideration. Cancer chemotherapy reports 50: 163-170.

[108] Heagerty PJ, Lumley T, Pepe MS (2000) Time-dependent roc curves for censored survival data and a diagnostic marker. Biometrics 56: 337-344.

[109] Li H, Gui J (2004) Partial cox regression analysis for high-dimensional microarray gene expression data. Bioinformatics 20: i208-i215.

[110] Chien J, Aletti G, Baldi A, Catalano V, Muretto P, et al. (2006) Serine protease htra1 modulates chemotherapy-induced cytotoxicity. J Clin Invest 116: 1994-2004.

[111] Bair E, Tibshirani R (2004) Semi-supervised methods to predict patient survival from gene expression data. PLoS Biology 2: e108.

[112] Bair E, Hastie T, Paul D, Tibshirani R (2006) Prediction by supervised principal components. Journal of the American Statistical Association 101: 119-137.

[113] Li L, Li H (2004) Dimension reduction methods for microarrays with application to censored survival data. Bioinformatics 20: 3406-3412.

[114] Nguyen D, Rocke D (2002) Partial least squares proportional hazard regression for application to dna microarray survival data. Bioinformatics 18: 1625-1632.

[115] Bastien P (2004) Pls-cox model: application to gene expression. Proceedings in Computational Statistics : 655-662.

[116] Bastien P, Vinzi V, Tenenhaus M (2005) Pls generalised linear regression. Computational Statistics & Data Analysis 48: 17-46.

[117] Boulesteix A, Strimmer K (2007) Partial least squares: a versatile tool for the analysis of high-dimensional genomic data. Briefings in bioinformatics 8: 32-44.

[118] Hothorn T, Lausen B, Benner A, Radespiel-Troger M (2004) Bagging survival trees. Stat Med 23: 77-91.

[119] Hothorn T, Buhlmann P, Dudoit S, Molinaro A, van der Laan M (2006) Survival ensembles. Biostatistics 7: 355-373.

[120] Ma S, Song X, Huang J (2007) Supervised group lasso with applications to microarray data analysis. BMC Bioinformatics 8: 60.

[121] Simon N, Friedman J, Hastie T, Tibshirani R (2012) A sparse-group lasso. Journal of Computational and Graphical Statistics, DOI 10: 681250.

[122] Sherman-Baust C, Weeraratna A, Rangel L, Pizer E, Cho K, et al. (2003) Remodeling of the extracellular matrix through overexpression of collagen vi contributes to cisplatin resistance in ovarian cancer cells. Cancer Cell 3: 377-386.

[123] Mortazavi A, Williams BA, McCue K, Schaeffer L, Wold B (2008) Mapping and quantifying mammalian transcriptomes by RNA-Seq. Nat Meth 5: 621-628.

[124] Wang ET, Sandberg R, Luo S, Khrebtukova I, Zhang L, et al. (2008) Alternative isoform regulation in human tissue transcriptomes. Nature 456: 470-476.

[125] Li JJ, Jiang CR, Brown JB, Huang H, Bickel PJ (2011) Sparse linear modeling of next-generation mRNA sequencing (RNA-Seq) data for isoform discovery and abundance estimation. Proceedings of the National Academy of Sciences 108: 19867-19872.

[126] Li W, Kang S, Liu CC, Zhang S, Shi Y, et al. (2014) High-resolution functional annotation of human transcriptome: predicting isoform functions by a novel multiple instance-based label propagation method. Nucleic Acids Research 42: e39.

[127] Yang EW, Girke T, Jiang T (2013) Differential Gene Expression Analysis Using Coexpression and RNA-Seq Data. Bioinformatics 29: 2153-2161.

[128] Roberts A, Trapnell C, Donaghey J, Rinn J, Pachter L (2011) Improving RNA-Seq expression estimates by correcting for fragment bias. Genome Biology 12: R22.

[129] Turro E, Su SY, Goncalves A, Coin L, Richardson S, et al. (2011) Haplotype and isoform specific expression estimation using multi-mapping RNA-seq reads. Genome Biology 12: R13.

[130] Kriventseva EV, Koch I, Apweiler R, Vingron M, Bork P, et al. (2003) Increase of functional diversity by alternative splicing. Trends in Genetics 19: 124 - 128.

[131] Resch A, Xing Y, Modrek B, Gorlick M, Riley R, et al. (2004) Assessing the impact of alternative splicing on domain interactions in the human proteome. Journal of Proteome Research 3: 76-83.

[132] Tseng YT, Li W, Chen CH, Zhang S, Chen J, et al. (2015) IIIDB: a database for isoform-isoform interactions and isoform network modules. BMC Genomics 16: S10.

[133] Finn RD, Marshall M, Bateman A (2005) iPfam: visualization of protein–protein interactions in PDB at domain and amino acid resolutions. Bioinformatics 21: 410-412.

[134] Stein A, Ceol A, Aloy P (2011) 3did: identification and classification of domain-based interactions of known three-dimensional structure. Nucleic Acids Research 39: 718-723.

[135] Punta M, Coggill PC, Eberhardt RY, Mistry J, Tate JG, et al. (2012) The Pfam protein families database. Nucleic Acids Research 40: 290-301.

[136] Pruitt KD, Tatusova TA, Brown GR, Maglott DR (2012) NCBI Reference Sequences (RefSeq): current status, new features and genome annotation policy. Nucleic Acids Research 40: 130-135.

[137] Berman HM, Westbrook JD, Feng Z, Gilliland G, Bhat TN, et al. (2000) The Protein Data Bank. Nucleic Acids Research 28: 235-242.

[138] Yellaboina S, Tasneem A, Zaykin DV, Raghavachari B, Jothi R (2011) DOMINE: a comprehensive collection of known and predicted domain-domain interactions. Nucleic Acids Research 39: 730-735.

[139] Prasad TSK, Goel R, Kandasamy K, Keerthikumar S, Kumar S, et al. (2009) Human Protein Reference Database–2009 update. Nucleic Acids Research 37: 767-772.

[140] Futreal PA, Coin L, Marshall M, Down T, Hubbard T, et al. (2004) A census of human cancer genes. Nature Reviews Cancer 4: 177-183.

[141] Higgins ME, Claremont M, Major JE, Sander C, Lash AE (2007) Cancergenes: a gene selection resource for cancer genome projects. Nucleic Acids Research 35: D721-D726.

[142] Tanaka Y, Kim KY, Zhong M, Pan X, Weissman SM, et al. (2014) Transcriptional regulation in pluripotent stem cells by methyl CpG-binding protein 2 (MeCP2). Human Molecular Genetics 23: 1045-1055.

[143] Daemen A, Griffith O, Heiser L, Wang N, Enache O, et al. (2013) Modeling precision treatment of breast cancer. Genome Biology 14: R110.

[144] Kim D, Pertea G, Trapnell C, Pimentel H, Kelley R, et al. (2013) TopHat2: accurate alignment of transcriptomes in the presence of insertions, deletions and gene fusions. Genome Biology 14: R36.

[145] Li H, Handsaker B, Wysoker A, Fennell T, Ruan J, et al. (2009) The Sequence Alignment/Map format and SAMtools. Bioinformatics 25: 2078-2079.

[146] Kanehisa M, Goto S (2000) KEGG: Kyoto Encyclopedia of Genes and Genomes. Nucleic Acids Research 28: 27-30.

[147] Griebel T, Zacher B, Ribeca P, Raineri E, Lacroix V, et al. (2012) Modelling and simulating generic RNA-Seq experiments with the flux simulator. Nucleic Acids Research 40: 10073-10083.

[148] Patro R, Mount SM, Kingsford C (2014) Sailfish enables alignment-free isoform quantification from RNA-seq reads using lightweight algorithms. Nat Biotech 32: 462–464.

[149] Tian B, Manley JL (2013) Alternative cleavage and polyadenylation: the long and short of it. Trends Biochem Sci 38: 312-320.

[150] Gruber AR, Martin G, Keller W, Zavolan M (2014) Means to an end: mechanisms of alternative polyadenylation of messenger rna precursors. Wiley Interdiscip Rev RNA 5: 183-196.

[151] Shi Y (2012) Alternative polyadenylation: new insights from global analyses. RNA 18: 2105-2117.

[152] Lutz CS, Moreira A (2011) Alternative mrna polyadenylation in eukaryotes: an effective regulator of gene expression. Wiley Interdiscip Rev RNA 2: 22-31.

[153] Sandberg R, Neilson JR, Sarma A, Sharp PA, Burge CB (2008) Proliferating cells express mrnas with shortened 3[prime] untranslated regions and fewer microrna target sites. Science 320: 1643-1647.

[154] Mayr C, Bartel DP (2009) Widespread shortening of 3[prime]utrs by alternative cleavage and polyadenylation activates oncogenes in cancer cells. Cell 138: 673-684.

[155] Shepard PJ (2011) Complex and dynamic landscape of rna polyadenylation revealed by pas-seq. RNA 17: 761-772.

[156] Hoque M (2013) Analysis of alternative cleavage and polyadenylation by 3' region extraction and deep sequencing. Nat Methods 10: 133-139.

[157] Lianoglou S, Garg V, Yang JL, Leslie CS, Mayr C (2013) Ubiquitously transcribed genes use alternative polyadenylation to achieve tissue-specific expression. Genes Dev 27: 2380-2396.

[158] Ji Z, Lee JY, Pan Z, Jiang B, Tian B (2009) Progressive lengthening of 3' untranslated regions of mrnas by alternative polyadenylation during mouse embryonic development. Proc Natl Acad Sci USA 106: 7028-7033.

[159] Singh P (2009) Global changes in processing of mrna 3' untranslated regions characterize clinically distinct cancer subtypes. Cancer Res 69: 9422-9430.

[160] Laplante M, Sabatini DM (2012) mtor signaling in growth control and disease. Cell 149: 274-293.

[161] Ma XM, Blenis J (2009) Molecular mechanisms of mtor-mediated translational control. Nat Rev Mol Cell Biol 10: 307-318.

[162] Hsieh AC (2012) The translational landscape of mtor signalling steers cancer initiation and metastasis. Nature 485: 55-61.

[163] Thoreen CC (2012) A unifying model for mtorc1-mediated regulation of mrna translation. Nature 485: 109-113.

[164] Laplante M, Sabatini DM (2013) Regulation of mtorc1 and its impact on gene expression at a glance. J Cell Sci 126: 1713-1719.

[165] Lamming DW, Sabatini DM (2013) A central role for mtor in lipid homeostasis. Cell Metab 18: 465-469.

[166] Zhang Y (2014) Coordinated regulation of protein synthesis and degradation by mtorc1. Nature 513: 440-443.

[167] Kwiatkowski DJ (2002) A mouse model of tsc1 reveals sex-dependent lethality from liver hemangiomas, and up-regulation of p70s6 kinase activity in tsc1 null cells. Hum Mol Genet 11: 525-534.

[168] Tee AR, Manning BD, Roux PP, Cantley LC, Blenis J (2003) Tuberous sclerosis complex gene products, tuberin and hamartin, control mtor signaling by acting as a gtpase-activating protein complex toward rheb. Curr Biol 13: 1259-1268.

[169] Knowles MA, Habuchi T, Kennedy W, Cuthbert-Heavens D (2003) Mutation spectrum of the 9q34 tuberous sclerosis gene tsc1 in transitional cell carcinoma of the bladder. Cancer Res 63: 7652-7656.

[170] Guo Y (2013) Tsc1 involvement in bladder cancer: diverse effects and therapeutic implications. J Pathol 230: 17-27.

[171] Guertin DA, Sabatini DM (2009) The pharmacology of mtor inhibition. Sci Signal 2: pe24.

[172] Filipowicz W, Bhattacharyya SN, Sonenberg N (2008) Mechanisms of post-transcriptional regulation by microrna: are the answers in sight? Nat Rev Genet 9: 102-114.

[173] Shimobayashi M, Hall MN (2014) Making new contacts: the mtor network in metabolism and signalling crosstalk. Nat Rev Mol Cell Biol 15: 155-162.

[174] Trapnell C, Pachter L, Salzberg SL (2009) TopHat: discovering splice junctions with RNA-Seq. Bioinformatics 25: 1105-1111.

[175] Beaudoing E, Freier S, Wyatt JR, Claverie JM, Gautheret D (2000) Patterns of variant polyadenylation signal usage in human genes. Genome Res 10: 1001-1010.

[176] Howell JJ, Ricoult SJ, Ben-Sahra I, Manning BD (2013) A growing role for mtor in promoting anabolic metabolism. Biochem Soc Trans 41: 906-912.

[177] Chio II (2012) Tradd contributes to tumour suppression by regulating ulf-dependent p19arf ubiquitylation. Nat Cell Biol 14: 625-633.

[178] Teixeira LK, Reed SI (2013) Ubiquitin ligases and cell cycle control. Annu Rev Biochem 82: 387-414.

[179] Yanagiya A (2012) Translational homeostasis via the mrna cap-binding protein, eif4e. Mol Cell 46: 847-858.

[180] Chen D, Shan J, Zhu WG, Qin J, Gu W (2010) Transcription-independent arf regulation in oncogenic stress-mediated p53 responses. Nature 464: 624-627.

[181] Hagting A (2002) Human securin proteolysis is controlled by the spindle checkpoint and reveals when the apc/c switches from activation by cdc20 to cdh1. J Cell Biol 157: 1125-1137.

[182] Zhou L (2013) The role of ring box protein 1 in mouse oocyte meiotic maturation. PLoS One 8: e68964.

[183] Kraft C (2003) Mitotic regulation of the human anaphase-promoting complex by phosphorylation. EMBO J 22: 6598-6609.

[184] Jia L, Sun Y (2009) Rbx1/roc1-scf e3 ubiquitin ligase is required for mouse embryogenesis and cancer cell survival. Cell Div 4: 16-21.

[185] Bartke T, Pohl C, Pyrowolakis G, Jentsch S (2004) Dual role of bruce as an antiapoptotic iap and a chimeric e2/e3 ubiquitin ligase. Mol Cell 14: 801-811.

[186] Shepard PJ, Choi EA, Lu J, Flanagan LA, Hertel KJ, et al. (2011) Complex and dynamic landscape of rna polyadenylation revealed by pas-seq. Rna 17: 761–772.